博士論文

Development of ultra-small instruments for planetary UV radiations

(惑星紫外放射の測定に向けた超小型観測器の開発)

東京大学大学院新領域創成科学研究科

複雑理工学専攻

桑原　正輝

博士論文

論文題目　Development of ultra-small instruments for planetary UV radiations
(惑星紫外放射の測定に向けた超小型観測器の開発)

氏　　名　桑原　正輝

Abstract

Planetary atmospheres and plasmas are excited by resonant scattering and electron impacts that emit light in a wide spectral range. Many of these emission lines are in the ultraviolet (UV) wavelength range. However, UV light is absorbed by the Earth's atmosphere; therefore, in order to measure their intensities, observations using satellites and spacecraft are essential. Unfortunately, conventional large exploration missions can take a long time to achieve. In order to solve this problem, ultra-small exploration missions have been planned. Compared to larger missions, ultra-small missions can be performed with shorter development times and lower costs. Such missions can increase exploration opportunities. Therefore, the various development and operational results can be fed back to efficiently inform future plans. However, small and highly efficient scientific instruments are required for these missions in association with spacecraft size and weight reductions. In this thesis, the development of highly efficient instruments for ultra-small missions is described.

The development of a telescope for detecting extreme ultraviolet (EUV) light named PHOENIX (Plasmaspheric Helium ion Observation by Enhanced New Imager in eXtreme ultraviolet) onboard the EQUilibriUm Lunar-Earth point 6U Spacecraft (EQUULEUS), which is scheduled to be launched into the Moon fly-by orbit in 2019, is described in Chapter 2. The optical design, especially the entrance mirror, which determines the light collection ability, was optimized for ultra-small observation missions.

A new multilayer coating that has a high reflectivity at 30.4 nm has been developed. The newly developed Mg/SiC multilayer coating designed for normal incident light had a higher reflectivity (37%) at 30.4 nm than the Mo/Si coating conventionally used in planetary and space missions. The temporal stability of the Mg/SiC multilayer coating was also evaluated. The coating was found to be stable under vacuum, dry N_2 purge, and normal atmosphere. Based on these results, the Mg/SiC multilayer coated mirror was selected as the PHOENIX flight mirror. PHOENIX can sufficiently attain the mission scientific objectives by acquiring an entire image of the

helium ions in the plasmasphere with a temporal resolution of < 1 hour.

In Chapter 3, the development of absorption cells for ultra-small missions is described. Atomic hydrogens in the planetary exosphere resonantly scatter solar Lyman-alpha emissions at 121.567 nm and form the planetary corona. Imaging the hydrogen corona allows the study of the density distribution of the atomic hydrogen. The absorption cell technique is a powerful tool for imaging the planetary hydrogen corona because the spatial density distribution and temperature can be obtained. These parameters provide insights used to estimate the present amount of planetary water dissipation. In an earlier attempt to apply the absorption cell technique, an UVS-P photometer was developed and installed in the Japanese Mars Orbiter NOZOMI launched in 1998. In this mission, however, because of the limited development time, the parameters that determine the absorption performance were insufficiently optimized. The absorption performance critically depends on filament shape (i.e., length and diameter), power applied to the filament, and the gas pressure in the cell. These parameters determine the thermal dissociation efficiency at the filament surface. The present study, therefore, focused mainly on the physical thermal dissociation process at the tungsten filament surface and the construction of new hydrogen absorption cells. To increase the power density and the dissociation rate, the new cells have several filaments that are thinner and/or shorter than those used in previous studies. The cells also have inlet ports that enable the H_2 gas pressure in the cells to be varied from the outside the cell. The optical thickness dependence and the Full Width at Half Maximum (FWHM) were used as performance indices for the new cell parameters and have been evaluated using the DESIRS (Dichroïsme Et Spectroscopie par Interaction avec le Rayonnement Synchrotron) beamline at the Synchrotron SOLEIL in France. The optical thickness with thinner filaments (diameter of 24.4 μm), gas pressure of 100-300 Pa, and filament power of 1-3 W were found to be about 4 times higher than those with the UVS-P photometer. In addition, determining the Doppler temperature of the Martian hydrogen coronas has been realized with an accuracy of approximately 30 K.

Contents

Acknowledgements

I wish to express my sincere appreciation to my supervisor, Prof. Ichiro Yoshikawa for his kind guidance during my doctoral and master's courses. The conversations with him have been very stimulating.

I express my deep gratitude to Lecturer Kazuo Yoshioka at the University of Tokyo, assistant professor Go Murakami at ISAS/JAXA, and all of the EQUULEUS project members.

I express my sincere thanks to Prof. Takeshi Imamura. His comments on my thesis were very sincere and constructive.

I wish to thank Mr. Fumiharu Suzuki, Miss Reina Hikida, and all of the colleagues who are (and were) associated with Yoshikawa Ichiro's Laboratory at the University of Tokyo.

I also wish to thank Mr. Hiroshi Takahashi and Dr. Takuo Watanabe at the Meisei Electronics Corporation for their sincere efforts.

I express my thanks to Mr. Rin Yamamoto, who was a vacuum technical expert. He provided many significant suggestions before he passed away.

I would like to thank Prof. Makoto Taguchi, and associate Prof. Shingo Kameda for providing useful comments and technical advice.

I am grateful to associate Prof. Michiaki Inomoto, associate Prof. Satoshi Kasahara, and associate Prof. Hiroyuki Koizumi for their very sincere and constructive comments on my thesis.

My greatest acknowledgement is sent to my parents, Naoki and Mutsuko. They have supported me during all my life. I am also grateful to my brothers, Hiroki and Motoki, for their encouragement.

Finally, I would like to express my special thanks to my future wife, Emi. This work could not be accomplished without her sincere support for many years.

Chapter 1. General Introduction

1.1. Imaging Observations for Planetary UV radiation

Optical observations of planetary atmospheres in a wide spectral range have been conducted. Ultraviolet (UV) light is particularly useful for planetary science to obtain various information about planetary upper atmospheres. However, It is difficult to effectively detect UV light by ground-based observations due to absorption by the terrestrial atmosphere. Thus, the launch of cumbersome instruments into outer space has been required.

Imaging observations of UV light have enabled scientists to study the temporal evolution and spatial structure of planetary upper atmospheres. In 1972, Apollo-16 was launched and succeeded in imaging the first two-dimensional geocoronal hydrogen Lyman-alpha (wavelength: 121.6 nm) spectra from the Moon using an ultraviolet camera [*Carruthers et al.*, 1976]. Figure 1.1 shows the intensity distribution of the hydrogen corona imaged by Apollo-16. The camera field-of-view was ~10 Re (Re – Earth radius). One can clearly see Earth surrounded by the hydrogen corona. During the mission, the Schmidt camera in UV light (as shown in Figure 1.2) was used, and KBr was deposited as a photoelectric surface on a focal plane. The incident photons were converted to electrons, and the electrons were accelerated at a high voltage of 25 kV and detected by a film. Using this technique, the camera achieved sensitivity 20 times higher than cameras without the KBr coating [*Carruthers*, 1973].

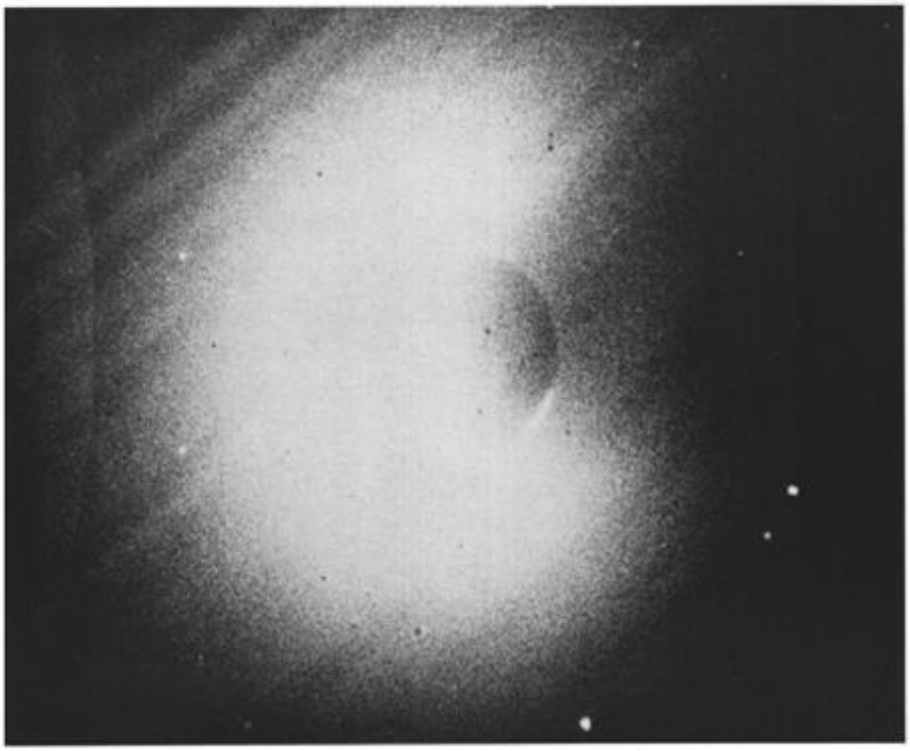

Figure 1.1. Two-dimensional image of Earth's hydrogen corona observed by Apollo-16 from the Moon. The target wavelength for this mission was 105-160 nm. The black circle located near the center of the image shows Earth, which is surrounded by the hydrogen corona. The camera field-of-view was ~10 Re [*Carruthers et al.*, 1976].

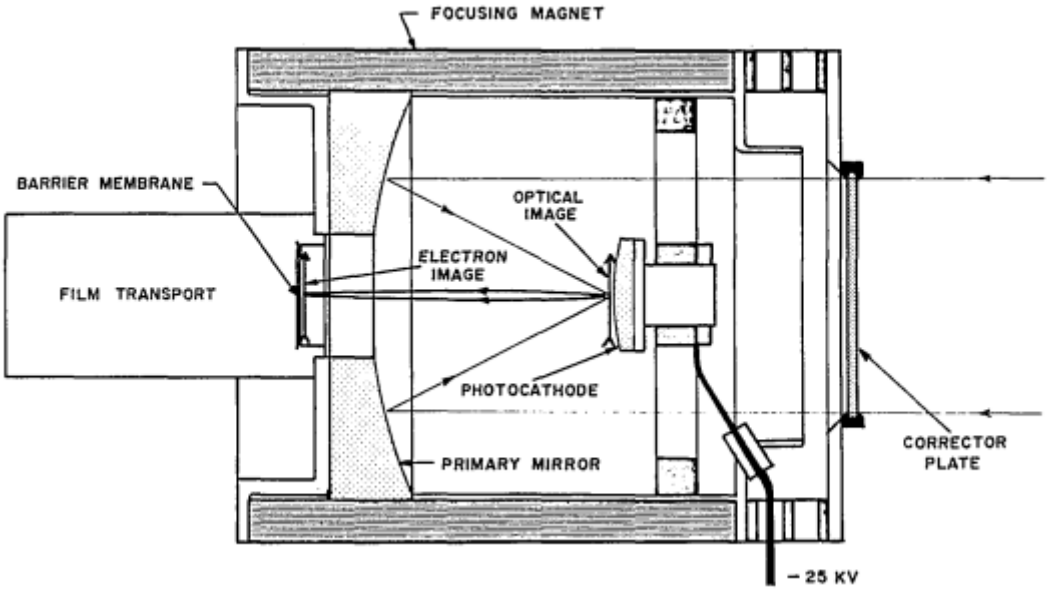

Figure 1.2. Simplified cross-sectional diagram of the Schmidt camera installed for the Apollo-16 mission [*Carruthers*, 1973].

Extreme UltraViolet imager (EUV) spectroscopic observations of the atmospheres of Mercury and Venus that were carried out by Mariner-10 in 1977 quantified the abundances of the atmospheric components. Mariner-10 had a primitive detector installed in order to only obtain the densities of components around the targets [*Broadfoot et al.*, 1977]. The EUV monochromator installed in Mariner-10 did not have an entrance mirror, but had sixteen collimators. The design is shown in Figure 1.3. A number of photomultipliers were installed at the focal points of each spectral line and simply acted as photon counting devices. The incident light with wavelengths in a wide spectral range was diffracted by a grating.

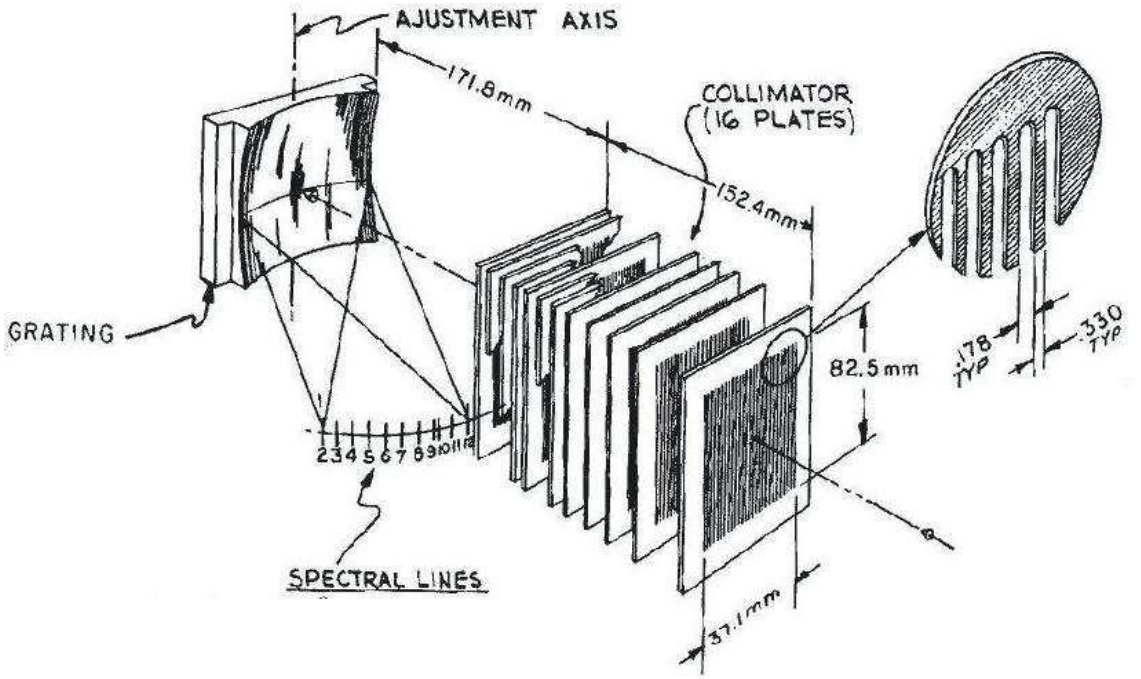

Figure 1.3. Design of the EUV monochromator installed in Mariner-10 [*Broadfoot et al.*, 1977].

After the Mariner-10 mission, remote observations of planetary UV radiations have been widely used as a method to quantify the abundances of atmospheres and plasmas. In 1998, an EUV scanner onboard the NOZOMI spacecraft [*Nakamura et al.*, 2000] conducted the first imaging observation of the Earth's plasmasphere by detecting the resonantly scattered light from He ions (He II: 30.4 nm) [*Yoshikawa et al.*, 2000a, 2000b, 2001]. Figure 1.4 shows a two-dimensional image observed by the scanner. Wavelength selections were performed by metallic thin filters that are transparent to light of specific wavelength ranges. A multilayer coated mirror was used to efficiently collect the EUV light (shown in Figure 1.5).

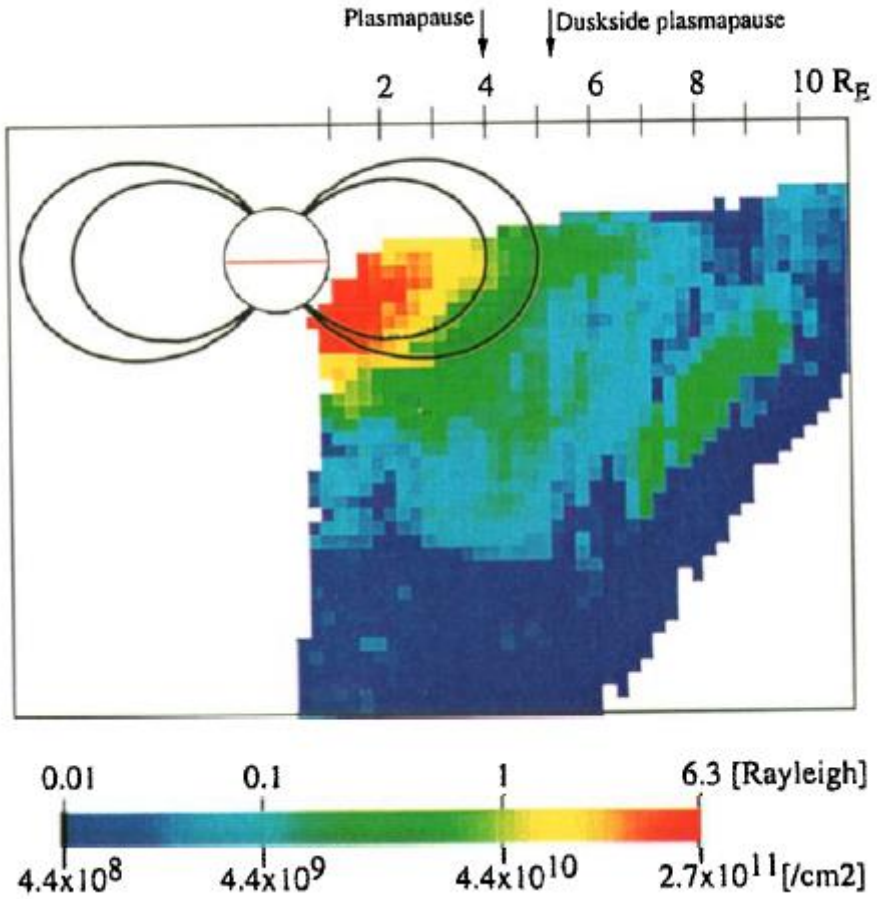

Figure 1.4. Two-dimensional image of the plasmasphere observed by NOZOMI. The L = 4 and 5 dipole magnetic field lines are also shown [*Yoshikawa et al.*, 2000].

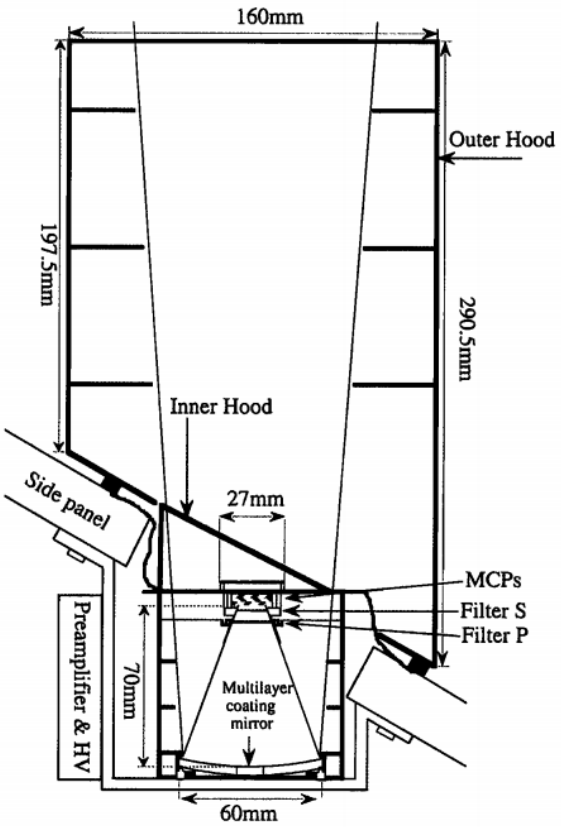

Figure 1.5. Schematic cross-sectional diagram of the EUV scanner onboard NOZOMI. The optical layout consists of a multilayer coated mirror that has a high reflectivity for 30.4 nm light, metallic thin filters for wavelength selection, and microchannel plates as the two-dimensional photon counting devices.

Further sequential imaging observations were made by the EUV imager on the Imager for Magnetopause-to-Aurora Global Exploration (IMAGE) satellite. The imager provided complete sequential pictures [*Burch et al.*, 2001a, 2001b; *Sandel et al.*, 2000, 2001]. It observed the distribution of He ions in the plasmasphere with temporal and spatial resolutions of 10 min., and 0.1 Re, respectively, from the apogee (~8 Re), and found the various plasmasphere structures [*Sandel et al.*, 2001, 2003] shown in Figure 1.6.

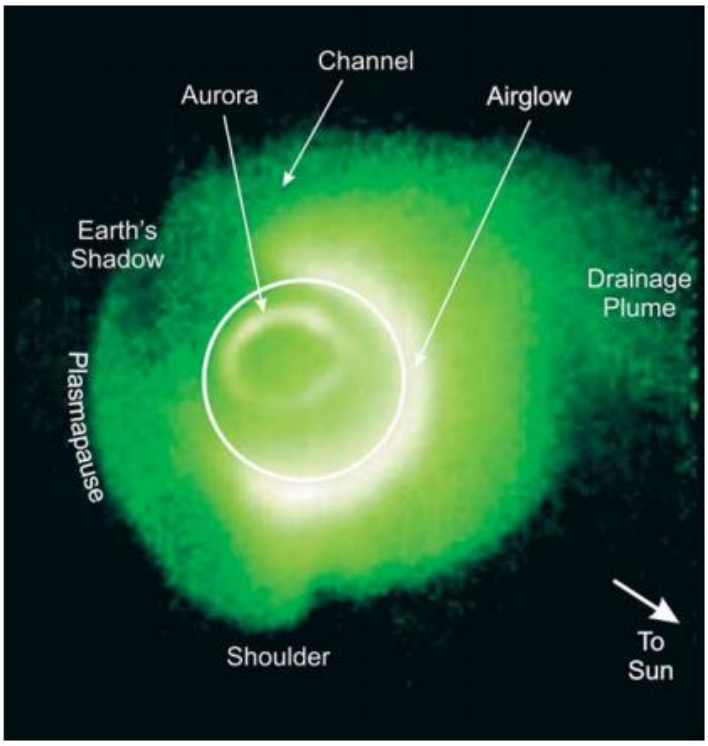

Figure 1.6. Two-dimensional image observed by IMAGE/EUV on May 24, 2000, during a magnetic disturbance. Several structures are clearly seen in this figure (e.g., shoulder, plume, and channel) [*Sandel et al.*, 2003].

A cutaway image of the EUV sensor onboard the IMAGE satellite [*Sandel et al.*, 2000] is shown in Figure 1.7. Optics similar to the EUV scanner onboard NOZOMI were used for the IMAGE/EUV. The optics was designed as a type of a normal incidence telescope, consisting of a multilayer coated mirror, a metallic thin filter, and microchannel plates.

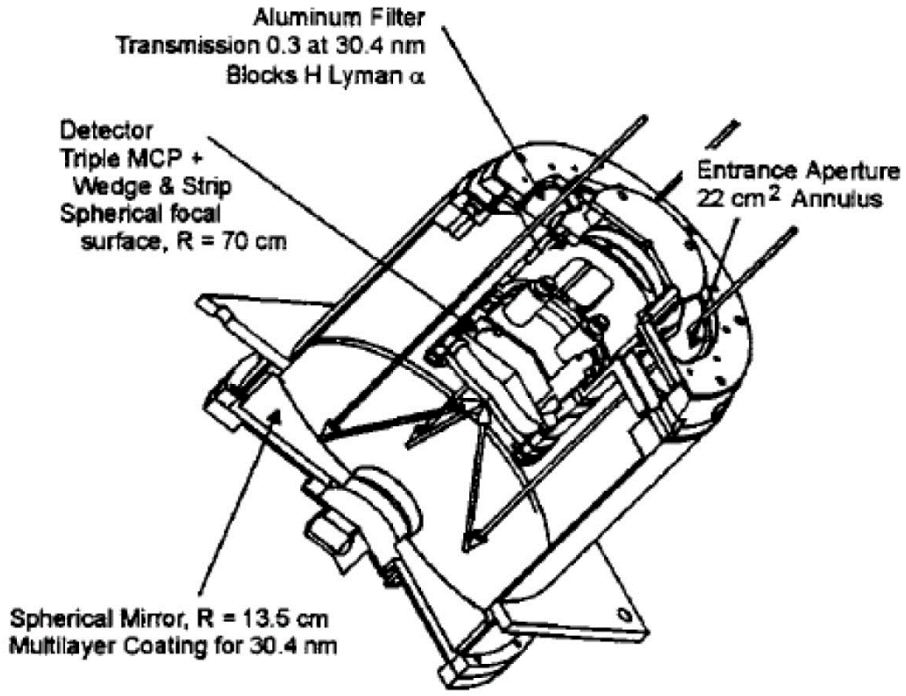

Figure 1.7. Cutaway drawing of the EUV sensor onboard the IMAGE satellite [*Sandel et al.*, 2000].

The first EUV imaging observation of a plasmasphere meridian perspective was conducted by the TEX onboard KAGUYA in 2008 [*Murakami et al.*, 2010]. The instrument found a new striking feature of enhanced brightness in the plasmasphere, which is called as plasmaspheric filament, during a prolonged quiet period [*Murakami et al.*, 2013] (as shown in Figure 1.8). It was suggested that the phenomenon is caused by an isolated magnetic flux tube filled with denser plasma than its neighbors. TEX found 4 events relative to the phenomenon, and the occurrence rate was estimated to be about 1 event / 8 days. In addition, all the events were observed during extremely quiet periods and no correlations between their occurrences and local times were identified.

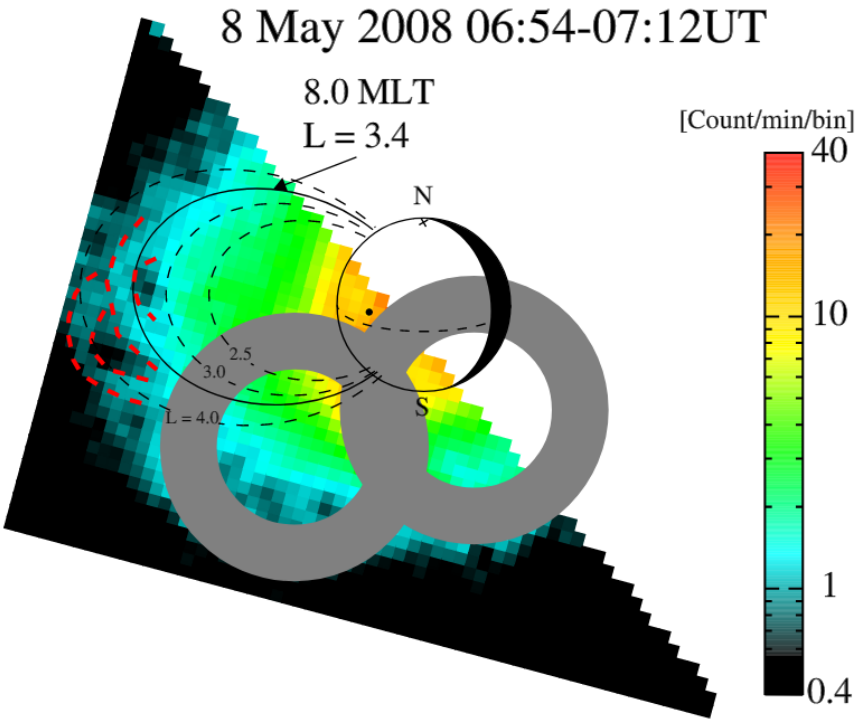

Figure 1.8. Image of plasmaspheric filaments obtained by KAGUYA/TEX. Two filament structures can be identified. The black lines represent the magnetic field lines assuming dipole magnetic field lines. The red dashed lines are traced to emphasize the loop structure.

The multilayer coating technique has been used conventionally to increase the reflectivity of mirrors in previous space missions, such as NOZOMI, IMAGE, and KAGUYA. All of them used multilayer coatings that have combinations of Mo and Si [e.g., *Yoshikawa et al.*, 2010]. In the ISS-IMAP (Ionosphere, Mesosphere, upper Atmosphere, and Plasmasphere mapping) mission [*Hozumi et al.*, 2017], which started in 2012, a Y_2O_3/Al multilayer coated mirror that has a higher reflectivity at 30.4 nm with a lower reflectivity at 58.4 nm than the Mo/Si mirror was developed for the Extreme Ultra Violet Imager (EUVI) in order to prevent light that is resonantly scattered by helium atoms (He I: 58.4 nm) and can possibly act as a contamination source from entering the detector [*Murakami et al.*, 2011]. As described above, in recent EUV imaging missions, the majority of instrument development efforts have been devoted to producing mirrors with high reflectivities for EUV light.

1.2. Ultra-Small Mission

Recently, governmental space agencies, private companies, and universities have been planning to conduct nano-satellite (1–10 kg) and micro-satellite (~50 kg) missions for deep space explorations.

As the first step in these attempts, the first 50-kg class micro-spacecraft, PROCYON (PRoximate Object Close flYby with Optical Navigation), jointly developed by the Japan Aerospace Exploration Agency (JAXA) and the University of Tokyo, was launched into space with HAYABUSA-2 in December 2014 [*Funase et al.*, 2015]. During its one-year flight in deep space, PROCYON succeeded in its primary objective as an engineering technology demonstration.

PROCYON also carried a scientific instrument named LAICA (Lyman Alpha Imaging CAmera), which aimed to image the geocoronal hydrogen Lyman-alpha emission spectra from deep space. In January 2015, the first image of Earth's entire hydrogen corona was obtained by LAICA, when the distance between PROCYON and Earth was 2,348 Re (shown in Figure 1.9) [*Kameda et al.*, 2017]. Right ascension and declination directions of PROCYON from Earth were 74.09, and -23.94 degrees, respectively. The spatial resolution was 1.34 Re / pix in the horizontal direction, and 0.98 Re / pix in the vertical direction. The total exposure time was 300 s. The image revealed that the hydrogen corona extends to about 40 Re in the anti-solar direction.

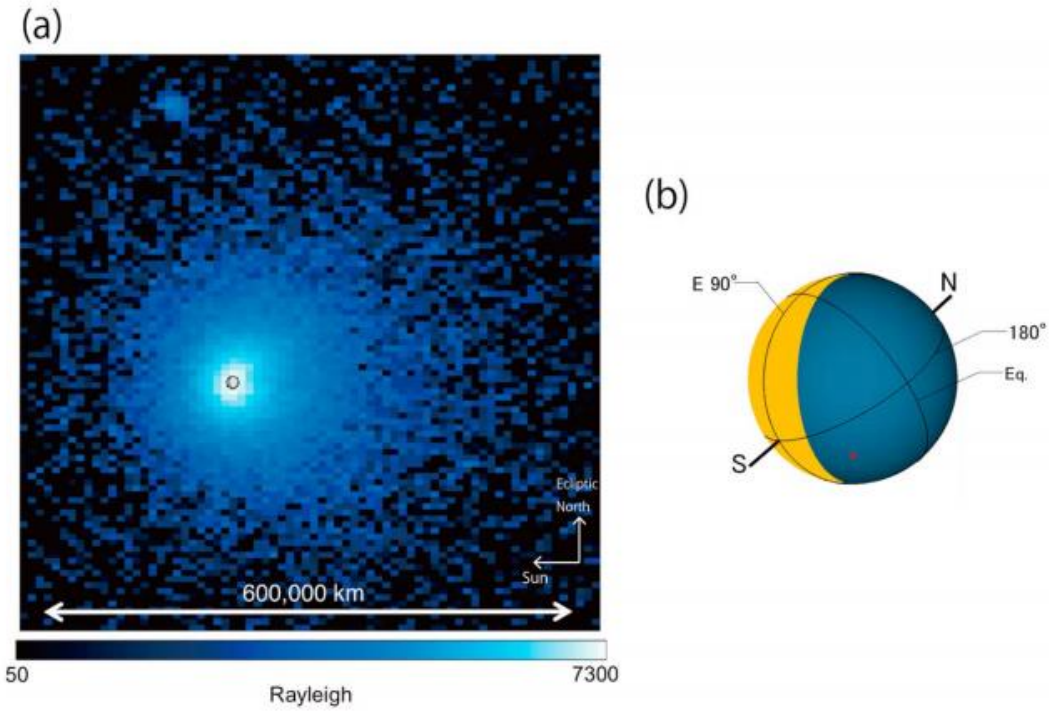

Figure 1.9. (a) First image of Earth's entire hydrogen corona. The image was acquired by subtracting the interplanetary background emission. The sun was on the left side of the image. Earth is located in the white circle near the center of the image and has a size of about 2 pixels. The geocoronal hydrogen corona can be clearly seen extending to ~40 Re in the direction of the night side of Earth. (b) Direction of the rotation axis and sunlit part of Earth during the observation. The red dot represents the location of the ecliptic south pole.

In addition to the observations of Earth, wide-field imaging observations of the hydrogen Lyman-alpha emissions from comet 67P/Churyumov-Gerasimenko were performed in September 2015 by LAICA and the water production rates of the comet were derived from the images [*Shinnaka et al.*, 2017]. The obtained values were comparable to those of the *in-situ* measurements by the Rosetta instruments and the ground and space-based observations.

These successes demonstrate the capabilities of ultra-small spacecraft for performing deep space missions and that they can be useful and strong tools for deep space exploration.

1.3. Organization of This Thesis

The purpose of this study is to develop techniques for ultra-small UV instruments. This thesis consists of 4 chapters. Chapter 2 presents the development of a helium ion imager, named PHOENIX, onboard the ultra-small deep space explorer, EQUULEUS. The optimization of the optics, especially the multilayer coated mirror, is detailed. Chapter 3 details the performance evaluation and development of new hydrogen absorption cells. The availability of the cell techniques for future ultra-small deep space explorations is also mentioned. Concluding remarks are given in Chapter 4. These applications are expected to lead to increase opportunities for future explorations with ultra-small spacecraft.

References

Broadfoot, A. L., Clapp, S. S., and Stuart, F. E. (1977). Mariner 10 ultraviolet spectrometer-Airglow experiment. *Space science instrumentation*, *3*, 199-208.

Burch, J. L., Mende, S. B., Mitchell, D. G., Moore, T. E., Pollock, C. J., Reinisch, B. W., Sandel, B. R., Fuselier, S. A., Gallagher, D. L., Green, J. L., Perez, J. D., and Reiff, P. H. (2001a). Views of Earth's magnetosphere with the IMAGE satellite. *Science*, *291*(5504), 619-624.

Burch, J. L., Mitchell, D. G., Sandel, B. R., Brandt, P. C., and Wüest, M. (2001b). Global dynamics of the plasmasphere and ring current during magnetic storms. *Geophysical research letters*, *28*(6), 1159-1162.

Carruthers, G. R. (1973). Apollo 16 far-ultraviolet camera/spectrograph: instrument and operations. *Applied optics*, *12*(10), 2501-2508.

Carruthers, G. R., Page, T., and Meier, R. R. (1976). Apollo 16 Lyman alpha imagery of the hydrogen geocorona. *Journal of Geophysical Research*, *81*(10), 1664-1672.

Funase, R., Inamori, T., Ikari, S., Ozaki, N., and Koizumi, H. (2015). Initial operation results of a 50kg-class deep space exploration micro-spacecraft PROCYON, 29th Annual AIAA/USU Conference on Small Satellites, SSC15-V-5, Logan, UT.

Hozumi, Y., Saito, A., Yoshikawa, I., Yamazaki, A., Murakami, G., Yoshioka, K., and Chen, C. H. (2017). Global distribution of the He^{+} column density observed by Extreme Ultra Violet Imager on the International Space Station. *Journal of Geophysical Research: Space Physics*, *122*(7), 7670-7682.

Kameda, S., Ikezawa, S., Sato, M., Kuwabara, M., Osada, N., Murakami, G., Yoshioka, K., Yoshikawa, I., Taguchi, M., Funase, R., Sugita, S., Miyoshi, Y., and Fujimoto, M. (2017). Ecliptic North‐South Symmetry of Hydrogen Geocorona. *Geophysical Research Letters*, *44*(23), 11,706-11,712.

Murakami, G., Yoshikawa, I., Obana, Y., Yoshioka, K., Ogawa, G., Yamazaki, A., Kagitani, M., Taguchi, M., Kikuchi, M., Kameda, S., and Nakamura, M. (2010). First sequential images of the plasmasphere from the meridian perspective

observed by KAGUYA. *Earth, Planets and Space*, *62*(4), e9-e12.

Murakami, G., Sakai, K., Homma, T., Yoshioka, K., Yoshikawa, I., Ichimaru, S., and Takenaka, H. (2011). Performance of Y2O3/Al multilayer coatings for the He-II radiation at 30.4 nm. *Review of Scientific Instruments*, *82*(3), 033106.

Murakami, G., Yoshikawa, I., Yoshioka, K., Yamazaki, A., Kagitani, M., Taguchi, M., Kikuchi, M., Kameda, S., and Nakamura, M. (2013). Plasmaspheric filament: an isolated magnetic flux tube filled with dense plasmas. *Geophysical Research Letters*, *40*(2), 250-254.

Nakamura, M., Yoshikawa, I., Yamazaki, A., Shiomi, K., Takizawa, Y., Hirahara, M., Yamashita, K., Saito, Y., and Miyake, W. (2000). Terrestrial plasmaspheric imaging by an extreme ultraviolet scanner on Planet‐B. *Geophysical research letters*, *27*(2), 141-144.

Sandel, B. R., Broadfoot, A. L., Curtis, C. C., King, R. A., Stone, T. C., Hill, R. H., Chen, J., Siegmund, O. H. W., Raffanti, R., Allred, D. D., Turley, R. S., and Gallagher, D. L. (2000). The extreme ultraviolet imager investigation for the IMAGE mission. In *The IMAGE Mission* (pp. 197-242). Springer, Dordrecht.

Sandel, B. R., King, R. A., Forrester, W. T., Gallagher, D. L., Broadfoot, A. L., and Curtis, C. C. (2001). Initial results from the IMAGE extreme ultraviolet imager. *Geophysical research letters*, *28*(8), 1439-1442.

Sandel, B. R., Goldstein, J., Gallagher, D. L., and Spasojevic, M. (2003). Extreme ultraviolet imager observations of the structure and dynamics of the plasmasphere. *Space Science Reviews*, *109*(1-4), 25-46.

Shinnaka, Y., Fougere, N., Kawakita, H., Kameda, S., Combi, M. R., Ikezawa, S., Seki, A., Kuwabara, M., Sato, M., Taguchi, M., and Yoshikawa, I. (2017). IMAGING OBSERVATIONS OF THE HYDROGEN COMA OF COMET 67P/CHURYUMOV–GERASIMENKO IN 2015 SEPTEMBER BY THE PROCYON/LAICA. *The Astronomical Journal*, *153*(2), 76.

Yoshikawa, I., Yamazaki, A., Shiomi, K., Yamashita, K., Takizawa, Y., and Nakamura, M. (2000a). Evolution of the outer plasmasphere during low geomagnetic activity observed by the EUV scanner onboard Planet‐B. *Journal of*

Geophysical Research: Space Physics, *105*(A12), 27777-27789.

Yoshikawa, I., Yamazaki, A., Shiomi, K., Yamashita, K., Takizawa, Y., and Nakamura, M. (2000b). Photometric measurement of cold helium ions in the magnetotail by an EUV scanner onboard Planet‐B: Evidence of the existence of cold plasmas in the near‐Earth plasma sheet. *Geophysical research letters*, *27*(21), 3567-3570.

Yoshikawa, I., Yamazaki, A., Shiomi, K., Yamashita, K., Takizawa, Y., and Nakamura, M. (2001). Interpretation of the He II (304 Å) EUV image of the inner magnetosphere by using empirical models. *Journal of Geophysical Research: Space Physics*, *106*(A11), 25745-25758.

Yoshikawa, I., Murakami, G., Ogawa, G., Yoshioka, K., Obana, Y., Taguchi, M., Yamazaki, A., Kameda, S., Nakamura, M., Kikuchi, M., Kagitani, M., Okano, S., and Miyake, W. (2010). Plasmaspheric EUV images seen from lunar orbit: Initial results of the extreme ultraviolet telescope on board the Kaguya spacecraft. *Journal of Geophysical Research: Space Physics*, *115*(A4).

Chapter 2. Development of the EUV Imager onboard EQUULEUS/PHOENIX

2.1. Introduction

In the Earth's upper atmosphere, charged particles, which are predominantly electrons and ions with energies below several electron volts, form a region of cold dense plasma trapped along geomagnetic field lines. This region is called the plasmasphere and extends regularly to ~4 Re (Re refers to the Earth's radius) from the Earth's center. The plasmaspheric He ions resonantly scatter solar radiation and emit EUV light at 30.4 nm. Since He ion is the second-most abundant component (~10%) of the plasmasphere, the emissions at a wavelength of 30.4 nm can be devoted to imaging the global plasmasphere. The acquired images are intensively used for studies on the dynamics and global structure of the plasmasphere [*Nakamura et al.*, 2000]. The plasmapause is a sharp outer boundary of the plasmasphere. The density of ions decreases by a factor of 100 or more across this boundary. The plasmapause does not locate at a fixed distance. It moves inwards during increased magnetic disturbances [*Carpenter*, 1963, 1966; *Taylor et al.*, 1965]. *Binsack* [1967] modeled the plasmapause location and explained it with the equation $L_{pp} = 6 - 0.6\,Kp$, where L_{pp} is the plasmapause location (unit: *L* value) and Kp is the geomagnetic activity index.

The NASA's Space Launch System (SLS) is a large rocket for carrying humans beyond the Earth's orbit. Furthermore, future manned space exploration of asteroids and Mars is being studied. The first flight of the SLS is scheduled to launch into the Moon fly-by orbit in 2019. Thirteen 6U-size secondary payloads ($10 \times 20 \times 30\,\mathrm{cm}^3$; 14 kg) will be onboard the SLS. EQUilibriUm Lunar-Earth point 6U Spacecraft (EQUULEUS), which is a nano-spacecraft designed and developed by the JAXA (Japan Aerospace Exploration Agency) and the University of Tokyo, is selected as one of the secondary payloads. EQUULEUS aims to reach a libration orbit around the Earth-Moon Lagrange point L2 (EML2) and demonstrates engineering technologies.

This mission also carries several scientific instruments. The first instrument, Plasmaspheric Helium ion Observation by Enhanced New Imager in eXtreme ultraviolet (PHOENIX), will conduct extreme ultraviolet (EUV) imaging of the Earth's plasmasphere throughout the mission phases. The second instrument, Cis-Lunar Object detector within THermal insulation (CLOTH), was installed in the multi-layer insulation of the spacecraft. It will detect and evaluate the meteoroid impact flux in the cis-lunar region. This mission aims to understand the size and spatial distributions of solid surface in the cis-lunar region. The third instrument, DEtection camera for Lunar impact PHenomena IN 6U Spacecraft (DELPHINUS), will observe the back side of the Moon for impact flashes. This observation will characterize the flux of meteorites. The results of this mission will contribute towards the evaluation of risks associated with future human activity and/or infrastructure on the lunar surface.

In this chapter, the development of the EUV telescope, PHOENIX, and its calibrated performance are described. PHOENIX will observe the distribution of plasma that surrounds Earth by detecting emissions of He II (30.4 nm). By flying away from Earth, PHOENIX can obtain an entire image of the plasmasphere. The image from the equatorial plane helps scientists understand plasma dynamics along magnetic field lines. Plasma behavior is related to solar activity and is the key to understanding of the physics and evolution of the Earth's space environment.

2.2. Scientific Objectives of PHOENIX

PHOENIX will provide information on the global distribution of plasma around Earth by detecting emissions scattered by He ions (He II) at 30.4 nm. In the following subsections, the scientific objectives of PHOENIX are described. The observation target is the plasmasphere.

When a solar wind disturbance arrives at Earth, the magnetospheric convection electric field becomes stronger. Then, the outer layer of the plasmasphere is stripped away and the plasmasphere shrinks under the influence of $E \times B$ drift [*Grebowsky*, 1970, 1971; *Chen and Wolf*, 1972]. This phenomenon is known as erosion. The sharp

outer boundary of the plasmasphere, the plasmapause, starts to move subsequently. After the plasmapause evolves, the magnetospheric convection electric field becomes weaker and the ionosphere supplies plasma to the plasmasphere. This process is known as plasmaspheric refilling and lasts for several hours or days.

2.2.1. Global Plasmaspheric Image

The plasmasphere extends to ~4 Re from the center of Earth, and it is observed within a field of view by approximately ± 4 degrees when viewed from the Moon. *Nakamura et al.* [2000] reported that the intensity of He II (30.4 nm) emission from the main body of the plasmasphere is ~5 Rayleigh. This value is consistent with those (1-10 Rayleigh) measured by using sounding rockets [*Ogawa and Tohmatsu*, 1971] and reported by numerical simulations [*Roelof et al.*, 1992]. The intensity of emissions scattered by He ions near the plasmapause was reported to be in the range of 0.1-0.5 Rayleigh based on measurements by the NOZOMI satellite [*Yoshikawa et al.*, 2000a]. Therefore, I consider this value as the lower threshold level to capture the global structure of the plasmasphere.

2.2.2. Plasmaspheric Erosion

Plasmaspheric erosion occurs when geomagnetic activity increases. Then, the plasmapause, which is defined as the sharp outer boundary of the plasmasphere, changes its outer shape. The mean speed of its inward motion is 0.2-0.3 Re/h. This phenomenon is important for quantifying the material removed from the plasmasphere during disturbance periods. *Spasojevíc and Sandel* [2010] calculated the global loss of plasmaspheric ions from the data recorded by the EUV instrument onboard the IMAGE satellite. The EUV instrument measured the fraction of He ions in the plasmasphere, which is a tracer of the total plasmaspheric ion content. It was found $\sim 0.6 \times 10^{30}$ to 2.2×10^{30} He ions were removed from the plasmaspheric region between L = 1.5 to 5.5 Re during a moderate disturbance period. These losses accounted for 20-42% of the

initial plasmaspheric He ion content.

The plasmasphere was observed from a meridian perspective with the EUV imager onboard KAGUYA during a geomagnetic disturbance period on May 1-2, 2008. This clearly revealed that the plasmapause location in the midnight sector is consistent with that predicted by dynamic simulations based on the interchange mechanism. Furthermore, night side column density of He ion decreased by ~30% at low latitudes (< 20 degrees) following convection enhancement. This decrease in column density was consistent with the formation of the plasmapause by the quasi-interchange instability mechanism. However, since there are few observations to prove the existence of the quasi-interchange instability mechanism, further investigation is required.

A geomagnetic storm, which is a major geomagnetic disturbance phenomenon, occurs when the interplanetary magnetic field turns southward. The main phase of this phenomenon, which is associated with an increase in geomagnetic activity, lasts for several hours. Then, the geomagnetic activity decreases gradually over several hours or days, which is known as the recovery phase. Therefore, the temporal resolution of PHOENIX should be at least 1 hour for investigations of plasmaspheric erosion.

2.2.3. Plasmaspheric Refilling

During the recovery phase of geomagnetic storms, the plasmasphere is refilled by ionospheric plasma over several hours or even days. This process can last for several days and modifies electron and mass densities along magnetic field lines. Therefore, the plasmasphere becomes denser and larger.

There are unresolved issues associated with the plasmasphere refilling process. Scientific studies on plasmaspheric refilling have been carried out since the 1960s and early 1970s. Observational studies [*Park*, 1970; *Chappell et al.*, 1971] and theoretical and/or modeling studies [*Banks et al.*, 1971; *Grebowsky*, 1971; *Schulz and Koons*, 1972; *Chen and Wolf*, 1972] have addressed various refilling issues.

Related observations by ATS 6 [*Horwitz*, 1980; *Comfort and Horwitz*, 1981], GEO 1 [*Farrugia et al.*, 1989] and 2 [*Higel and Wu*, 1984; *Sojka and Wrenn*, 1985],

ISEE 1 [*Nagai et al.*, 1985; *Carpenter and Anderson*, 1992], and SCATHA [*Olsen et al.*, 1987], provided interesting information about the characteristics of cold and warm plasma in the outer plasmasphere and plasma trough.

Refilling investigations have increased since the mid-1980s. Theoretical/modeling studies using thermal plasma measurements from the Dynamics Explorer mission [*Horwitz et al.*, 1984, 1986, 1990a, 1990b; *Décréau et al.*, 1986; *Gallagher et al.*, 1988] provided new and intriguing results.

By using IMAGE data, *Sandel* [2011] found that the ratio of He ion density to electron density in the plasmasphere was nearly constant with a typical L value of ~0.09. This ratio was more variable during the early stages of the refilling process than during the later stages. This suggests that difference in ion species causes variation in refilling rates from the ionosphere.

KAGUYA observed the plasmasphere intermittently for only about 26 days in 2008 [*Murakami*, private communication]. Since continuous and long-term observations could not be conducted during the KAGUYA mission, the long-term structural variation of the plasmasphere in response to geomagnetic disturbances and plasmaspheric refilling during the recovery phase could not be observed.

Observational and theoretical and/or modeling studies have been carried. One of the earliest theoretical studies was conducted by *Banks et al.* [1971]. They used a single-stream hydrodynamic model. This study is still widely cited since it indicates the basic characteristics of refilling. *Rasmussen and Schunk* [1988] adopted a two-stream model for plasmaspheric refilling. A kinetic approach to the study of refilling was reviewed and expanded by *Khazanov et al.* [2012].

One of the unresolved issues of refilling is that there are scarce observational results to support the models that are based on the initial conditions in an empty magnetic flux tube, such as plasma density, flow velocity, and temperature [*Singh and Horwitz*, 1992]. PHOENIX can continuously observe the plasmasphere. An observation period of at least 1 year will reveal the long-term behavior of the plasmasphere from the meridian perspective. PHOENIX takes advantage of this superiority to observe the plasmaspheric refilling process during geomagnetic disturbance periods. Latitudinal

distributions of He ions during refilling periods can be obtained from PHOENIX observations. These results will determine the initial conditions of the models.

PHOENIX will start observations in 2019. Since solar activity varies on an 11-year cycle, I assumed that the solar activity in 2019 will be comparable to that in 2008. Assuming that a geomagnetic disturbance with difference in geomagnetic activity (*Dst* index) of 40 nT or more is a geomagnetic storm, 23 geomagnetic storms occurred in 2008. Therefore, PHOENIX is expected to observe the plasmaspheric refilling process more than 20 times. Assuming that geomagnetic storms occur twice a month on average, a continuous observation period of 15 days will be required to capture the full scope of the plasmaspheric variation induced by a geomagnetic disturbance. KAGUYA could perform continuous observations for an average period of 4.3 days only. However, PHOENIX can observe the plasmasphere continuously for more than 15 days.

2.2.4. Plasmaspheric Filament

Recently, the IMAGE mission identified several novel plasmaspheric structures. (for instance, a depleted region called notch, a sharp azimuthal gradient in He ion density called shoulder, and a radial structure of enhanced brightness called finger). The finger structure was observed during a geomagnetically quiet period and has been interpreted as an isolated flux tube that is filled to higher density than neighboring tubes [*Sandel et al.*, 2001]. Such flux tubes viewed from above the Earth's north pole were projected onto the magnetic equator plane and observed to have a finger-like appearance. The first EUV imaging observation of the plasmasphere from the meridian perspective was recorded by the TEX onboard KAGUYA in 2008 [*Murakami et al.*, 2010]. By the TEX instrument, plasmaspheric filament structures were observed during prolonged quiet periods [*Murakami et al.*, 2013]. *Murakami et al.* [2013] suggested that these structures are equivalent to the finger structures observed by IMAGE/EUV. They found only four events of plasmaspheric filament and the physical process involved in the formation of this plasmaspheric filament has still not been understood. *Murakami et al.* [2013] investigated the spatial structure of the plasmaspheric filament viewed from the

Moon. They found that spatial width of this filament was ~0.3 Re. Thus, a spatial resolution of at least 0.3 Re or less is required to examine this structure. The black lines in Figure 1.8 represent magnetic field lines, assuming dipole magnetic field lines. *Murakami et al.* [2013] suggested that the loop structures are caused by isolated magnetic flux tubes that are filled with higher plasma densities than their neighbors. The red dashed lines emphasize the loop structures in this study. However, it is difficult to interpret these lines as they are along the magnetic field lines. For further verification and comprehension, it is necessary to obtain statistically significant data of the plasmaspheric filament, which is a key to understanding of the plasmasphere-ionosphere coupling effect, especially the physical process of plasmasphere refilling.

The key to obtaining such data is to develop a highly efficient EUV optical system. In particular, the technique of developing multilayer coated mirrors, which have high reflectivities in the EUV range, is important [*Yoshikawa et al.*, 1997]. The capabilities of instruments equipped with multilayer coated mirrors have been already demonstrated by the NOZOMI [*Yoshikawa et al.*, 2001] and KAGUYA [*Yoshikawa et al.*, 2008] missions. In this study, I focused on the technique of multilayer coating and developed a new mirror by using a Mg/SiC material combination. This mirror has a higher reflectivity for He II (30.4 nm) emission than previously developed mirrors. This multilayer coated mirror of Mg/SiC was installed as the flight mirror in the optical system of PHOENIX.

2.3. Instrumental Overview

PHOENIX is a type of normal incidence telescope and comprised of a multilayer coated mirror, a metallic thin filter, a microchannel plate (MCP) detector, and electronic components. Figures 2.1 and 2.2 show the schematic diagrams of this instrument and its main features are summarized in Table 2.1. The light from the target is focused by a spherical mirror, whose sensitivity is optimized at a wavelength of 30.4

nm, and passes through a filter, which eliminates undesired light (i.e., geocoronal and interplanetary emissions). After the light passes through the filter, a two-dimensional photon counting detector converts the light into electrical signals. The design of the telescope is similar to those of KAGUYA/TEX [*Yoshikawa et al.*, 2008, 2010; *Murakami et al.*, 2010] and ISS-IMAP/EUVI [*Hozumi et al.*, 2017]. The detailed design and ground calibration results of each component are described below.

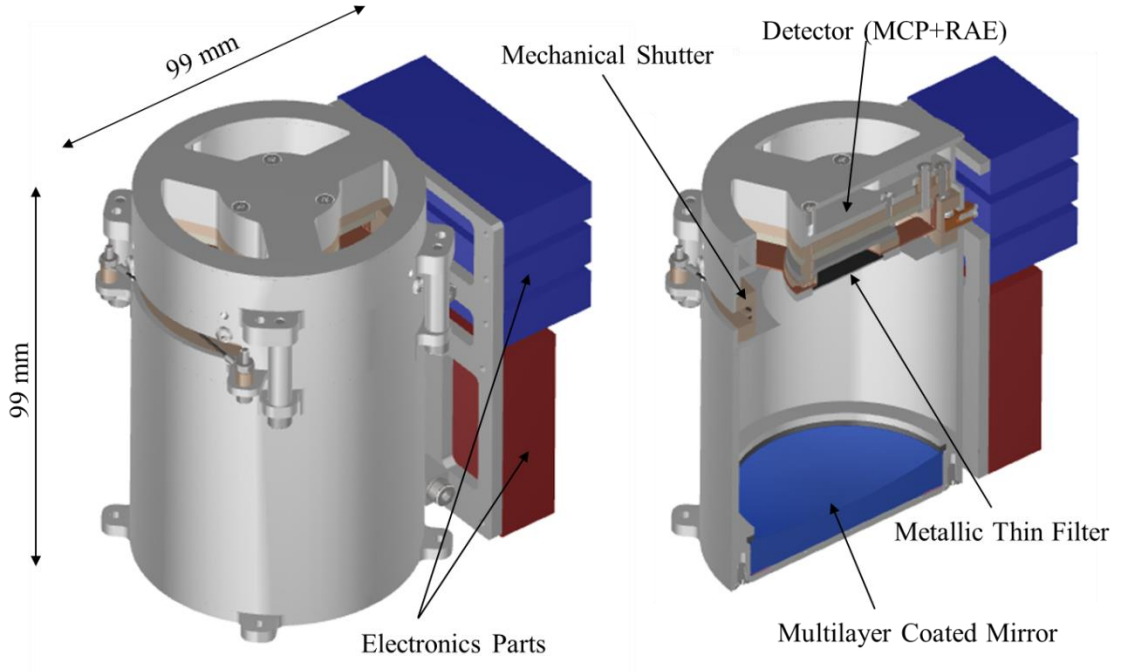

Figure 2.1. Schematic diagram of PHOENIX. Its main components are a multilayer coated mirror, a metallic thin filter, a detector, and electronics components. To prevent sunlight from entering the filter and detector, a mechanical shutter was installed in front of the metallic thin filter.

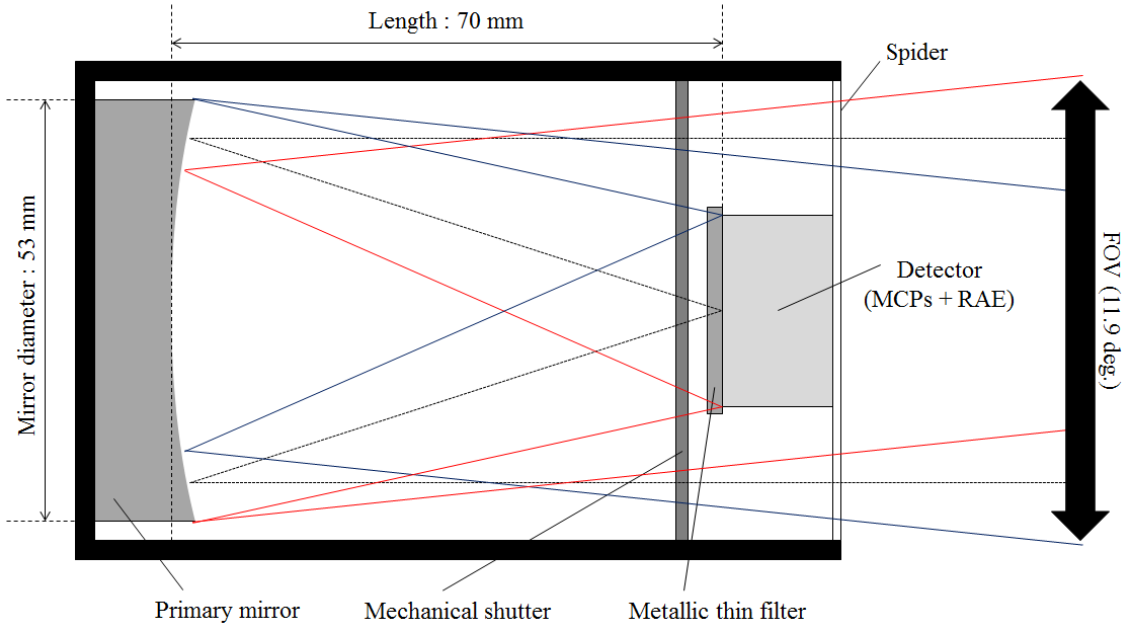

Figure 2.2. Cross-sectional diagram of the optical layout of PHOENIX. The diameter and focal length of the mirror are 53 mm and 70 mm respectively. The field of view (FOV) of PHOENIX is 11.9 degrees.

Table 2.1. Specifications of PHOENIX

Target Wavelength	30.4 nm (He II)
Angular Resolution	~0.15 deg. (~0.15 Re from the Moon's orbit)
Temporal Resolution	< 1 h
Field of View	$11.9 \times 11.9\,\mathrm{deg.}^2$
Data Format	$256 \times 256\,\mathrm{bin}^2$
Mass	532.5 g
Size	$66 \times 99 \times 99\,\mathrm{mm}^3$
Open Aperture	$11.66\,\mathrm{cm}^2$

2.4. Multilayer Coated Mirror

The entrance mirror is one of the most important factors that determine the performance of an EUV optical system. The efficiency of this mirror depends on its effective area and reflectivity. However, it is quite difficult to equip with a light entrance

because the allowable envelope of PHOENIX is small ($66 \times 99 \times 99\,\mathrm{mm}^3$). Therefore, to ensure successful scientific observations during missions by ultra-small spacecraft, the efficiency of the entrance mirror should be improved.

The technique of periodic multilayer coatings has been developed in recent years for normal incidence optics in the soft X-ray and EUV spectral regions. A multilayer coated mirror is an optical element, in which two kinds of materials that have different complex refractive indices are overlaid periodically and alternately on the surface of a mirror. The reflectivity of such a mirror can be dramatically improved by the interference of reflected light at each interface. The response of the coating can be adjusted by adjusting the multilayer period d (i.e., thickness of the layer) according to the Bragg's law $n\lambda = 2d\cos\theta$, where θ is the incident angle of light and n is the Bragg order. In order to control the spectral response of the coating, the number of periods N and thickness ratio of each constituent material Γ can also be adjusted.

In space and planetary sciences, this technique for EUV radiation has been used for a number of missions. High reflectivity multilayer coatings for He II radiation at a wavelength of 30.4 nm have been developed for some of these applications [*Sandel et al.*, 2000; *Yoshikawa et al.*, 2008]. The Mo/Si multilayer coated mirror has been widely used because of its high stability [*Yamashita et al.*, 1992; *Kunieda et al.*, 1996; *Yoshikawa et al.*, 1997; *Yoshikawa et al.*, 2001; *Sandel et al.*, 2001]. The reflectivity of the Mo/Si multilayer coated mirror installed on the TEX onboard KAGUYA was 18.8% at a wavelength of 30.4 nm [*Yoshikawa et al.*, 2008]. After this mission, a Y_2O_3/Al multilayer coated mirror was installed in ISS-IMAP/EUVI in order to achieve high reflectivity and avoid contamination from geocorona. The reflectivity of this mirror was 23% at 30.4 nm [*Murakami et al.*, 2011]. The planetary science community should develop multilayer coatings with higher reflectivities for optical system applications.

In this study, a multilayer coated mirror with higher reflectivity for He II radiation (30.4 nm) than previously developed mirrors was used in order to minimize deterioration of the efficiency of an instrument due to its miniaturization. Sample mirrors with three types of Mg/SiC multilayer coatings were fabricated and evaluated. The performances of each sample mirror under different parameters are reported in this

chapter. The secular stabilities of the reflectivities of the mirrors in different storage environments are also shown.

2.4.1. Designs and Calculations

In order to decide a combination of materials applied to a multilayer coated mirror to be installed in PHOENIX, reflectivities of various multilayer coatings were calculated by using conventional method with characteristic matrix. In the circumterrestrial space, there are not only He II (30.4 nm) radiation but also He I (58.4 nm), O II (83.4 nm), and H I (121.6 nm) radiations. These radiations possibly contaminate acquired images of the PHOENIX mission. In this work, I selected materials whose optical constants are available for the wavelengths of 30.4, 58.4, 83.4, and 121.6 nm and evaluated reflectivities of each combination for the 30.4 nm light. Table 2.2 and 2.3 show materials and their optical constants (refractive index n and extinction coefficient k) used in this study. Generally, in order to increase reflectivity, it is important that complex refractive indices $n-ik$ at the target wavelength of two materials are separated from each other and each k is small [e.g., *Hotta et al.*, 2002]. If k of two materials are small, a reflectivity tends to increase with increase in N. In other words, the combination of the two materials with small k suppresses attenuation of reflected light from deep interfaces and increases efficiency of interference. Considering the above two conditions, I summarized the materials that are expected to improve in the reflectivity into Table 2.2 (materials with relatively large n values at 30.4 nm) and Table 2.3 (materials with relatively small n values). However, the combination of the optimum materials cannot be determined without calculation. Therefore, I calculated the reflectivities of all the combinations between 7 materials in Table 2.2 and 6 materials in Table 2.3. In this calculation, I considered the layer thickness d, the number of periods of the laminated layer N, and the thickness ratio of two materials Γ as parameters that determine the reflectivity of the multilayer coating. The optimum values were searched three-dimensionally with the ranges and grid sizes of the parameters described in Table 2.4. The detail of the calculation of the reflectivity

is written in Appendix A.

Table 2.2. Optical constants at 30.4 nm of various materials with large n value

Material	n (at 30.4nm)	k (at 30.4nm)
Li	0.99	0.0017
Cs	0.96	0.0058
Mg	0.98	0.0083
Al	0.94	0.0079
Sn	1.06	0.11
ZnS	0.94	0.052
KCl	0.94	0.019

Table 2.3. Optical constants at 30.4 nm of various materials with small n value

Material	n (at 30.4nm)	k (at 30.4nm)
Ca	0.85	0.16
C	0.81	0.084
Fe	0.85	0.101
Co	0.82	0.15
Os	0.77	0.11
SiC	0.85	0.045

Table 2.4. Parameters used for calculations.

Parameter	Range	Grid Size
Layer Thickness, d	15.0-17.0	0.1
Number of Periods, N	10-100	10
Thickness Ratio, Γ	0.1-0.9	0.1

The reflectivities at 30.4 nm for the incident angle of 4 degrees, which is determined by the location of the outer boundary of the plasmasphere, plasmapause,

viewed from PHOENIX located near the Moon, were calculated for all the combinations as described above and are summarized in Table 2.5. The parameter sets having the highest reflectivities for the wavelength of 30.4 nm for each combination were selected as optimum values. In Table 2.5, $R_{30.4}$, $R_{58.4}$, $R_{83.4}$, and $R_{121.6}$ represent the reflectivities at the wavelengths of 30.4 nm, 58.4 nm, 83.4 nm, and 121.6 nm, respectively. Figure 2.3 shows the calculated reflectivities of various multilayer coatings which have high reflectivities over 40% at 30.4 nm for the normal incidence of 4 degrees. The multilayer coatings using Li perform higher reflectivities than any other combinations in my calculation and subsequent candidates are the combinations of Cs/Os and Mg/Os. However, it is difficult to handle Li, Cs, and Os. I excluded the combinations with Li, because Li has a property to ignite spontaneously when mixed with a large amount of water. Cs has a low melting point (~300 K) and is in a liquid state around the room temperature. Therefore, I also removed the combinations with Cs from the candidates. Os should be excluded because it has a property of easily producing poisonous osmium oxide when it is left in the air or heating.

As cited above, I have concluded that Mg/SiC is the best combination for the flight mirror because it achieves the high reflectivity of 43% at the wavelength of 30.4 nm for the normal incidence of 4 degrees

.

Table 2.5. Reflectivities of combinations of various materials

Materials	Number of Periods (N)	Layer Thickness (d) [nm]	Thickness Ratio $(SiC/d, \Gamma)$	$R_{30.4}$	$\frac{R_{30.4}}{R_{58.4}}$	$\frac{R_{30.4}}{R_{83.4}}$	$\frac{R_{30.4}}{R_{121.6}}$
Li/Ca	100	15.4	0.2	0.499	298.61	149.46	16.59
Li/C	100	15.5	0.2	0.614	39.54	15.80	70.77
Li/Fe	100	15.4	0.2	0.529	85.79	33.44	11.41
Li/Co	90	15.4	0.2	0.526	76.28	24.77	7.96
Li/Os	100	15.5	0.2	0.626	19.59	36.68	15.10
Li/SiC	100	15.5	0.2	0.643	52.13	9.96	3.17
Cs/Ca	100	15.9	0.2	0.315	179.18	27.67	173.33
Cs/C	90	16.1	0.3	0.423	7.87	4.10	9.86
Cs/Fe	100	16.0	0.3	0.317	12.56	5.79	6.50
Cs/Co	90	16.0	0.2	0.345	25.84	7.83	8.72
Cs/Os	80	16.2	0.3	0.447	4.86	6.97	8.41
Cs/SiC	100	16.1	0.3	0.432	9.82	3.54	1.79
Mg/Ca	70	15.7	0.3	0.299	94.52	29.27	0.81
Mg/C	80	15.9	0.3	0.418	9.44	4.68	48.95
Mg/Fe	80	15.8	0.3	0.316	19.15	7.33	2.31
Mg/Co	70	15.8	0.3	0.331	19.24	6.03	2.09
Mg/Os	70	15.9	0.3	0.439	5.52	10.43	4.04
Mg/SiC	**80**	**16.0**	**0.4**	**0.433**	**6.92**	**1.72**	**1.15**
Al/Ca	70	16.4	0.3	0.254	156.69	3.72	0.31
Al/C	90	16.5	0.3	0.348	6.70	3.17	10.28
Al/Fe	90	16.4	0.3	0.249	17.91	3.04	0.82
Al/Co	80	16.4	0.3	0.282	24.67	3.29	0.99
Al/Os	60	16.6	0.3	0.383	4.65	7.26	1.56
Al/SiC	90	16.6	0.4	0.329	3.76	0.97	0.79

Table 2.5. Reflectivities of combinations of various materials (continued)

Materials	Number of Periods (N)	Layer Thickness (d) [nm]	Thickness Ratio $(SiC/d, \Gamma)$	$R_{30.4}$	$\frac{R_{30.4}}{R_{58.4}}$	$\frac{R_{30.4}}{R_{83.4}}$	$\frac{R_{30.4}}{R_{121.6}}$
Sn/Ca	20	15.1	0.4	0.100	10.86	5.70	0.20
Sn/C	20	15.8	0.5	0.172	1.62	1.03	3.84
Sn/Fe	20	15.4	0.5	0.112	2.51	1.24	0.43
Sn/Co	20	15.2	0.4	0.119	3.66	1.29	0.40
Sn/Os	10	15.0	0.1	0.037	3.58	0.67	0.08
Sn/SiC	20	15.8	0.5	0.185	2.08	0.57	0.41
ZnS/Ca	30	16.8	0.4	0.084	17.32	1.29	0.29
ZnS/C	40	16.9	0.4	0.125	1.07	0.68	1.69
ZnS/Fe	40	16.7	0.4	0.07	1.47	0.54	0.29
ZnS/Co	30	16.9	0.4	0.101	2.27	0.70	0.38
ZnS/Os	20	16.9	0.4	0.159	1.00	1.37	0.72
ZnS/SiC	40	16.9	0.5	0.108	0.67	0.30	0.24
KCl/Ca	50	16.5	0.3	0.163	7.16	6.75	3.94
KCl/C	10	15.0	0.1	0.008	0.07	0.15	0.18
KCl/Fe	60	16.6	0.4	0.148	1.49	1.62	1.19
KCl/Co	60	16.6	0.3	0.185	2.25	2.11	1.42
KCl/Os	50	16.9	0.4	0.268	1.29	2.79	2.11
KCl/SiC	80	16.7	0.4	0.207	0.90	0.86	0.61

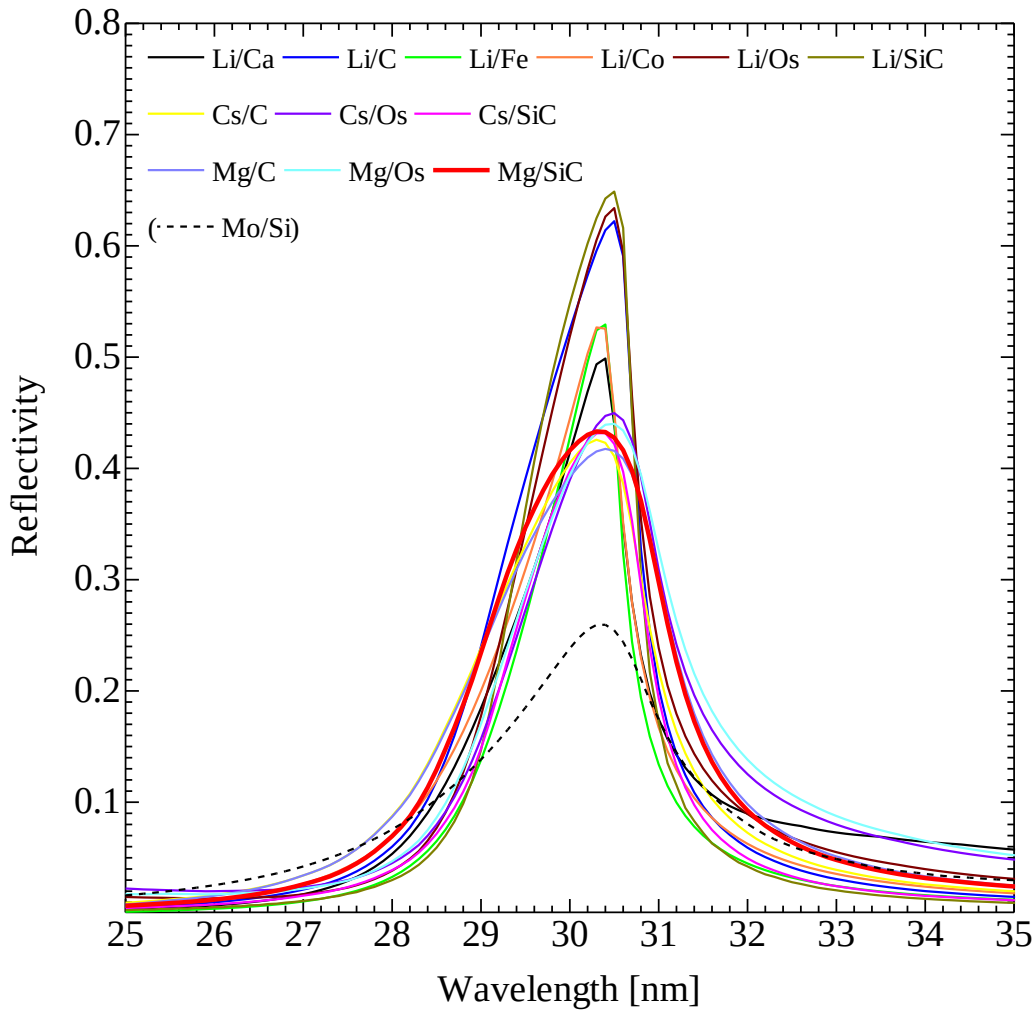

Figure 2.3. Calculated Reflectivities (> 40%) of the various multilayer coatings for the normal incidence of 4 degrees. The parameters, N, d, and Γ, were optimized for normal incidence light at the wavelength of 30.4 nm. The variable parameters of each combination were optimized values. Reflectivities of the conventional Mo/Si mirror are also shown.

Figure 2.4 shows the relationship between the calculated reflectivity at 30.4 nm and the number of periods N with d of 16.0. It is obvious that the reflectivity is saturated at more than 30 layers. Since reflected light from deep interfaces decreases in amplitude with increase in N, the peak reflectivity tends to be saturated. From this result, I concluded that the number of periods of 30 is sufficient for the Mg/SiC

multilayer coated mirror.

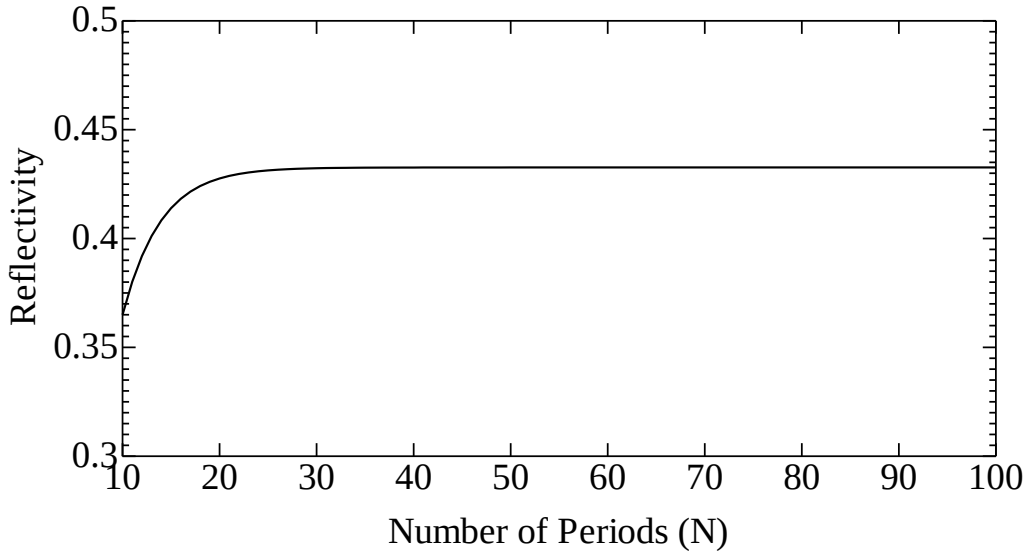

Figure 2.4. Relationship between the calculated reflectivity at 30.4 nm and the number of periods N . The reflectivity is saturated at more than 30 periods.

Figure 2.5 shows the calculated reflectivity of Mg/SiC coatings at 30.4 nm with various Γ values. The reflectivity peaks with d of 15.8-16.0 and Γ of 0.3-0.4. Considering the results in Figure 2.4 and 2.5, I concluded that the parameters, such as d of 15.8-16.0, Γ of 0.3-0.4, and N of 30, are required for the Mg/SiC mirror which has a high reflectivity at the wavelength of 30.4 nm.

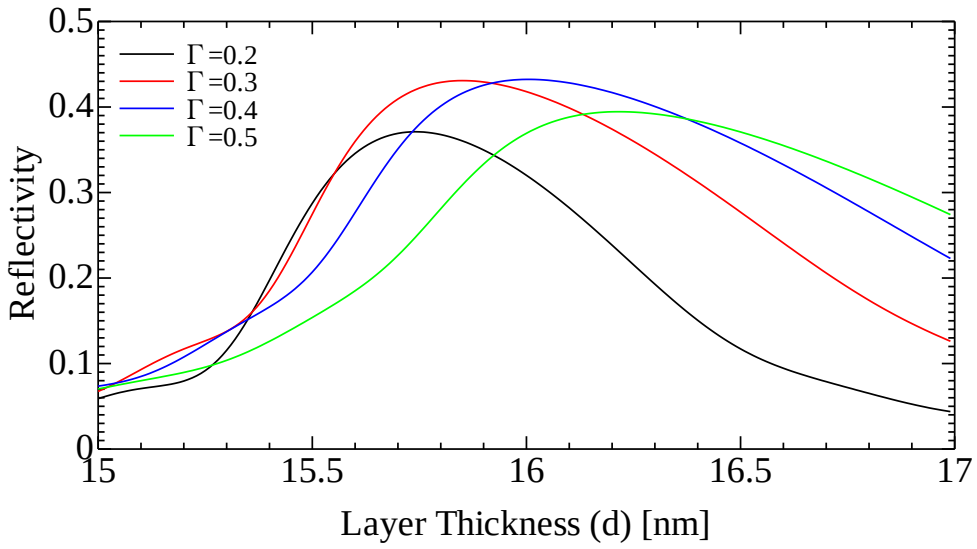

Figure 2.5. Relationship between the calculated reflectivity at 30.4 nm and the layer thickness d with different Γ. The reflectivity appears to be the highest with d of 15.8-16.0 and Γ of 0.3-0.4.

2.4.2. Previous Studies of Mg/SiC multilayer coatings

Takenaka et al. [2005] fabricated Mg/SiC multilayer coatings with peaks of reflectivities at the wavelength of 30 nm by magnetron sputtering for use in EUV photoelectron microscopy and reported that they have high reflectivities over 40% for near normal incidence.

Yoshikawa et al. [2005] also designed multilayer coatings of pairs of Mg/SiC and evaluated their reflectivities. As a result, it was reported that the coatings have high reflectivities for the wavelength of 30.4 nm.

Soufli et al. [2005] investigated temporal changes of reflectivities of Mg/SiC multilayer coatings for the wavelength of 30.4 nm. The reflectivities decreased by ~4% by the atmospheric exposure of 5 months.

Ejima et al. [2005] made reflection measurements in the 25-35 nm region for

Mg/SiC and Mg/Y_2O_3 multilayer coatings. They were kept in a low humidity atmosphere (< 50%) for 4 or 5 years. As for these reflectivities, no significant change compared to ones measured immediately after deposition was confirmed. It was thought that the storage environment prevented the top Mg layer from the reaction with an atmosphere.

Zuccon et al. [2006] investigated the performances of Mg/SiC multilayer coatings with or without Si cap layers on the top surface of the Mg/SiC coatings. Although the reflectivities for 30.4 nm light of multilayers without any Si cap layer were lower than the calculated values, those with the Si cap layers achieved high reflectivities close to the calculated values.

The performance of an Mg/SiC multilayer coating and the aging in reflectivity under atmosphere and vacuum were reported by *Toyota et al.* [2007]. As a result, the aging appeared under atmosphere, but the reduction in reflectivity could be suppressed under vacuum. They suggested that the difference between the calculation and the result of the measurement indicates the elements of the multilayer coating become opaque under atmosphere after the deposition.

Two types of multilayer coatings of Mg/SiC and B_4C/Mo/Si were deposited and evaluated their reflectivities by *Zhu et al.* [2008]. These coatings achieved high reflectivities of 38% and 32.5% at the wavelength of 30.4 nm, respectively. In addition, it was reported that fitted results of measured reflectivity of the Mg/SiC multilayer coating indicate a large amount of interface roughness.

Zhu et al. [2010] deposited multilayer coatings of Mg/SiC, Mg/Co, Mg/B_4C, and Mg/Si and measured reflectivities of them for 30.4 nm light. Mg/Co and Mg/SiC multilayer coatings achieved high reflectivities of 40.3% and 44.6%, respectively, while those of Mg/Si and Mg/B_4C coatings were too low (5.6% and 0.2%, respectively) for application.

Pelizzo et al. [2012] used Mg/SiC multilayer coatings to mirrors for rocket observation. In addition, they prepared several types of multilayer coatings and investigated long-term stabilities of them over 4 years. As a result, significant surface modifications were observed in the coatings. It is suggested that the expansion due to

reaction of Mg with an atmosphere causes the modifications. They measured reflectivities of the aged coatings and compared them to ones measured immediately after deposition. Although the reflectivities for 121.6 nm and visible light were affected by deterioration, some coatings did not change reflectivities for EUV. All the multilayer coatings with an Si top layer were degraded, while there were no changes in those with an SiC top layer deposited over the last SiC layer. It is also suggested that the thickness of each Mg layer affects the deterioration of Mg/SiC multilayer coatings.

Soufli et al. [2012] and *Fernández-Perea et al.* [2012] suggested that an Al-Mg layer which is deposited on top of an Mg/SiC multilayer coating provides efficient corrosion protection. The demonstration of Mg/SiC multilayer coatings with corrosion resistance is great interest in the development of mirrors for space missions.

As cited above, the application of multilayer coatings of pairs of Mg and SiC having a high reflectivity for the wavelength of 30.4 nm to EUV optics was reported by previous researchers. However, the stability of Mg/SiC multilayer coating has been investigated insufficiently and there is no consensus on it. Therefore, further detailed examinations have been needed to mount in the spacecraft. In this work, in order to overcome this issue, the stabilities of Mg/SiC coatings were investigated in detail through four storage environments.

2.4.3. Reflectivity Measurement of Sample Mirrors

I have found that the calculation using optical constants of Mg and SiC shows the high reflectivity of 43 % at the wavelength of 30.4 nm as shown in Figure 2.3. Therefore, in this study, I fabricated sample mirrors of 3 types of Mg/SiC multilayer coatings (No.1-3) and evaluated the performances of them. The designs of the samples are listed in Table 2.6. The sample coatings, which were periodic 30 pairs of Mg and SiC on flat planes with various d , and Γ , were deposited by an ion-beam sputtering system. The parameters of the samples were aimed for normal incidence reflection.

There are 4 flat sample plates for each sample. All the sample coatings were manufactured by the NTT Advanced Technology Corporation.

Table 2.6. Designs of sample Mg/SiC multilayer coatings

Sample Number	Number of Periods (N)	Multilayer Period (d) [nm]	Thickness Ratio (Γ : SiC/d)
No. 1	30	15.85	0.3
No. 2	30	15.90	0.4
No. 3[a]	30	15.86	0.4

[a]Surface SiC is twice as thick as other samples.

Figure 2.6 shows the setup of reflectivity measurements of the sample mirrors. The system consists of a windowless RF excited flow lamp filled with various source gases and connected to a JOVIN YVON LHT30 30-cm scanning monochromator. The monochromator provides radiation of spectral lines particularly in light source gas. In a vacuum chamber, the mirrors were located on an XYZ translation stage with a rotation stage with single axis aligned perpendicularly to an incident beam. The incident and reflected beams were alternately detected by a photon detector consisting of 5-stack microchannel plate (MCP) and a resistive anode encoder (RAE). The reflectivity was evaluated by comparing the intensities of each beam and can be measured for the incident angle of more than only 4 degrees due to configuration constraint in the facility.

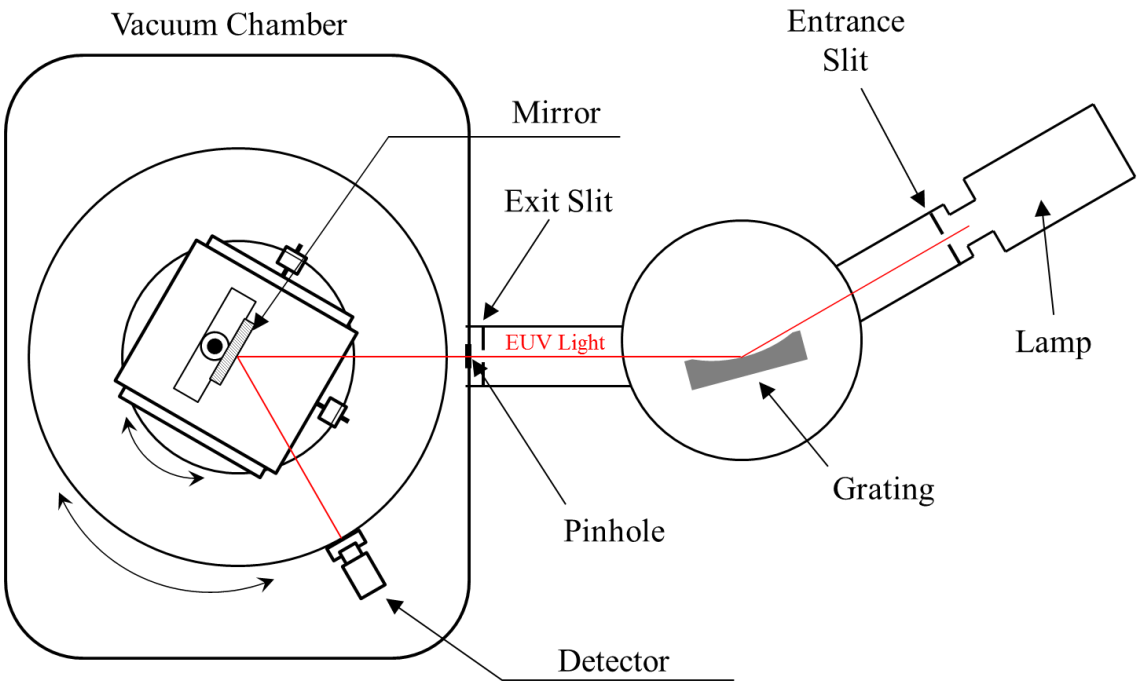

Figure 2.6. Setup of the measurement configuration. A discharge lamp is used as an EUV light source and the target line is selected by a monochromator. The monochromatic light is collimated by a pinhole at the entrance of the vacuum chamber. An assembly of a 5-stack microchannel plate (MCP) and a resistive anode encoder (RAE) is used as a detector.

I measured the reflectivities of the samples at the wavelength of 30.4 nm as a function of an incident angle from the normal incidence. Figure 2.7 shows the results of the experiments. The theoretical calculations of the reflectivities are also shown. At the incident angle of 4 degrees, the reflectivities of sample No. 1, No. 2, and No. 3 were 37%, 25%, and 10%, respectively. These results show that the multilayer coating consisting of 30 pairs of Mg/SiC with a layer thickness of 15.85 nm and thickness ratio of 0.3 achieved the highest reflectivity at 30.4 nm among all the samples and the reflectivity was two times higher than the conventional coating such as Mo/Si (18.8%). The performance evaluation of the flight mirror for normal incident light is described in detail in the subsection 2.4.5.

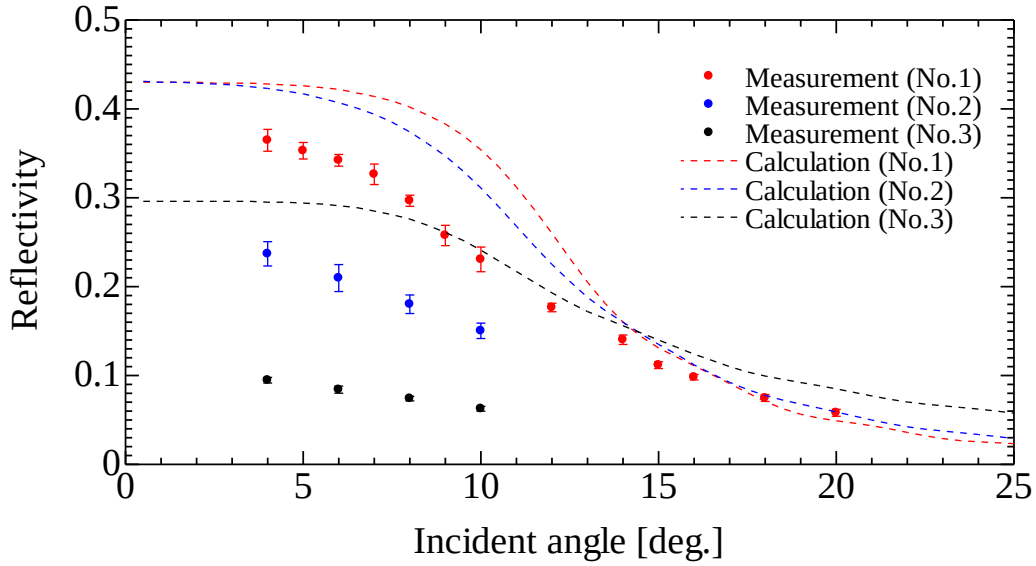

Figure 2.7. Averaged reflectivities at 30.4 nm of Mg/SiC multilayer coated mirrors (No.1-3). The calculated reflectivities are also shown.

Instead of measurements of reflectivities for nearly normal incident light of sample No. 1, I confirmed indirectly the accuracy of manufacturing of mirrors by comparing measured values of the reflectivities and the fitted curve to them. The best parameters of the least-squares fitting are d of 15.66, Γ of 0.32, and N of 30. It is confirmed that the sample mirror was manufactured within 1.5% of tolerance (nominal value of the manufacturer). The result is shown in Figure 2.8.

The calculated values were reflectivity curves when ignoring (1) roughness of a surface and interfaces, (2) diffusion of substances at interfaces that occurs after deposition, and (3) measurement errors of thickness of each layer. The difference of about 1.5% between the calculated value and the measured values of sample No. 1 in Figure 2.8 appears probably due to disregard for the above effects. The error due to individual differences of multilayer coatings has not been evaluated in this study. The reduction in reflectivity of multilayers composed of a combination of Mg and SiC due to the diffusion of substances and the roughness of interfaces was suggested in previous studies [e.g., *Zhu et al.*, 2008]. The dependence of states of interfaces on thickness of

Mg layers was also reported [e.g., *Pelizzo et al.*, 2012]. Although I recognized that improvement of reflectivity by closing d and Γ to the target values through feed-back of results of evaluations to the manufacturer should be done, no implementation was carried out in this study. The degree of decrease in reflectivity depends on the deviation of d from the target value as shown in Figure 2.5. Actually, the reflectivity with larger d than the target value decreases more moderately than that with smaller d. From this result, it can be said that layer thickness should be set thicker than the target value when designing Mg/SiC multilayer coatings so that the expected value becomes large and the dispersion becomes small with consideration for the accuracy of 1.5%.

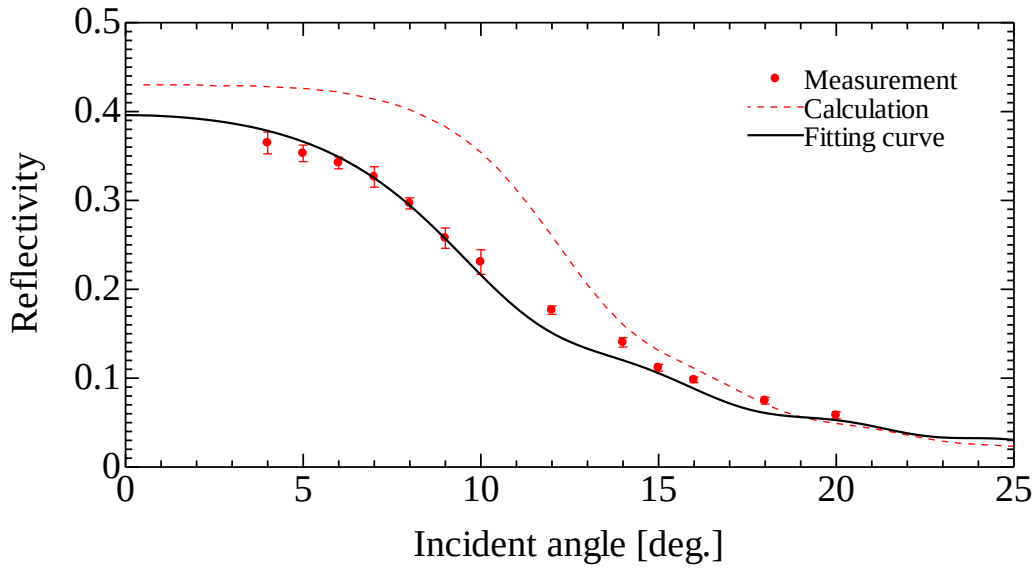

Figure 2.8. Confirmation of the accuracy of manufacturing of mirrors. Red dots show the reflectivities of the sample No.1 and the dashed line shows the calculated reflectivities. The best fitted curve to the measured points with parameters of d of 15.66, Γ of 0.32, and N of 30 is shown in the black line.

2.4.4. Stability Evaluation of the Mg/SiC Multilayer Coated Mirror

The sample mirrors with the Mg/SiC multilayer coatings achieved the high reflectivity at the wavelength of 30.4 nm. However, Mg is known to be highly reactive. In nature, Mg is usually found in the form of a carbonate, an oxide, or a silicate, often in combination with calcium. The issue of long-term stability of Mg based multilayer coating has been remained [e.g., *Soufli et al.*, 2005].

In this work, I have evaluated stabilities of the reflectivities of the Mg/SiC multilayer coated mirrors of sample No.1 with an incident angle of 10 degrees through 4 storage environment. The storage environments are shown in Table 2.7. The samples were under vacuum ($< 10^{-4}$ Pa) in every measurements.

Figure 2.9 shows the results of the experiments about long-term stabilities of the Mg/SiC multilayer coated mirrors. The results show that no dramatic degradation in the reflectivities of each Mg/SiC multilayer coated mirror is found. This result suggests that surface layers of SiC prevent inner Mg layers from the reaction with materials in the air.

Table 2.7. Four storage environments for the evaluation of the stabilities

Plate No.	Storage Environments
(i)	Under Vacuum
(ii)	N_2 Purge
(iii)	Under Atmosphere with Silica Gel (in Clean Bench)
(iv)	Under Atmosphere (in Clean Bench)

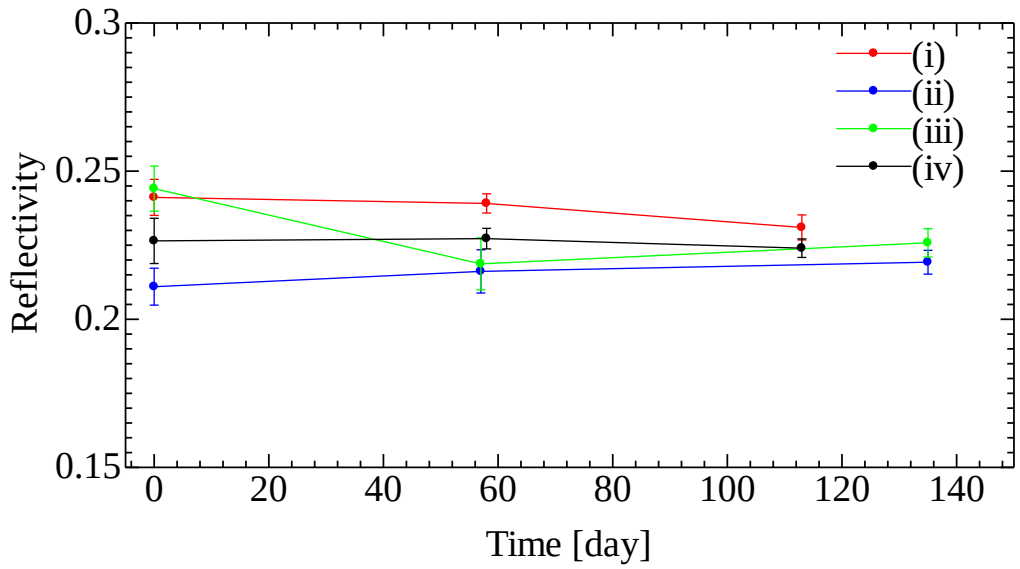

Figure 2.9. Stabilities of the Mg/SiC multilayer coated mirrors. The wavelength of 30.4 nm and the incident angle of 10 degrees were selected at the measurements.

2.4.5. Mg/SiC Multilayer Coated Mirror installed in PHOENIX

The experimental results as described in Section 2.4.3 and 2.4.4 suggested that the Mg/SiC multilayer coating is suitable and can be applied to the optics of PHOENIX onboard EQUULEUS. Therefore, the flight mirror for PHOENIX was fabricated with the combination of Mg/SiC.

Figure 2.10 shows a photograph of the flight mirror for PHOENIX and specifications of the mirror are summarized in Table 2.8. The substrate of the mirror was made of CLEARCERAM-Z and thickness of the center of it is 7 mm. The effective diameter and focal length of the Mg/SiC mirror are 53 mm and 70 mm, respectively. In order to reduce aberration, the surface of the mirror is a spherical shape. The parameters of the multilayer are the same as those of the sample No.1 as described above. The reflectivities of the flight mirror of PHOENIX are shown in Figure 2.11 and optimized

for the He II emission (30.4 nm).

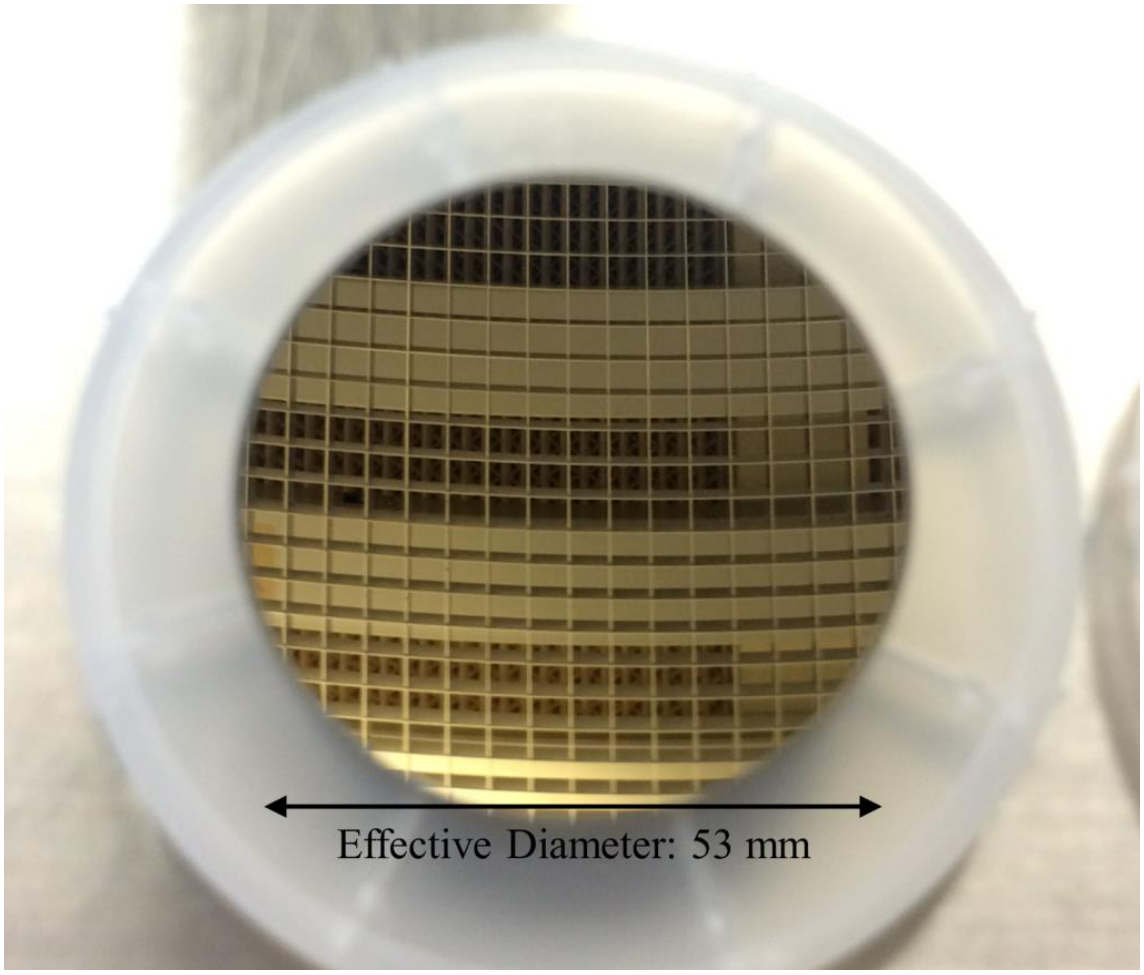

Figure 2.10. Photograph of the flight mirror for PHOENIX. The mirror whose surface is a spherical shape in order to reduce a spherical aberration has the focal length of 70 mm and the effective diameter of 53 mm. The surface is coated by 30 pairs of Mg/SiC multilayer.

Table 2.8. Specifications of the flight mirror of PHOENIX

Substrate	
Material	CLEARCERAM-Z
Diameter	ϕ 55 mm
Curvature	R140 mm
Thickness	7 mm (at the center of the substrate)

Multilayer	
Combination of Materials	Mg/SiC
Number of Periods, N	30
Multilayer Period, d [nm]	15.85
Thickness Ratio, Γ (SiC/d)	0.3

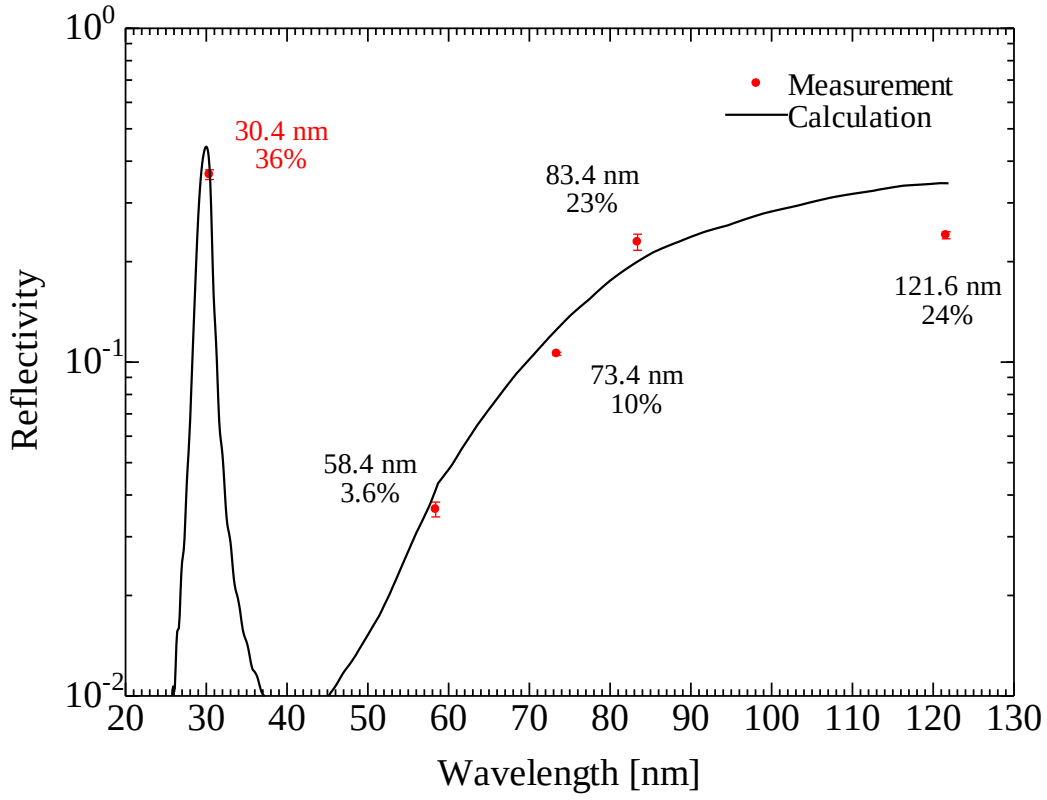

Figure 2.11. Measured reflectivities of the flight mirror installed in PHOENIX. The

calculated reflectivities are also shown. The red dots show the reflectivities for the light incident on a position of 25 mm away from the center of the mirror. The measured values agree well with the calculated values.

Figure 2.11 shows reflectivities when light with a spot diameter of 1mm or less entered at a position 25 mm from the center of the flight mirror. The incident angle to the mirror was about 10 degrees. Calculated values at the incident angle of 10 degrees are also plotted in Figure 2.11. The measured values and calculated values are in good agreement. Therefore, I assumed that the multilayer coating was deposited with high accuracy, and calculated the reflectivities for 30.4 nm of the whole region of the mirror with two different incident angles. Figure 2.12 shows the result of the incident angle distribution on the mirror surface for incident angles of 0 degrees and 6 degrees to PHOENIX. The reflectivity distributions converted from the incident angle distributions are shown in Figure 2.13. I used a reflectivity curve obtained by fitting to measured reflectivities of the sample mirror (Figure 2.8) when determining the distributions. The total reflectivity of the whole mirror surface is about 30% with an incident angle of 0 degrees to PHOENIX, while that with 6 degrees is about 25%.

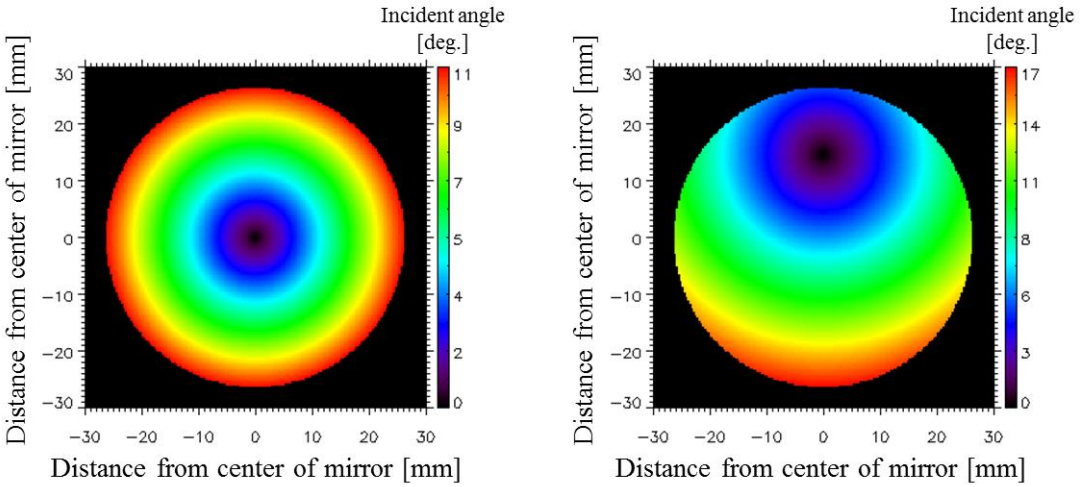

Figure 2.12. Distributions of incident angles to the mirror. The left (right) panel shows the distribution for an incident angle of 0 deg. (6 deg.) to PHOENIX.

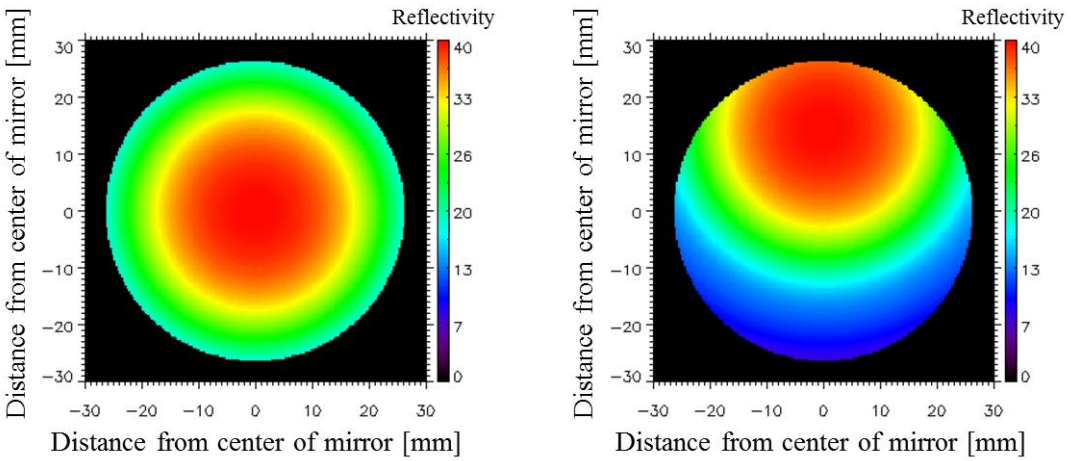

Figure 2.13. Reflectivity distributions on the mirror surface. The left (right) panel shows the distribution for an incident angle of 0 deg. (6 deg.) to PHOENIX.

2.5. Metallic Thin Filter

A metallic thin filter for selection of incoming light is placed at 4.66 mm off from a detector plane. Materials used in the filter need to be chosen to efficiently pass through 30.4 nm, while low sensitivities to other lights which are the possible contamination sources (i.e., geocoronal He I 58.4 nm, O II 83.4 nm, H I 121.6 nm and emissions from the interplanetary medium) are desirable. The transmittance of the filter can be calculated from complex refractive index in the same way as reflectivity of the multilayer coated mirror. A combination of Al and C is conventionally used in the previous plasma imagers [*Nakamura et al.*, 1999, 2000; *Yoshikawa et al.*, 2008, 2010; *Murakami et al.*, 2010].

2.5.1. Design of the Metallic Thin Filter

The flight filter made of a combination of Al and C is equipped with PHOENIX. In order to prevent oxidization of an Al material, carbon coatings of 15 nm are on both sides of an Al film whose thickness is 165.2 nm. Figure 2.14 shows a

photograph of the flight filter for PHOENIX. The specifications of the filter are shown in Table 2.9. This filter can attenuate emissions whose wavelengths are longer than 40 nm. The flight filter was manufactured by LUXEL Corporation.

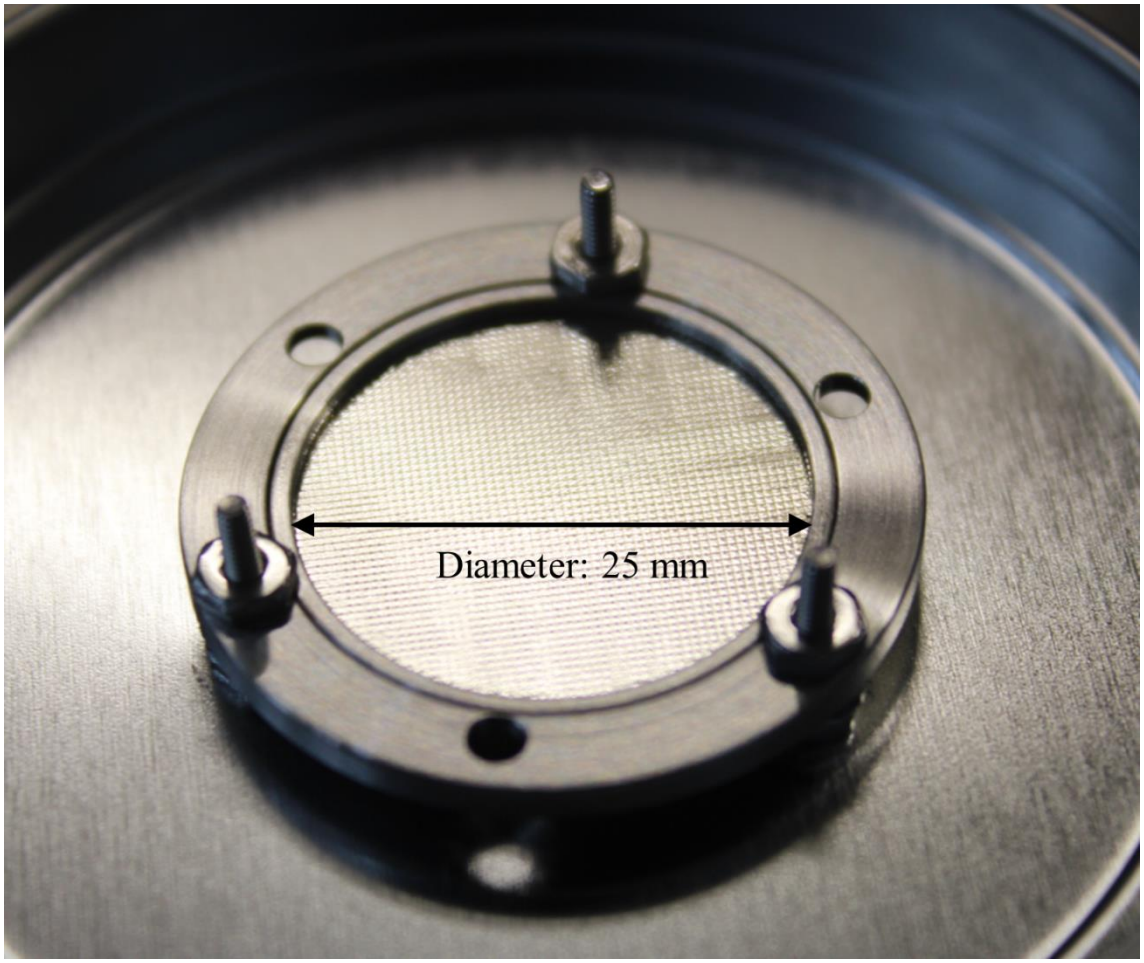

Figure 2.14. Flight filter for PHOENIX. Carbon materials are coated on both sides of an Al film. The thickness of the C/Al/C filter is 15nm/165.2nm/15nm. The filter is supported by a stainless steel mesh having a wire.

Table 2.9. Specifications of the flight filter for PHOENIX

Materials	C/Al/C
Effective Area	ϕ 20.5 mm
Thicknesses	$15nm/165.2nm/15nm$

2.5.2. Transmittance Measurement

Figure 2.15 shows the results from measurement of the transmittance of the flight filter and calculation. The C/Al/C filter has transmittances of 20.1% at 30.4 nm, 2.6% at 58.4 nm and 0.2% at 73.4 nm, and the transmittance above 83.4 nm is less than the MCP noise level of ~0.7 cps/cm^2. The elimination of contamination from longer wavelengths is achieved well enough.

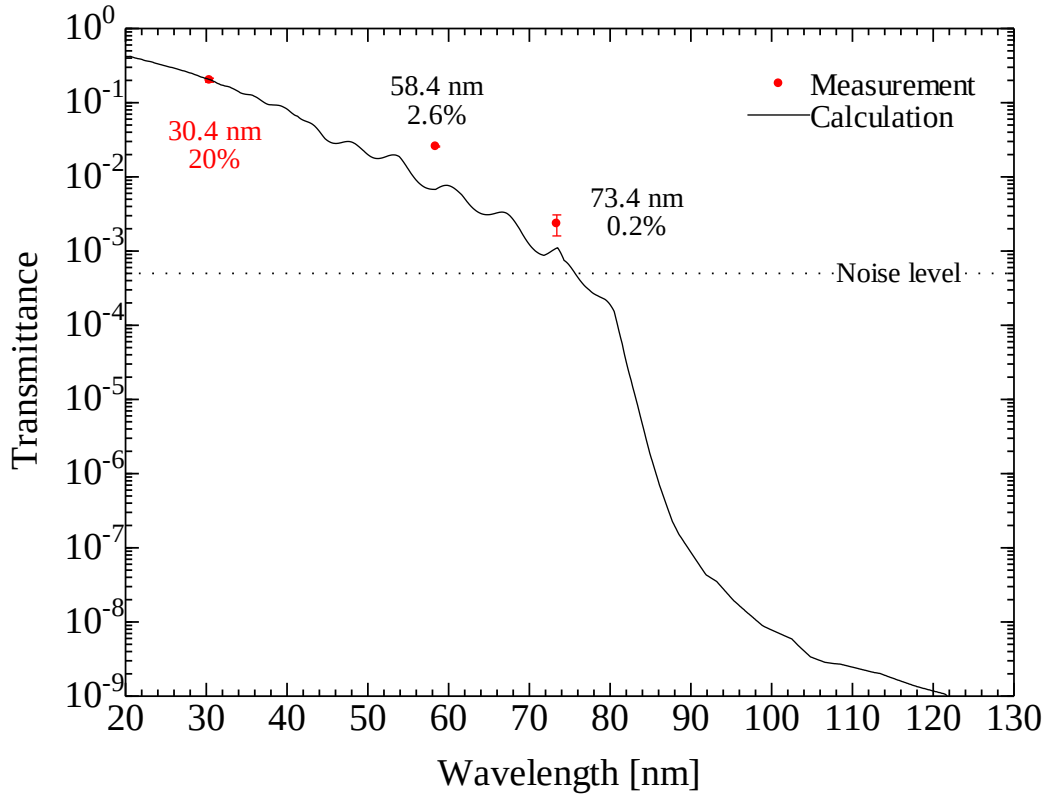

Figure 2.15. Transmittances of the flight filter for PHOENIX at the incident angle of 0 degrees. The transmittances at 83.4 nm and 121.6 nm are less than the noise level (~0.7 cps/cm^2) of the MCP detector. The calculated transmittance is also shown.

2.6. Microchannel Plate and Resistive Anode Encoder

For the PHOENIX detector, microchannel plates (MCPs) and a resistive anode encoder (RAE) which are conventional techniques for EUV imaging are used. In order to achieve cost reduction, I actively adopted the MCPs of a catalog item.

2.6.1. Designs of the Microchannel Plate and Resistive Anode Encoder

A 3-stack MCP detector is placed at the focus of the Mg/SiC multilayer coated mirror. The specifications of the MCP detector are shown in Table 2.10. The detector has an effective area of 14.5 mm with a bias angle of 8 degrees, a 12 μm pore size, and an L/D (a ratio of length to pore diameter) of 40 and total resistance of the MCPs is ~1 MOhm. Behind the MCPs, a resistive anode encoder is placed to analyze positions of incident photons. The conventional RAE has a rectangular shape. However, in order to downsize, the RAE installed in PHOENIX was improved to a triangle shape. This improvement has advantages of a reduction of the number of channels of analog electronics and enlargement of the aperture. A photograph of the flight assembly of MCPs and RAE is shown in Figure 2.16.

Table 2.10. Specifications of the MCP (catalog item)

Number of Stacks	3-stack
Effective Area	ϕ 14.5 mm
Input High Voltage	Nominal value: -2.5 kV
Gain	$> 10^7$

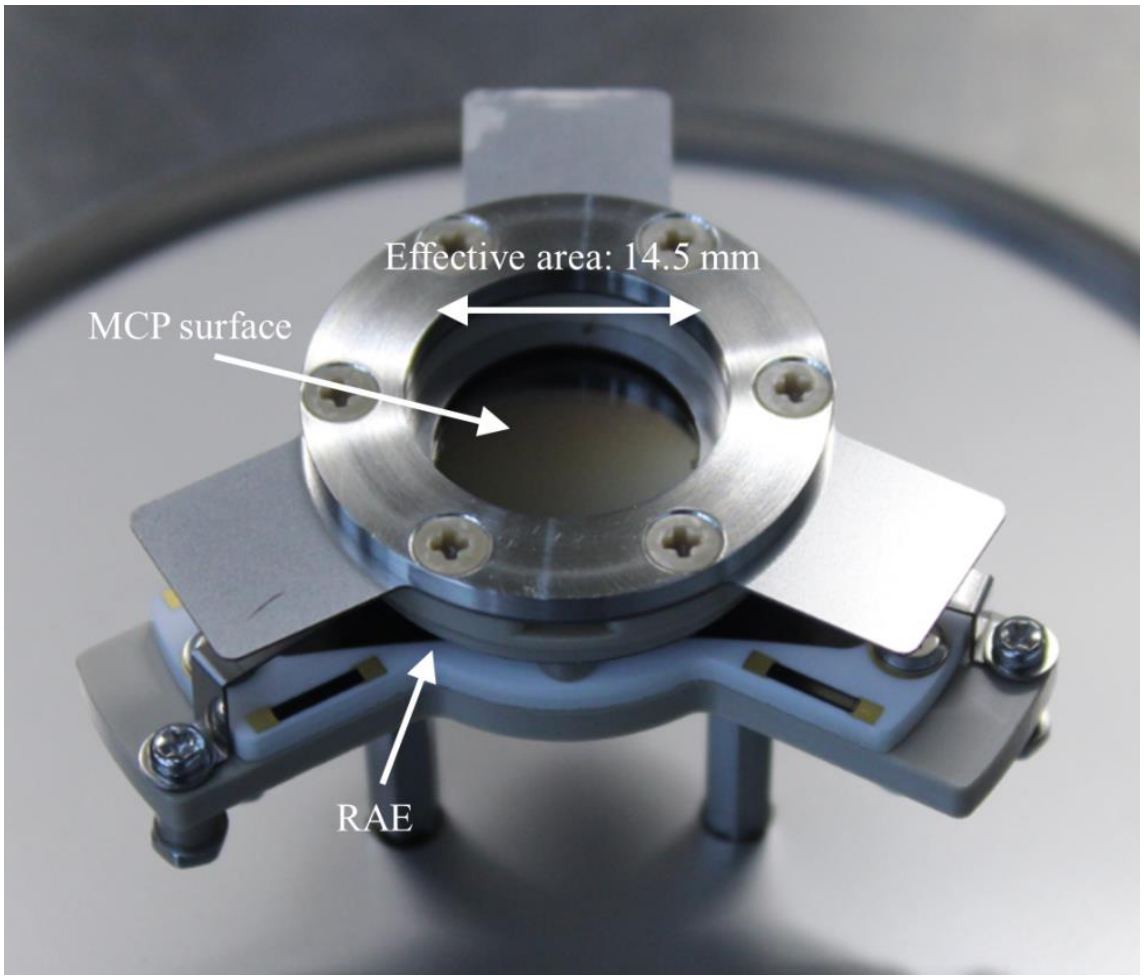

Figure 2.16. Assembly of MCPs and RAE for PHOENIX. The effective area of the MCPs is 14.5 mm diameter. The triangle shaped RAE is placed behind the MCPs.

An electron cloud emitted from the MCPs consists of an order of ~10^7 electrons. The electron cloud is drifted from the MCPs output to the RAE and divided over three electrodes at the corners in reverse proportional to the distance to them. Figure 2.17 shows a block diagram of position analysis in the electronics of PHOENIX. The electrons are directly sent to the charge amplifiers. The amplifiers are composed of three separate electrodes (one for each anode corner). The signal at the electrode is amplified by A-225 and PH300 holds the signal peak. These processes are done in the vicinity of the lens barrel of PHOENIX, while following processes are done at a distance up to 35 cm from the lens barrel due to size limitation of the spacecraft. ADC digitalizes height of the signal. The main electronics (FPGA) computes the position.

The position of an incident photon is calculated by following formulas,

$$X = \frac{Q_A}{(Q_A + Q_B + Q_C)} \tag{2-1}$$

$$Y = \frac{Q_C}{(Q_A + Q_B + Q_C)} \tag{2-2}$$

where, QA, QB, and QC represent the amounts of electrons divided for each electrode. The location of the incident photon is transmitted to an (X, Y) of an oblique coordinate system and the intensity is incremented digitally by 1. The coordinate system divides into 256×256 bin^2. A-225 and PH300 are manufactured by AMPTEK. In nominal observation, PHOENIX will take one image every 10 minutes. The obtained two-dimensional data will be downlinked and integrated to acquire an image of the plasmasphere. In the ground calibration, the dark count rate of the MCP detector was ~0.7 cps/cm^2. The assembly was manufactured by HAMAMATSU Photonics.

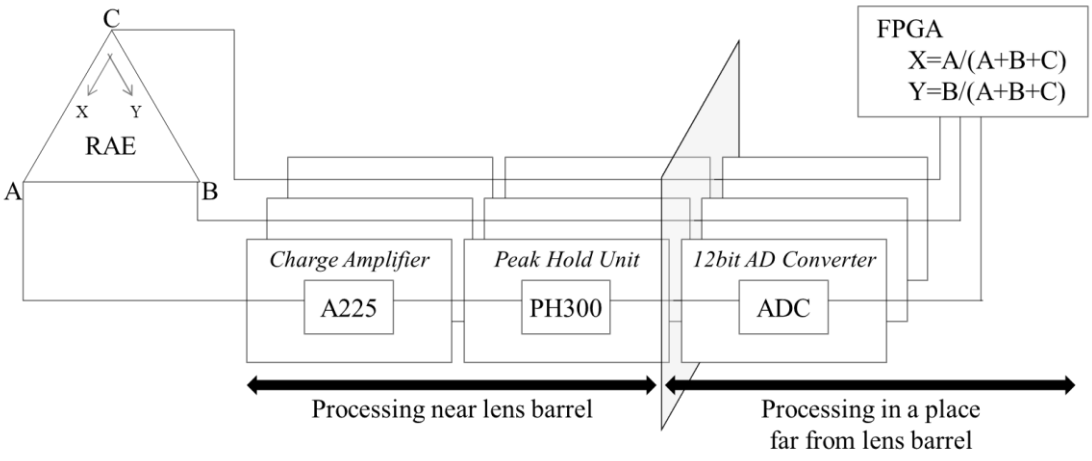

Figure 2.17. Block diagram of position analysis electronics. Preamplifiers and peak-hold ICs are AMPTEK Co. products. This system realizes 256-bin for each axis.

2.6.2. Quantum Efficiency Measurement

In order to evaluate quantum efficiencies of the MCPs installed in PHOENIX, measurement for emission lines with a wide spectral range was performed. The wavelength was selected by a spectrometer, which is installed behind a lamp. Figure 2.18 shows the dependence of the quantum efficiencies (QEs) on an incident angle of 0 degrees. For 30.4 nm, the QE achieved 0.16 and it gradually decreased with increases in the wavelength. The QE for 121.6 nm, which is the strongest emission in circumterrestrial space, was 1/10 compared to that for 30.4 nm.

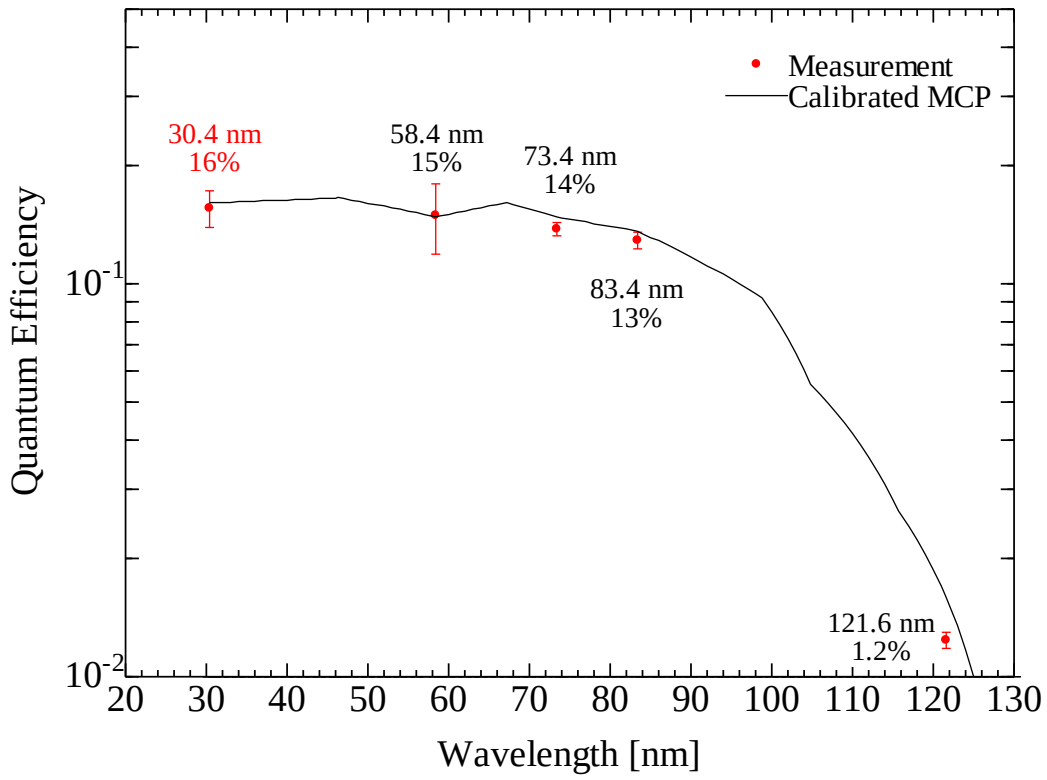

Figure 2.18. Measured QEs of the MCPs for PHOENIX with an incident angle of 0 degrees. As the wavelength becomes longer, the QE decreases and eventually, for 121.6 nm, it decreases to 1/10 compared to that for 30.4 nm.

2.6.3. Dependence of Gain of MCPs on Incident Angle

A 3-stack MCP detector is installed in PHOENIX and phases of the MCPs are changed by 180 degrees for each stage. Pores of the MCPs are tilted by a bias angle of 8 degrees. When light with the bias angle enters the pore of the first stage MCP, the secondary electron emission does not occur and eventually the effect leads gain of the MCP detector to reduce. Therefore, it is necessary to quantitatively estimate the reduction in gain due to various incident angles.

I calculated incident angles of light reflected by the mirror to the pore of the first stage MCP as shown in Figure 2.19. Figure 2.20 shows histograms of these incident angles. The dependence of gain on the incident angle of the pore of the first stage MCP was investigated from 0 degrees to 30 degrees in increments of 5 degrees (Figure 2.21). In this experiment, there were variations in the incident angle since incident light to the MCP detector was not strictly parallel light. However, it is considered that the variations were less than 0.1 degrees with consideration of a diameter of a pinhole on the front of a slit and distance between the spectrometer and the slit. The sum of the histogram and the dependence of gain on the incident angle corresponds to gain of the detector when parallel light enters into PHOENIX. Since the difference between the gain for the parallel light with the incident angles of 0 degrees and 6 degrees is about 1.7%, and the threshold of an amplifier is 5×10^6 electrons, the reduction in gain due to the bias angle is negligible as shown in Figure 2.22. The histograms distribute as shown in Figure 2.20 because the ratio of the mirror diameter to the focal length is greater than that of the pore diameter to length. Therefore, gain is insensitive to the incident angle and sufficient amplification is expected even in the first stage MCP.

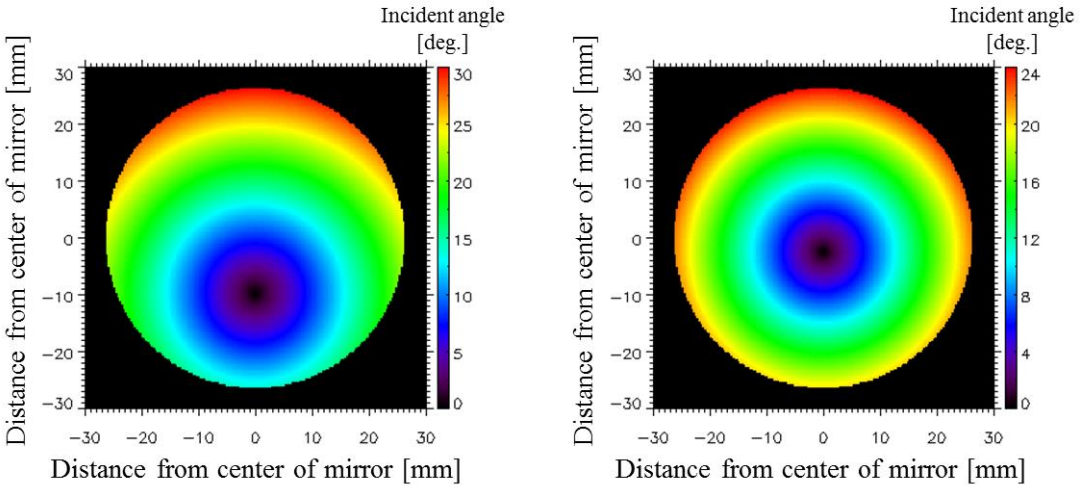

Figure 2.19. Distributions of the incident angle to the pore of the first stage MCP. The left (right) panel shows the distribution at an incident angle of 0 deg. (6 deg.) to PHOENIX.

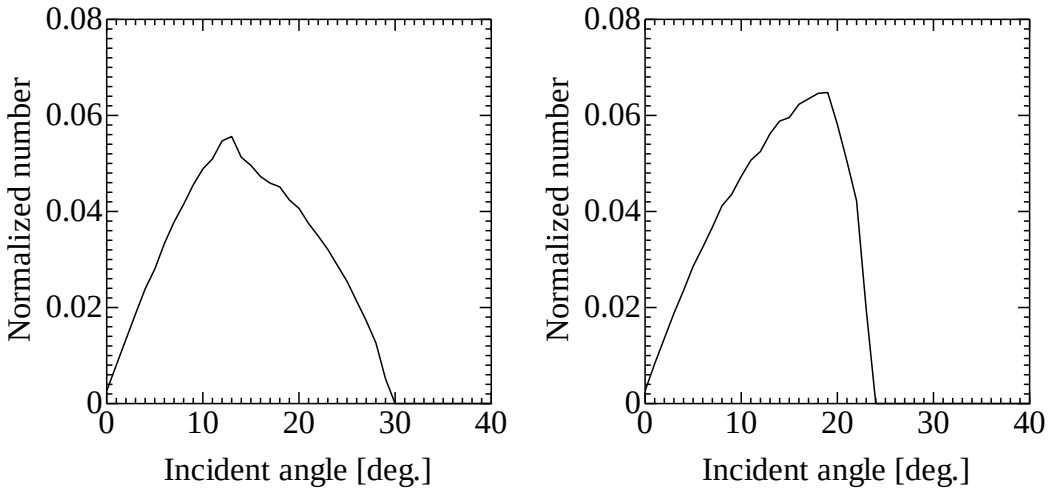

Figure 2.20. Histograms of incident angle to the pore. The left (right) panel shows the distribution at an incident angle of 0 deg. (6 deg.) to PHOENIX.

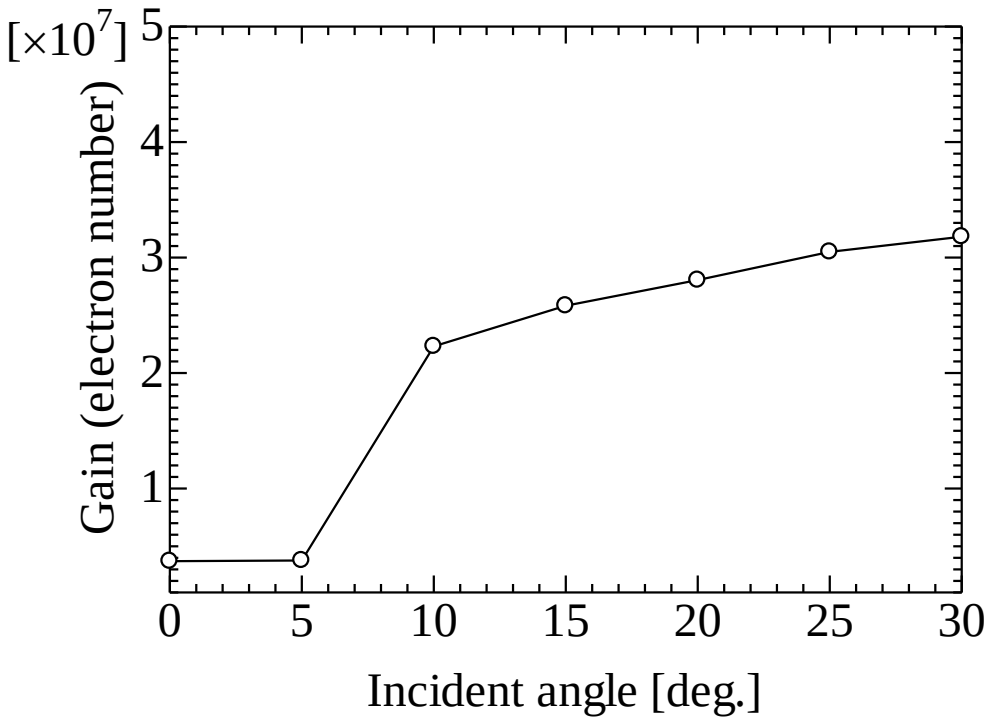

Figure 2.21. Dependence of gain on the incident angle to the pore of the first stage MCP.

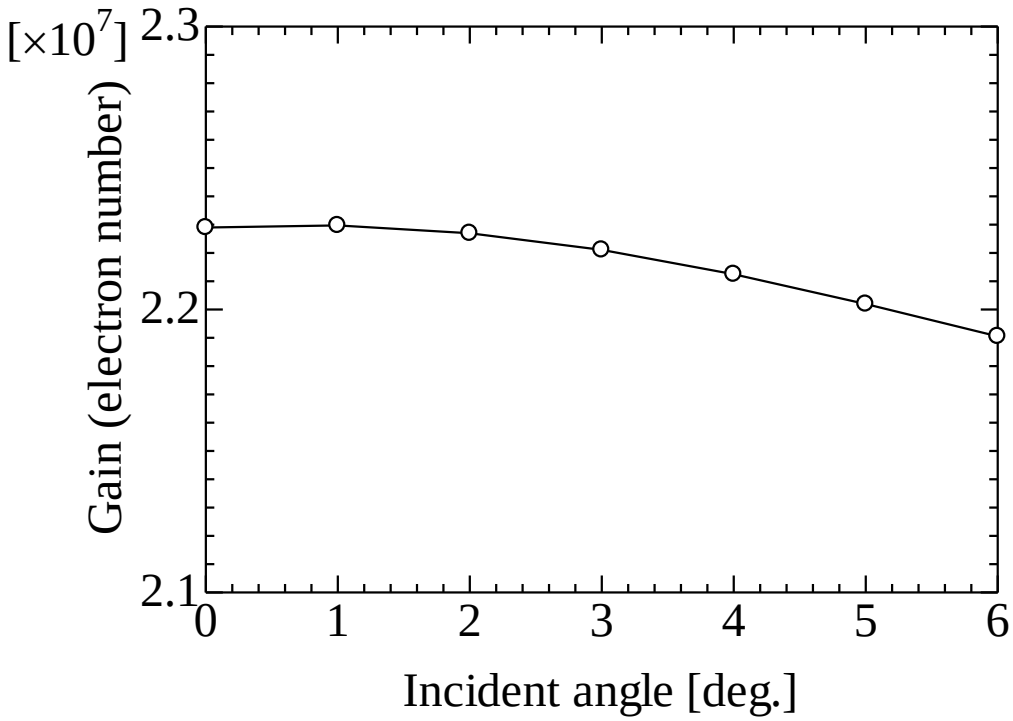

Figure 2.22. Dependence of gain on the incident angle to PHOENIX.

2.7. Aberration Analysis

The target level of a plate scale of PHOENIX is 0.15 Re/bin in design. This value corresponds to 1/2 of the apparent width of the plasmaspheric filament [*Murakami et al.*, 2013] and about 180 μm on the detector plane. Therefore, in order to observe the plasmaspheric structure from the Moon orbit, the spatial resolution of at least 0.15 Re is required. The aberration analysis of an optical configuration of PHOENIX should be performed because a spherical aberration of the mirror possibly blurs acquired images.

Figure 2.23 shows the relationship between the mirror-detector distance and a size of the aberration on the detector plane calculated by Zemax software. The size of the aberration means the 50% encircled energy region (ECE) in this case. The figure explains that, in order to suppress the aberration radius to less than 100 μm, the

distance between the multilayer coated mirror and the detector plane should be in the range of 69.4 ± 0.1 mm. From this analysis, the multilayer coated mirror (focal length = 70 mm) installed in PHOENIX was placed at a distance of 69.4 mm from the detector plane in design.

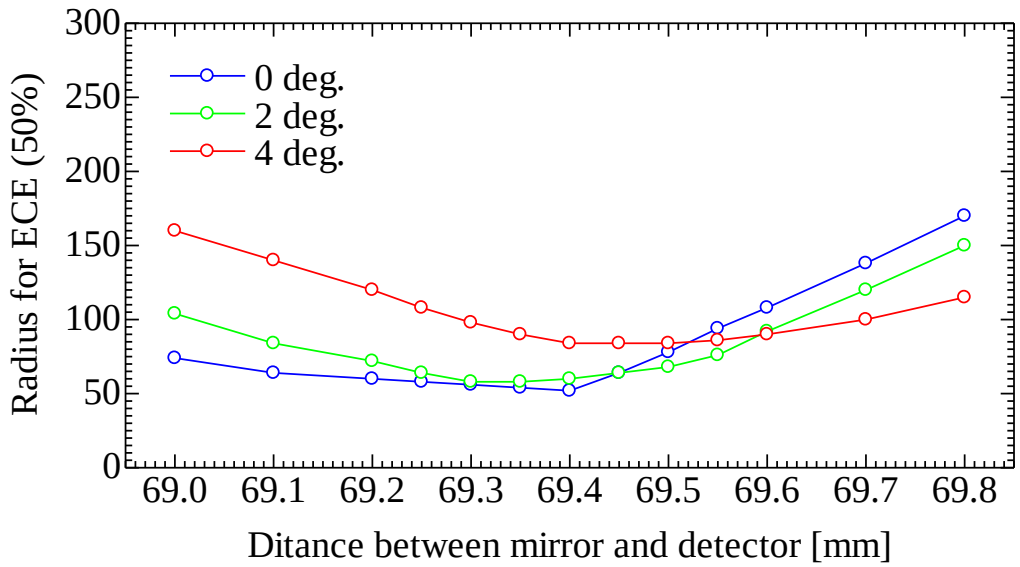

Figure 2.23. Relationship between mirror-detector distance and the size of aberration. The aberration radius of the optical system of PHOENIX can be suppressed to less than $100\,\mu m$ by placing of the mirror at a distance of 69.4 ± 0.1 mm from the detector plane.

The actual distance between the mirror and the detector is fine-adjusted by inserting shims behind the mirror. In order to determine the optimum value of the distance, a collimated light was entered into PHOENIX with various numbers of the shims (thickness of a shim = 0.1 mm) and aberration was evaluated from the spot sizes of collected light on the detector plane. Figure 2.24 shows the result of the experiment with an incident angle of 0 degrees. The result explains that aberration with the designed value (69.4 mm) is smaller than those with other values and the spot size of 88 μm is significantly smaller than the bin size of 180 μm. In other words, the spatial resolution of 0.15 Re can be achieved sufficiently under the influence of the spherical

aberration.

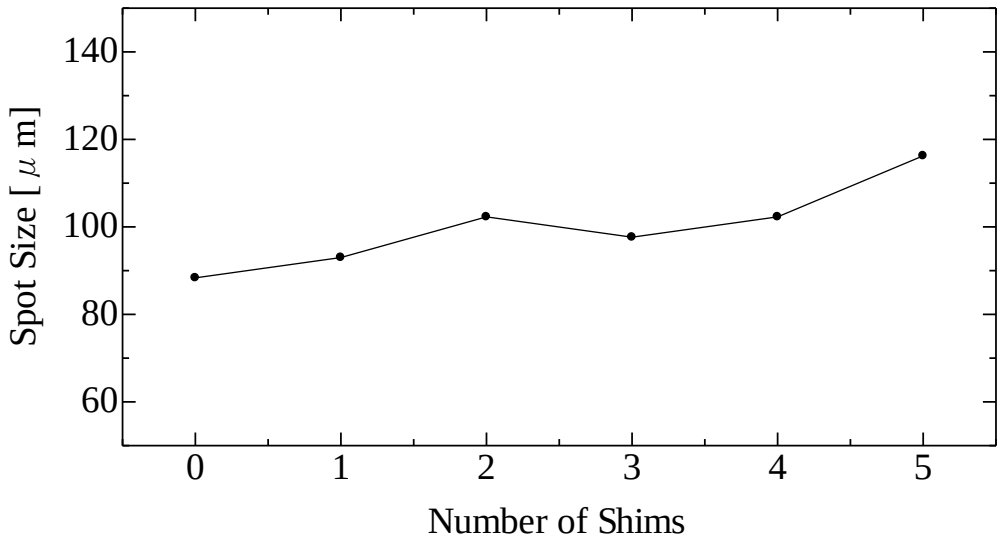

Figure 2.24. Relationship between the number of shims and the spot size which is collected on the detector plane.

2.8. Total Sensitivity of PHOENIX

PHOENIX has a full circular field-of-view of 11.9 degrees, and the spatial resolution of 0.15 Re on the Earth's surface from the Moon orbit.

According to the results of evaluations for each component (a multilayer coated mirror, a metallic thin filter, and an MCP detector), the overall sensitivity of PHOENIX as a function of the wavelength can be estimated. The efficiencies of each component that have been evaluated in the former subsections and the total photon detection efficiency (multiplied all efficiencies) are shown in Figure 2.25.

The signal count rate N (cps/bin) of the emission is represented by the following equation.

$$N = \frac{10^6}{4\pi} \times B \times Eff. \times \Omega \tag{2-3}$$

In this equation, the B represents brightness of the target in units of Rayleigh, and $Eff.$ represents the effective area of PHOENIX which is calculated by multiplying an area of the aperture and the detection efficiency. Ω is the solid angle of identical field-of-view of one bin. The typical values of those parameters are summarized in Table 2.1. PHOENIX has a total sensitivity of 0.059 cps/Rayleigh/bin for the He II 30.4 nm. The efficiencies of each component and the total sensitivity are shown in Table 2.11.

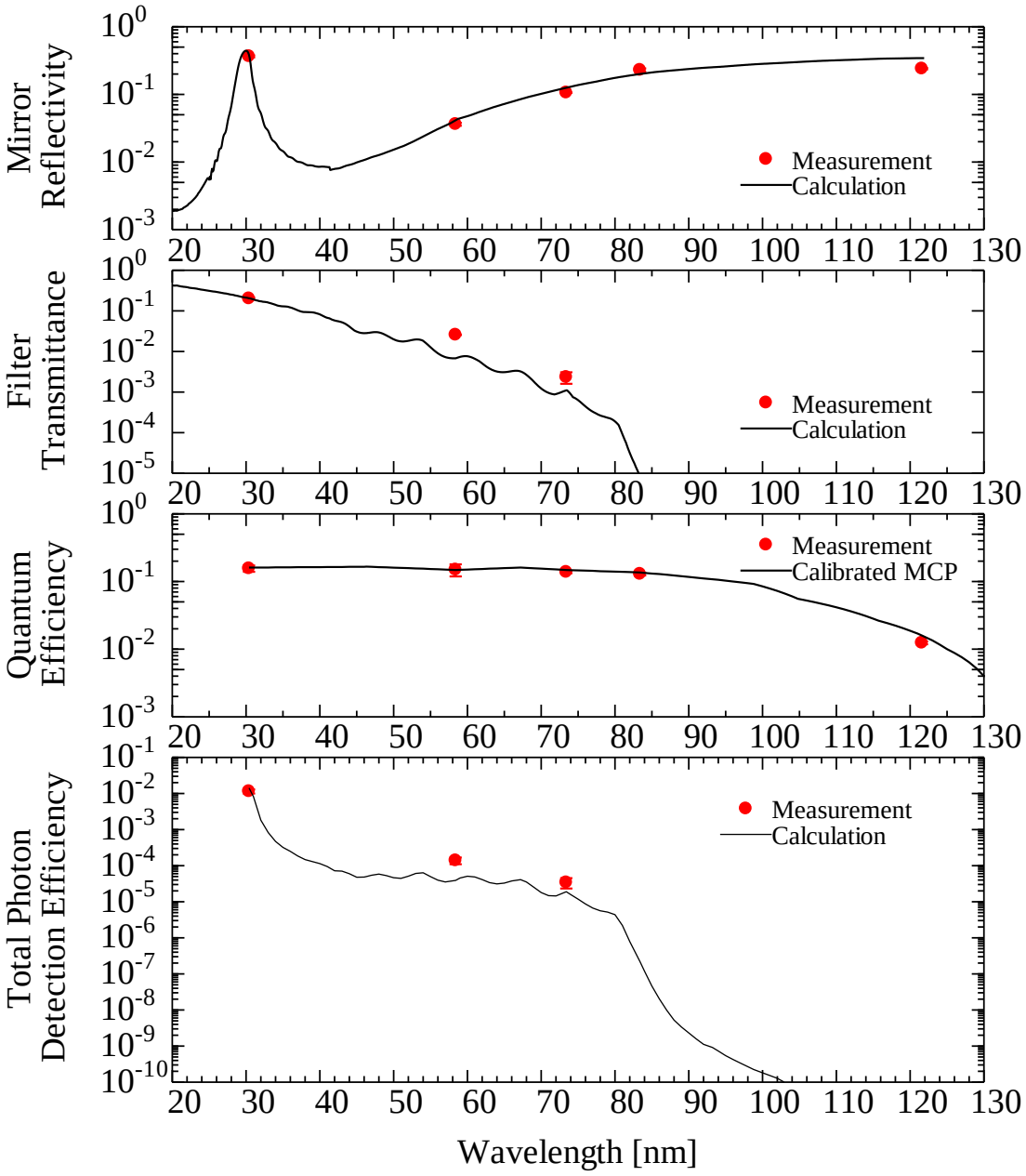

Figure 2.25. Efficiencies of each component and total photon detection efficiency (multiplied all efficiencies) of PHOENIX. The red dots correspond to the measured values and the black lines represent the calculated values. The red dots of the upper panel show the reflectivities of light incident on a position of 25 mm away from the center of the mirror.

Table 2.11. Efficiencies for He II emission (30.4 nm)

Reflectivity of Mirror	30.0%
Transmittance of Filter	20.1%
Quantum Efficiency of MCP	15.6%
Total Sensitivity	0.059 cps/Rayleigh/bin

I estimated the ratios between the signal counts and the statistical fluctuation (signal to noise ratio, SNR). The detector is assumed to be an ideal photon counter and photon counts in each exposure time accord to the Poisson distribution. The statistical fluctuation of signal is described as the square root of counts.

A primary noise source is an instrumental background (noise count from MCPs due to cosmic ray and/or high-energy particle bombardments in the magnetosphere). The second noise source is a contamination from He I (58.4 nm) and H I Lyman-alpha (121.6 nm) emissions. As shown in Figure 2.15, the metallic thin filter attenuates the H I Lyman-alpha emission sufficiently and so the intensity of the emission is negligible for the observation. For He I (58.4 nm), it is fairly well reduced by the filter, however, it has the potential to contaminate the observation. The results from the NOZOMI mission, the intensities of He II 30.4 nm emission from the main body of the plasmasphere and the plasmapause were reported as about 5 Rayleigh by *Nakamura et al.* [2000] and 0.5 Rayleigh by *Yoshikawa et al.* [2000a], respectively. For contamination sources, the maximum intensities of He I (58.4 nm) in the geocorona and the interplanetary are assumed to be 100 Rayleigh [*Meier and Weller*, 1972] and 7.5 Rayleigh [*Yamazaki et al.*, 2006], respectively. It should be noted that the main body of the plasmasphere imaged by PHOENIX cannot be distinguished clearly from the contamination of the geocoronal He I emission. On the other hand, the interplanetary He I emission can be observed separately in the field-of-view of PHOENIX. Therefore, the interplanetary He I emission can be subtracted from the obtained image. Because it was reported that the temporal variation and spatial distribution of the emission are very small [*Yamazaki et al.*, 2006], the statistical fluctuation of the background can be assumed as the square root of counts of the background.

SNR can be assumed based on the following equations,

$$
\begin{aligned}
N_{signal} &= N_{total} - N_{background} \\
\sigma_{signal} &= \sqrt{\sigma_{total}^2 + \sigma_{background}^2} \approx \sqrt{\sigma_{signal}^2 + 2\sigma_{background}^2} \approx \sqrt{N_{signal} + 2N_{background}} \\
SNR &= \frac{N_{signal}}{\sigma_{signal}} = \frac{N_{signal}}{\sqrt{N_{signal} + 2N_{background}}}
\end{aligned}
\tag{2-4}
$$

where N_{signal} is the EUV signal detected by the detector in units of cps/bin. $N_{background}$ is expressed in the instrumental background plus the contaminations from the interplanetary He I emission (58.4 nm). The calculated SNRs are shown in Figure 2.26. PHOENIX can observe the plasmapshere with 10-min exposure time in nominal observation and identify the main body of the plasmasphere with a high SNR (>10). The plasmapause can be observed with the exposure time of < 1hour.

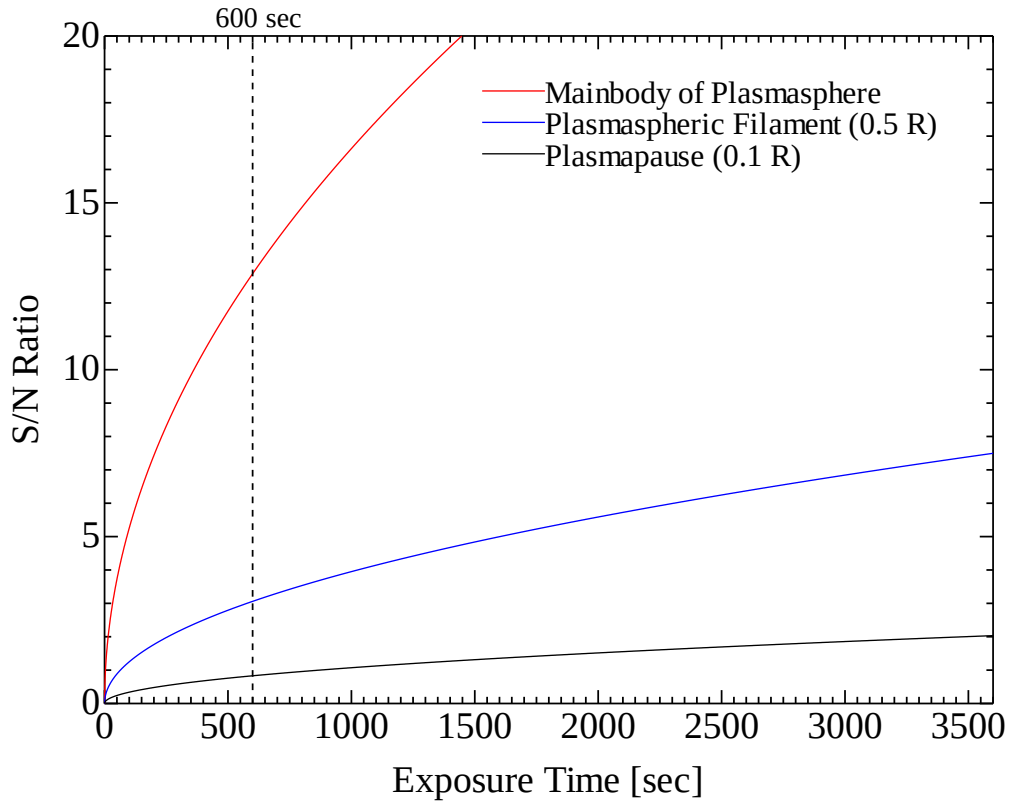

Figure 2.26. Signal-to-noise ratios of the observations for the plasmaspheric structure.

2.9. Feasibility Analysis for Observation of PHOENIX

The plasmapause and the plasmaspheric filament are assumed as the observation targets of PHOENIX.

For observations for the plasmapause, the aim is to capture structural changes of it to the geomagnetic variations. The geomagnetic storm, a large scale geomagnetic disturbance, causes a decrease in the geomagnetism over several hours in the main phase. In the recovery phase, the geomagnetism increases over several hours to days and finally returns to the steady state. In order to capture these geomagnetic variations, the temporal resolution of 1 hour is thought to be sufficient. In the case of the plasmaspheric filament, its structure can be observed with 10-min exposure as shown in

Figure 2.26. The structure moves about 2.5 degrees in the longitudinal direction in 10 minutes because the plasmasphere co-rotates with Earth. When the structure moves 2.5 degrees near the plasmapause (4 Re), the moving distance is less than 0.01 Re as viewed from the Moon orbit. The variation is less than 5% with respect to the width in the longitudinal direction of the filament structure. *Singh and Horwitz* [1992] measured plasma density during refilling after the geomagnetic storm of September 13, 1968. Equatorial density around L of 3.5 recovered to the steady state over about 8 days from the beginning of this refilling event. Furthermore, the refilling rate during erosion was also estimated by *Denton and Borovsky* [2014]. In their simulations, the total ion density increased with a refilling rate of ~120 cm^{-3} / 5 days. Assuming that the refilling rate of He ions is 0.1 cm^{-3} / 1 hour because of their abundance, the increase by refilling of the plasmaspheric density around L of 3.5 is only about 0.1%. Therefore, 10-min exposure is sufficient to capture the structure of plasmaspheric filament and its temporal evolution.

In the main phase of the geomagnetic storm, an erosion of the plasmasphere occurs due to the development of the convection electric field of the magnetosphere. In the recovery phase, the plasmasphere reduced by the erosion returns to the steady state by the refilling of plasma from the ionosphere. During the erosion, the plasmasphere shrank with the mean speed of ~0.2 Re / hour [*Murakami et al.*, 2010]. The structure of the plasmaspheric filament was reported by *Murakami et al.* [2013] and it expands spatially ~0.3 Re. The observations for the above structure require the spatial resolution of 0.15 Re at least and this resolution of PHOENIX was decided based on the trade-off with the downlink rate of the spacecraft.

I simulated the imaging observations for the plasmasphere. The spacecraft with PHOENIX will arrive at the Earth-Moon Lagrange point L2 in June 2019. Figure 2.27 shows the illustration of geometry of observations from the Moon orbit. Figure 2.28-30 show the calculated images with 1-hour exposure obtained by PHOENIX when it is located on the dawn (a), day (b), and dusk (c) sides of Earth. The appearance of the plasmasphere varies depending on the location due to the inclination of the magnetic axis. In these calculations, I assumed that the plasmasphere has a circular shape. The

equatorial He ion density distributions were calculated with an empirical formula obtained from the statistical in-situ measurement [*Carpenter and Anderson*, 1992]. The formula is described as follows:

$$log_{10}N_{eq} = -0.3145L + 3.9043 \quad (2\text{-}5)$$

where N_{eq} is expressed in electron/cc and L is *L*-value. The He ion density along the magnetic field line was calculated from radial power law according to:

$$n = n_0(L\,Re/R)^3 \quad (2\text{-}6)$$

where n_0 is the He ion density at the equatorial plane, *Re* is the Earth radius, and *R* is the geocentric distance [e.g., *Obana et al.*, 2010]. The validity of this model can also be discussed by results from observation of PHOENIX.

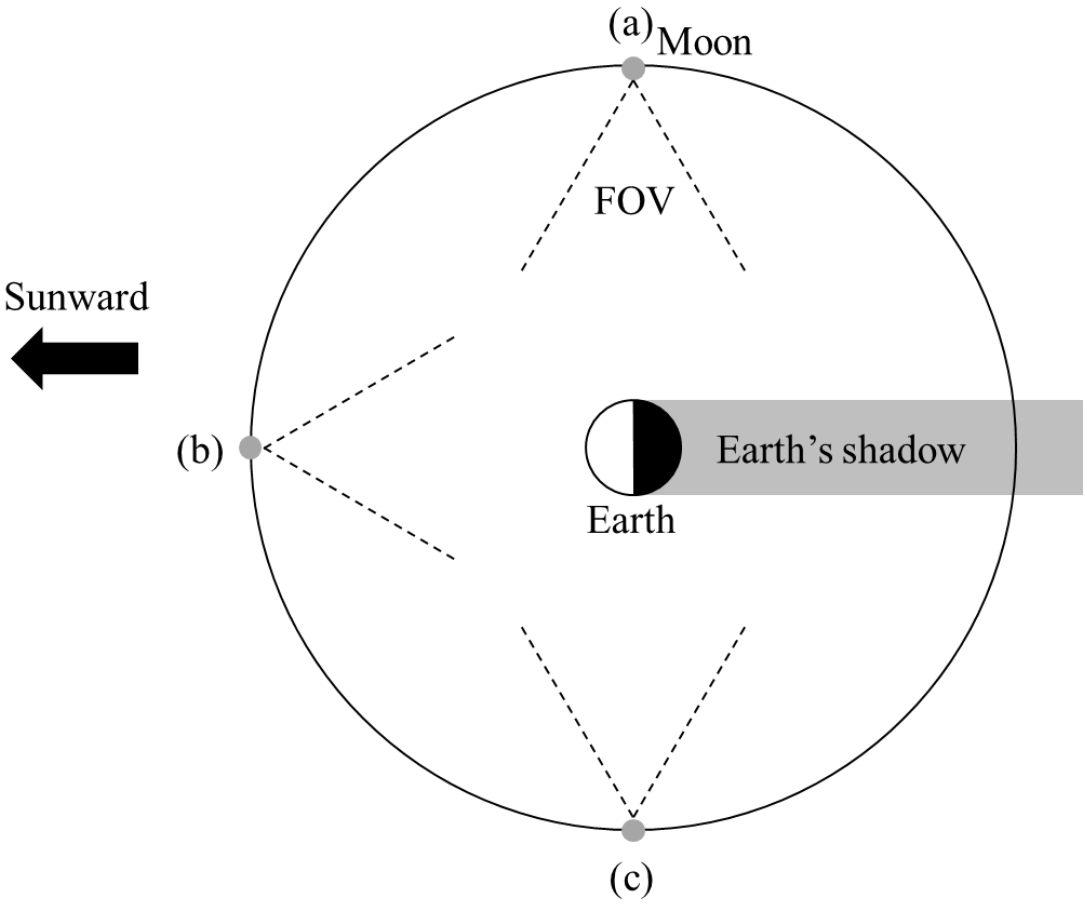

Figure 2.27 Illustration of geometry of observations for the plasmasphere from the Moon orbit.

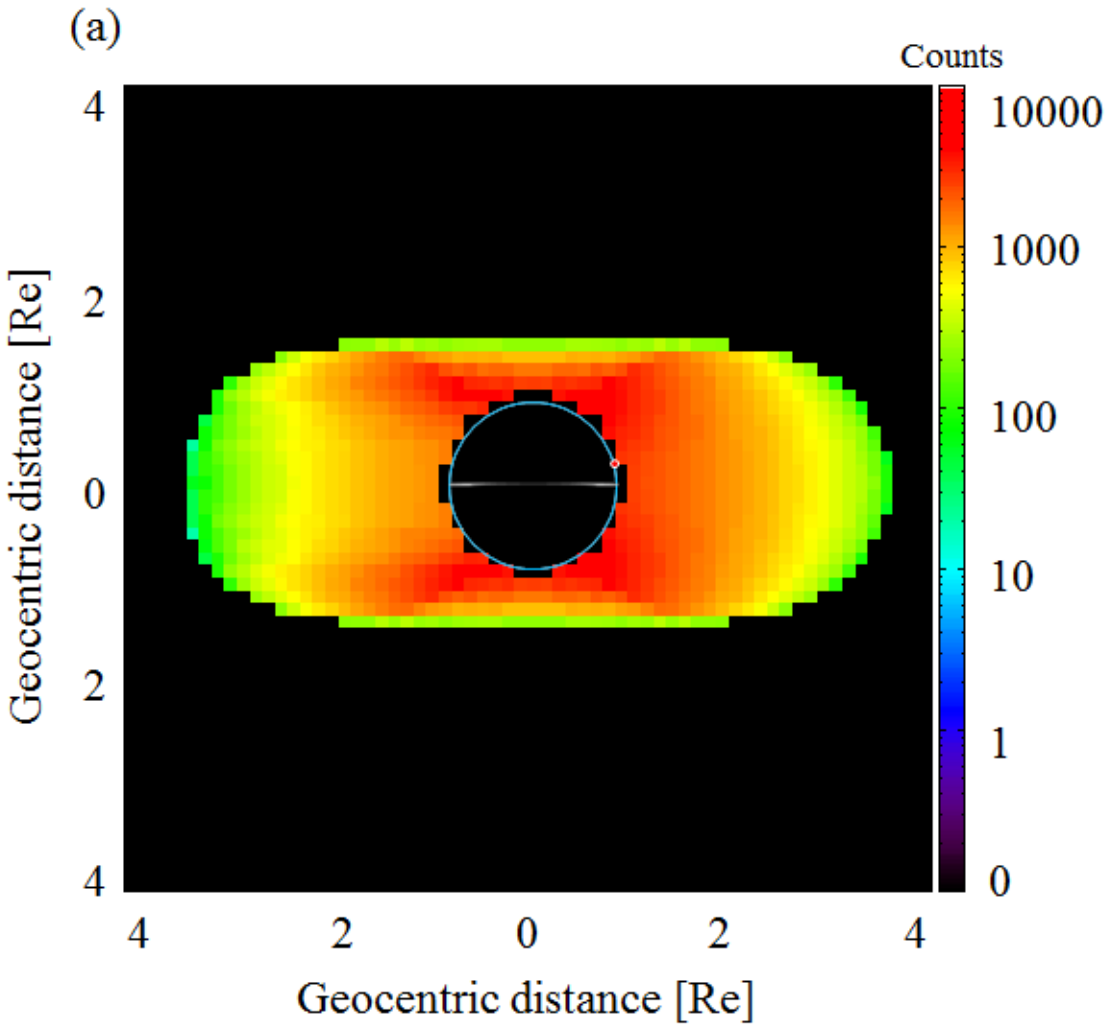

Figure 2.28. Calculated image of the plasmasphere observed by PHOENIX from the location at (a) in Figure 2.27. Earth is located in the blue circle near the center of the image. The white line and the red dot on Earth represent the Earth's geomagnetic equator and the sub-solar point, respectively. The sun is on the right side of the image.

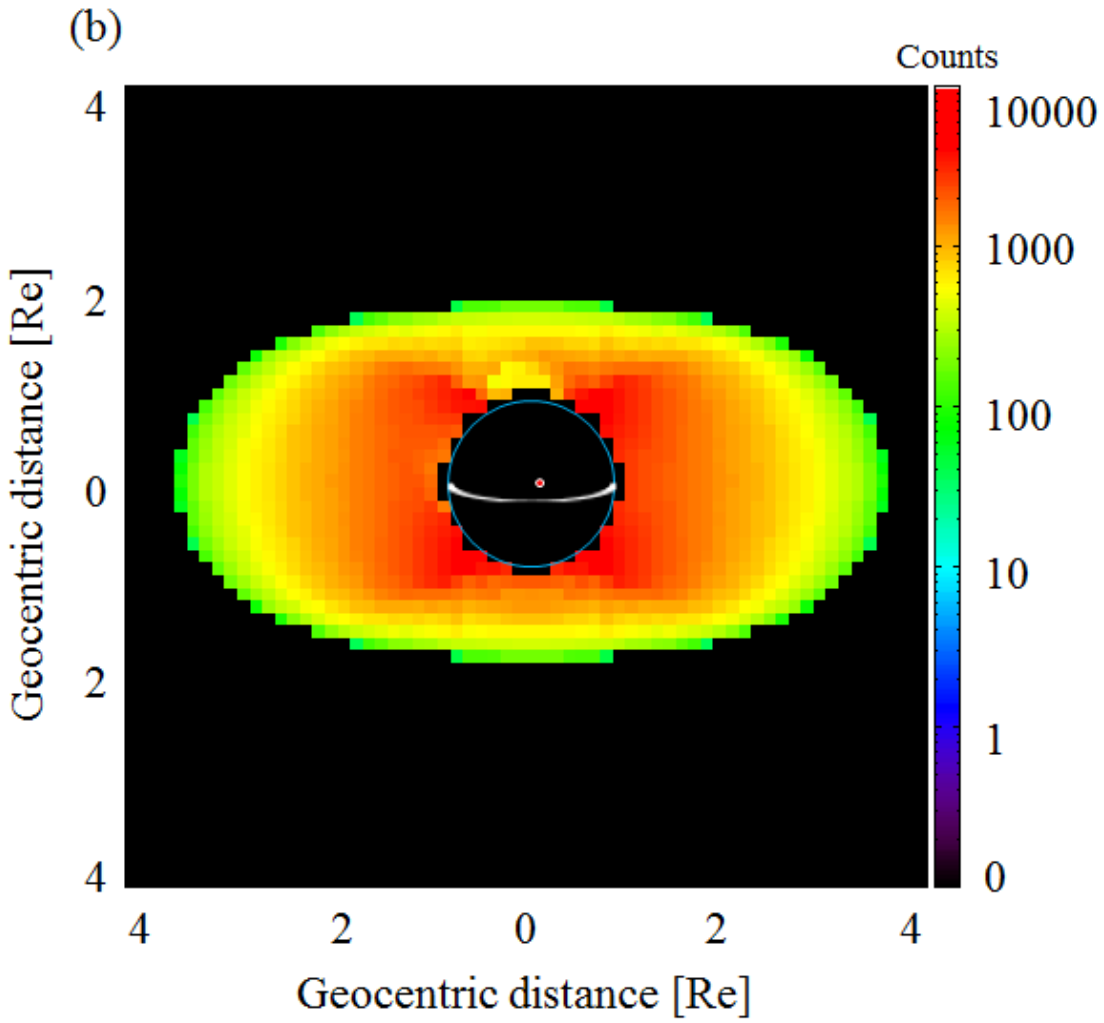

Figure 2.29. Calculated image of the plasmasphere observed by PHOENIX from the location at (b) in Figure 2.27. This image is presented in the same manner as that in Figure 2.28.

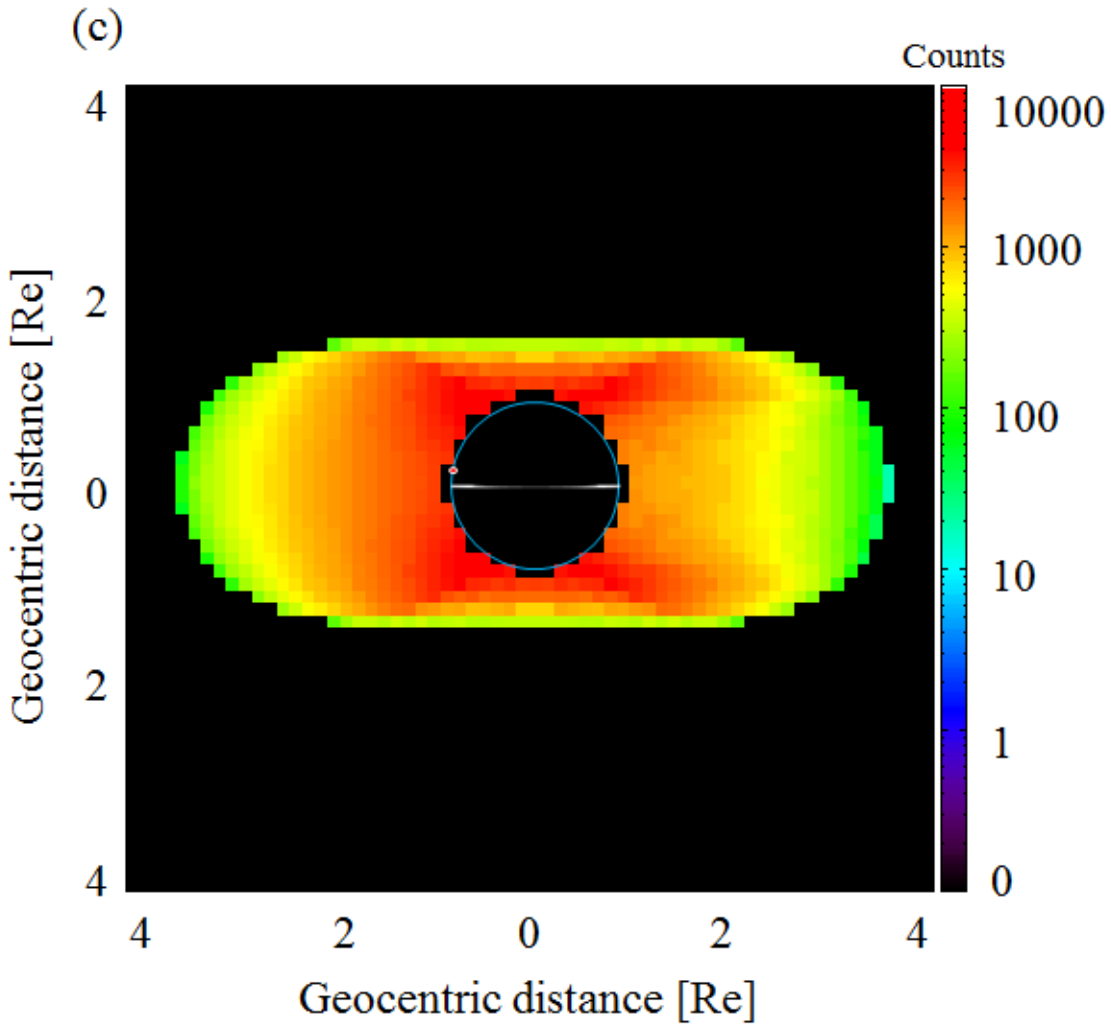

Figure 2.30. Calculated image of the plasmasphere observed by PHOENIX from the location at (c) in Figure 2.27. This image is presented in the same manner as that in Figure 2.28.

In addition to the imaging of the plasmasphere, observation of the plasmaspheric filament was also simulated. It was reported that this looped structure is filled with 5 times dense plasma as compared with the neighbor magnetic flux tube. Figure 2.31 shows the simulated image with 10-min exposure of the plasmaspheric filament observed by PHOENIX. It is suggested that the filament structure with a width of 0.3 Re can be observed by PHOENIX.

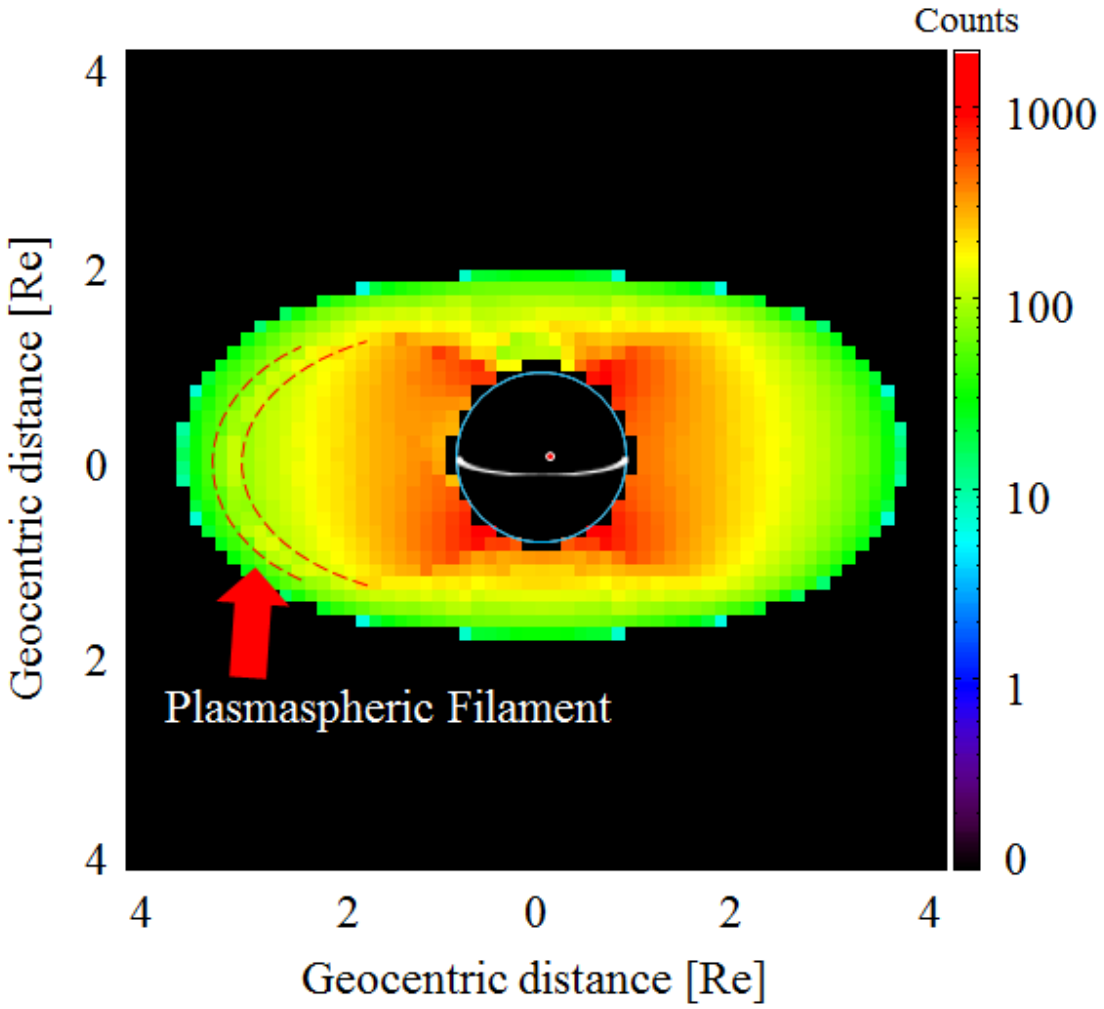

Figure 2.31. Calculated image of the plasmaspheric filament observed by PHOENIX from the location at (b) in Figure 2.27. The isolated flux tube at $L = 3.5$ and MLT = 6 can be detected. Inside it He ion density is assumed to be higher than its neighbors by a factor of 5. The red dashed lines are drawn to emphasize the loop structure.

2.10. Conclusions

The ultra-small EUV imager, PHOENIX, onboard the EQUULEUS will image near-Earth cold plasma at the wavelength of He II (30.4 nm) emission. PHOENIX has enough performance to detect the He ion density distribution in the plasmasphere and can detect the plasmapause with exposure time of < 1 hour. This value is sufficient to discuss the behavior of plasma in the plasmasphere. In addition, the improvement of the

efficiency enabled constructing PHOENIX with size of $66 \times 99 \times 99\, mm^2$, and its size is considerably smaller (< 10%) than KAGUYA/TEX.

References

Banks, P. M., Nagy, A. F., and Axford, W. I. (1971). Dynamical behavior of thermal protons in the mid-latitude ionosphere and magnetosphere. *Planetary and Space Science*, *19*(9), 1053-1067.

Binsack, J. H. (1967). Plasmapause observations with the MIT experiment on IMP 2. *Journal of Geophysical Research*, *72*(21), 5231-5237.

Carpenter, D. L. (1963). Whistler evidence of a 'knee'in the magnetospheric ionization density profile. *Journal of Geophysical Research*, *68*(6), 1675-1682.

Carpenter, D. L. (1966). Whistler studies of the plasmapause in the magnetosphere: 1. Temporal variations in the position of the knee and some evidence on plasma motions near the knee. *Journal of Geophysical Research*, *71*(3), 693-709.

Carpenter, D. L., and Anderson, R. R. (1992). An ISEE/whistler model of equatorial electron density in the magnetosphere. *Journal of Geophysical Research: Space Physics*, *97*(A2), 1097-1108.

Chappell, C. R., Harris, K. K., and Sharp, G. W. (1971). The dayside of the plasmasphere. *Journal of Geophysical Research*, *76*(31), 7632-7647.

Chen, A. J., and Wolf, R. A. (1972). Effects on the plasmasphere of a time-varying convection electric field. *Planetary and Space Science*, *20*(4), 483-509.

Comfort, R. H., and Horwitz, J. L. (1981). Low energy ion pitch angle distributions observed on the dayside at geosynchronous altitudes. *Journal of Geophysical Research: Space Physics*, *86*(A3), 1621-1627.

Decreau, P. M. E., Carpenter, D., Chappell, C. R., Comfort, R. H., Green, J., Olsen, R. C., and Waite, J. H. (1986). Latitudinal plasma distribution in the dusk plasmaspheric bulge: Refilling phase and quasi‐equilibrium state. *Journal of Geophysical Research: Space Physics*, *91*(A6), 6929-6943.

Denton, M. H., and Borovsky, J. E. (2014). Observations and modeling of magnetic flux tube refilling of the plasmasphere at geosynchronous orbit. *Journal of Geophysical Research: Space Physics*, *119*(11), 9246-9255.

Ejima, T., Yamazaki, A., Banse, T., Saito, K., Kondo, Y., Ichimaru, S., and Takenaka, H. (2005). Aging and thermal stability of Mg/SiC and Mg/Y 2 O 3 reflection multilayers in the 25–35 nm region. *Applied optics*, *44*(26), 5446-5453.

Farrugia, C. J., Young, D. T., Geiss, J., and Balsiger, H. (1989). The composition, temperature, and density structure of cold ions in the quiet terrestrial plasmasphere: GEOS 1 results. *Journal of Geophysical Research: Space Physics*, *94*(A9), 11865-11891.

Fernández-Perea, M., Soufli, R., Robinson, J. C., De Marcos, L. R., Méndez, J. A., Larruquert, J. I., and Gullikson, E. M. (2012). Triple-wavelength, narrowband Mg/SiC multilayers with corrosion barriers and high peak reflectance in the 25-80 nm wavelength region. *Optics express*, *20*(21), 24018-24029.

Gallagher, D. L., Craven, P. D., and Comfort, R. H. (1988). An empirical model of the Earth's plasmasphere. *Advances in space research*, *8*(8), 15-24.

Grebowsky, J. M. (1970). Model study of plasmapause motion. *Journal of Geophysical Research*, *75*(22), 4329-4333.

Grebowsky, J. M. (1971). Time‐dependent plasmapause motion. *Journal of Geophysical Research*, *76*(25), 6193-6197.

Higel, B., and Lei, W. (1984). Electron density and plasmapause characteristics at 6.6 RE: A statistical study of the GEOS 2 relaxation sounder data. *Journal of Geophysical Research: Space Physics*, *89*(A3), 1583-1601.

Horwitz, J. L. (1980). Conical distributions of low‐energy ion fluxes at synchronous orbit. *Journal of Geophysical Research: Space Physics*, *85*(A5), 2057-2064.

Horwitz, J. L., Comfort, R. H., and Chappell, C. R. (1984). Thermal ion composition measurements of the formation of the new outer plasmasphere and double plasmapause during storm recovery phase. *Geophysical research letters*, *11*(8), 701-704.

Horwitz, J. L., Brace, L. H., Comfort, R. H., and Chappell, C. R. (1986). Dual‐spacecraft measurements of plasmasphere‐ionosphere coupling. *Journal of Geophysical Research: Space Physics*, *91*(A10), 11203-11216.

Horwitz, J. L., Comfort, R. H., and Chappell, C. R. (1990a). A statistical

characterization of plasmasphere density structure and boundary locations. *Journal of Geophysical Research: Space Physics*, *95*(A6), 7937-7947.

Horwitz, J. L., Comfort, R. H., Richards, P. G., Chandler, M. O., Chappell, C. R., Anderson, P., Hanson, W. B., and Brace, L. H. (1990b). Plasmasphere‐ionosphere coupling: 2. Ion composition measurements at plasmaspheric and ionospheric altitudes and comparison with modeling results. *Journal of Geophysical Research: Space Physics*, *95*(A6), 7949-7959.

Hotta, Y., Furudate, M., Yamamoto, M., and Watanabe, M. (2002). Design and fabrication of multilayer mirrors for He-II radiation. *Surface Review and Letters*, *9*(01), 571-576.

Hozumi, Y., Saito, A., Yoshikawa, I., Yamazaki, A., Murakami, G., Yoshioka, K., and Chen, C. H. (2017). Global distribution of the He^+ column density observed by Extreme Ultra Violet Imager on the International Space Station. *Journal of Geophysical Research: Space Physics*, *122*(7), 7670-7682.

Khazanov, G. V., Khabibrakhmanov, I. K., and Glocer, A. (2012). Kinetic description of ionospheric outflows based on the exact form of Fokker‐Planck collision operator: Electrons. *Journal of Geophysical Research: Space Physics*, *117*(A11).

Kunieda, H., Yamashita, K., Yamazaki, T., Ikeda, K., Misaki, K., Takizawa, Y., Nakamura, M., Yoshikawa, I., and Yamaguchi, A. (1996, January). EUV observation with normal incidence multilayer telescopes. In *International Astronomical Union Colloquium* (Vol. 152, pp. 21-26). Cambridge University Press.

Murakami, G., Yoshikawa, I., Obana, Y., Yoshioka, K., Ogawa, G., Yamazaki, A., Kagitani, M., Taguchi, M., Kikuchi, M., Kameda, S., and Nakamura, M. (2010). First sequential images of the plasmasphere from the meridian perspective observed by KAGUYA. *Earth, Planets and Space*, *62*(4), e9-e12.

Murakami, G., Sakai, K., Homma, T., Yoshioka, K., Yoshikawa, I., Ichimaru, S., and Takenaka, H. (2011). Performance of Y2O3/Al multilayer coatings for the

He-II radiation at 30.4 nm. *Review of Scientific Instruments*, *82*(3), 033106.

Murakami, G., Yoshikawa, I., Yoshioka, K., Yamazaki, A., Kagitani, M., Taguchi, M., Kikuchi, M., Kameda, S., and Nakamura, M. (2013). Plasmaspheric filament: an isolated magnetic flux tube filled with dense plasmas. *Geophysical Research Letters*, *40*(2), 250-254.

Meier, R. R., and Weller, C. S. (1972). EUV resonance radiation from helium atoms and ions in the geocorona. *Journal of Geophysical Research*, *77*(7), 1190-1204.

Nagai, T., Horwitz, J. L., Anderson, R. R., and Chappell, C. R. (1985). Structure of the plasmapause from ISEE 1 low‐energy ion and plasma wave observations. *Journal of Geophysical Research: Space Physics*, *90*(A7), 6622-6626.

Nakamura, M., Yamashita, K., Yoshikawa, I., Shiomi, K., Yamazaki, A., Sasaki, S., Takizawa, Y., Hirahara, M., Miyake, W., Saito, Y., and Chakrabarti, S. (1999). Helium observation in the Martian ionosphere by an X-ray ultraviolet scanner on Mars orbiter NOZOMI. *Earth, planets and space*, *51*(1), 61-70.

Nakamura, M., Yoshikawa, I., Yamazaki, A., Shiomi, K., Takizawa, Y., Hirahara, M., Yamashita, K., Saito, Y., and Miyake, W. (2000). Terrestrial plasmaspheric imaging by an extreme ultraviolet scanner on Planet‐B. *Geophysical research letters*, *27*(2), 141-144.

Obana, Y., Murakami, G., Yoshikawa, I., Mann, I. R., Chi, P. J., and Moldwin, M. B. (2010). Conjunction study of plasmapause location using ground‐based magnetometers, IMAGE‐EUV, and Kaguya‐TEX data. *Journal of Geophysical Research: Space Physics*, *115*(A6).

Ogawa, T., and Tohmatsu, T. (1971). Sounding rocket observation of helium 304‐and 584‐A glow. *Journal of Geophysical Research*, *76*(25), 6136-6145.

Olsen, R. C., Shawhan, S. D., Gallagher, D. L., Green, J. L., Chappell, C. R., and Anderson, R. R. (1987). Plasma observations at the Earth's magnetic equator. *Journal of Geophysical Research: Space Physics*, *92*(A3), 2385-2407.

Park, C. G. (1970). Whistler observations of the interchange of ionization between the ionosphere and the protonosphere. *Journal of Geophysical Research*, *75*(22),

4249-4260.

Pelizzo, M. G., Corso, A. J., Zuppella, P., Nicolosi, P., Fineschi, S., Seely, J. F., Kjornrattanawanich, B., and Windt, D. L. (2012). Long-term stability of Mg/SiC multilayers. *Optical Engineering*, *51*(2), 023801.

Rasmussen, C. E., and Schunk, R. W. (1988). Multistream hydrodynamic modeling of interhemispheric plasma flow. *Journal of Geophysical Research: Space Physics*, *93*(A12), 14557-14565.

Roelof, E. C., Mauk, B. H., and Meier, R. R. (1992, June). Instrument requirements for imaging the magnetosphere in extreme ultraviolet and energetic neutral atoms derived from computer-simulated images. In *Instrumentation for Magnetospheric Imagery* (Vol. 1744, pp. 19-30).

Sandel, B. R., Broadfoot, A. L., Curtis, C. C., King, R. A., Stone, T. C., Hill, R. H., Chen, J., Siegmund, O. H. W., Raffanti, R., Allred, D. D., Turley, R. S., and Gallagher, D. L. (2000). The extreme ultraviolet imager investigation for the IMAGE mission. In *The IMAGE Mission* (pp. 197-242). Springer, Dordrecht.

Sandel, B. R., King, R. A., Forrester, W. T., Gallagher, D. L., Broadfoot, A. L., and Curtis, C. C. (2001). Initial results from the IMAGE extreme ultraviolet imager. *Geophysical research letters*, *28*(8), 1439-1442.

Sandel, B. R. (2011). Composition of the plasmasphere and implications for refilling. *Geophysical Research Letters*, *38*(14).

Schulz, M., and Koons, H. C. (1972). Thermalization of colliding ion streams beyond the plasmapause. *Journal of Geophysical Research*, *77*(1), 248-254.

Singh, N., and Horwitz, J. L. (1992). Plasmasphere refilling: Recent observations and modeling. *Journal of Geophysical Research: Space Physics*, *97*(A2), 1049-1079.

Sojka, J. J., and Wrenn, G. L. (1985). Refilling of geosynchronous flux tubes as observed at the equator by GEOS 2. *Journal of Geophysical Research: Space Physics*, *90*(A7), 6379-6385.

Soufli, R., Windt, D. L., Robinson, J. C., Baker, S. L., Spiller, E., Dollar, F. J., Andrew, L. A., Gullikson, E. M., Kjornrattanawanich, B., Seely, J. F., and Golub, L.

(2005, September). Development and testing of EUV multilayer coatings for the atmospheric imaging assembly instrument aboard the Solar Dynamics Observatory. In *Solar Physics and Space Weather Instrumentation* (Vol. 5901, p. 59010M). International Society for Optics and Photonics.

Soufli, R., Fernández-Perea, M., Robinson, J. C., Baker, S. L., Alameda, J., and Gullikson, E. M. (2012, September). Corrosion-resistant high-reflectance Mg/SiC multilayer coatings for solar physics in the 25-80 nm wavelength region. In *Space Telescopes and Instrumentation 2012: Ultraviolet to Gamma Ray* (Vol. 8443, p. 84433R). International Society for Optics and Photonics.

Spasojevic, M., and Sandel, B. R. (2010, January). Global estimates of plasmaspheric losses during moderate disturbance intervals. In *Annales geophysicae: atmospheres, hydrospheres and space sciences* (Vol. 28, No. 1, p. 27).

Takenaka, H., Ichimaru, S., Ohchi, T., and Gullikson, E. M. (2005). Soft-X-ray reflectivity and heat resistance of SiC/Mg multilayer. *Journal of electron spectroscopy and related phenomena*, *144*, 1047-1049.

Toyota, T., Murakami, G., Yoshioka, K., and Yoshikawa, I. (2007, September). Performance of newly developed Mg/SiC multilayer mirrors. In *Advances in X-Ray/EUV Optics and Components II*(Vol. 6705, p. 67050V). International Society for Optics and Photonics.

Taylor, H. A., Brinton, H. C., and Smith, C. R. (1965). Positive ion composition in the magnetoionosphere obtained from the Ogo‐A satellite. *Journal of Geophysical Research*, *70*(23), 5769-5781.

Yamashita, K., Takahashi, S., Kitamoto, S., Takahama, S., Tamura, K., Hatsukade, I., Sakurai, M., Watanabe, M., Yamaguchi, A., Nagata, H., and Ohtani, M. (1992). Characterization of multilayer reflectors and position sensitive detectors in the 45–300 Å region. *Review of scientific instruments*, *63*(1), 1513-1515.

Yamazaki, A., Yoshikawa, I., Shiomi, K., Takizawa, Y., Miyake, W., and Nakamura, M. (2006). Latitudinal variation of the solar He I 58.4 nm irradiance from the optical observation of the interplanetary He I emission. *Journal of Geophysical*

Research: Space Physics, *111*(A6).

Yoshikawa, I., Nakamura, M., Hirahara, M., Takizawa, Y., Yamashita, K., Kunieda, H., Yamazaki, T., Misaki, K., and Yamaguhi, A. (1997). Observation of He II emission from the plasmasphere by a newly developed EUV telescope on board sounding rocket S‐520‐19. *Journal of Geophysical Research: Space Physics*, *102*(A9), 19897-19902.

Yoshikawa, I., Yamazaki, A., Shiomi, K., Yamashita, K., Takizawa, Y., and Nakamura, M. (2000). Evolution of the outer plasmasphere during low geomagnetic activity observed by the EUV scanner onboard Planet‐B. *Journal of Geophysical Research: Space Physics*, *105*(A12), 27777-27789.

Yoshikawa, I., Yamazaki, A., Shiomi, K., Yamashita, K., Takizawa, Y., and Nakamura, M. (2001). Interpretation of the He II (304 Å) EUV image of the inner magnetosphere by using empirical models. *Journal of Geophysical Research: Space Physics*, *106*(A11), 25745-25758.

Yoshikawa, I., Murachi, T., Takenaka, H., and Ichimaru, S. (2005). Multilayer coating for 30.4 nm. *Review of scientific instruments*, *76*(6), 066109.

Yoshikawa, I., Yamazaki, A., Murakami, G., Yoshioka, K., Kameda, S., Ezawa, F., Toyota, T., Miyake, W., Taguchi, M., Kikuchi, M., and Nakamura, M. (2008). Telescope of extreme ultraviolet (TEX) onboard SELENE: science from the Moon. *Earth, planets and space*, *60*(4), 407-416.

Yoshikawa, I., Murakami, G., Ogawa, G., Yoshioka, K., Obana, Y., Taguchi, M., Yamazaki, A., Kameda, S., Nakamura, M., Kikuchi, M., Kagitani, M., Okano, S., and Miyake, W. (2010). Plasmaspheric EUV images seen from lunar orbit: Initial results of the extreme ultraviolet telescope on board the Kaguya spacecraft. *Journal of Geophysical Research: Space Physics*, *115*(A4).

Zhu, J., Wang, Z., Zhang, Z., Wang, F., Wang, H., Wu, W., Zhang, S., Xu, D., Chen, L., Zhou, H., Huo, T., Cui, M., and Zhao, Y. (2008). High reflectivity multilayer for He-II radiation at 30.4 nm. *Applied optics*, *47*(13), C310-C314.

Zhu, J., Zhou, S., Li, H., Huang, Q., Wang, Z., Le Guen, K., Hu, M. -H., André, J. –M., and Jonnard, P. (2010). Comparison of Mg-based multilayers for solar He II

radiation at 30.4 nm wavelength. *Applied optics*, *49*(20), 3922-3925.

Zuccon, S., Garoli, D., Pelizzo, M. G., Nicolosi, P., Fineschi, S., and Windt, D. (2017, November). Multilayer coatings for multiband spectral observations. In *International Conference on Space Optics—ICSO 2006* (Vol. 10567, p. 105673J). International Society for Optics and Photonics.

Chapter 3. Development of the Absorption Cell

3.1. Introduction

Liquid water is considered a necessary condition for the development of complex organic molecules and the eventual formation of life in the universe. In this context, the water dissipation process can provide important information for estimating the past abundance and survival of water in planetary atmospheres.

In the lower atmosphere of planets, water molecules (H_2O) are photodissociated by sunlight mainly into hydrogen atoms and hydroxyl radicals. The generated hydrogen atoms are elevated to the ionosphere and only those atoms with kinetic energies higher than the gravitational potential energy can escape to interplanetary space by thermal dissipation, which is the main atmospheric escape process.

Hydrogen atoms in planetary exospheres resonantly scatter solar Lyman-alpha radiation (121.567 nm) and form planetary hydrogen coronas. In the optically thin region, the intensity of this emission is proportional to the density of the atom. Therefore, the density distribution of the hydrogen atoms can be estimated by measuring the intensity of the H Lyman-alpha radiation. Alternatively, the estimation of the Doppler temperature requires the shape of the H Lyman-alpha line whose width, for example, is $\sim 2\times10^{-3}$ nm at 500 K. The Imaging UltraViolet Spectrograph (IUVS) on board the MAVEN (Mars Atmosphere and Volatile EvolutioN) spacecraft was launched in November 2013 as part of a NASA large exploration mission. Even this large instrument (outer envelope dimensions of $617 \times 541 \times 231$ mm^3 for 26.8 kg [*McClintock et al.*, 2015]) with a high spectral resolution capability in the echelle mode cannot capture the profile of the Lyman-alpha line [*Clarke et al.*, 2017]. In order to measure the line shape with a spectrometer, a considerably larger size payload would be required. Therefore, if the development of smaller and lighter spacecraft-borne instruments for observing planetary coronas can be realized, that would increase the chances of participating in future space missions.

The intensity of the Earth's hydrogen corona is sensitive to electromagnetic disturbances by solar winds. Lyman-alpha detectors [*Nass et al.,* 2006; *McComas et al.,* 2009] installed on the Two Wide-angle Imaging Neutral-atom Spectrometers (TWINS) of an Earth-orbiting satellite mission, recorded detailed images of the geocorona [*Bailey and Gruntman,* 2011]. The detectors also found that the neutral hydrogen density increases by 6-17% during geomagnetic storms [*Bailey and Gruntman,* 2013]. The Hisaki satellite, launched in September 2013, is equipped with the extreme ultraviolet spectrometer (EXtreme ultraviolet spectrosCope for ExosphEric Dynamics: EXCEED) [*Yoshioka et al.,* 2013; *Yoshikawa et al.,* 2014]. EXCEED acquires spectroscopic images (52-148 nm spectral range) of the atmospheres/magnetospheres of planets from the Earth-orbiting. The images taken by EXCEED also contain the geocoronal emissions because the instrument observes the targets from within the terrestrial exosphere (~1000 km). Using the geocoronal emissions data obtained by the Hisaki satellite, *Kuwabara et al.* [2017] revealed that the neutral hydrogen density variations is explained in terms of the charge exchange with plasmaspheric ions. Imaging observations of the geocorona from the outside the terrestrial exosphere were also conducted by *Kameda et al.* [2017] using the Lyman Alpha Imaging CAmera (LAICA) onboard the ultra-small deep space explorer, PRoximate Object Close flYby with Optical Navigation (PROCYON) [*Funase et al.,* 2015]. The instrument obtained the first image from deep space of the entire geocorona extending more than 38 Earth radii. They reproduced the observed intensity distribution using their proposed analytical model that contains exobase temperature, exobase density, and solar radiation pressure as parameters and suggested that the production of hot hydrogen atoms in the plasmasphere is not the dominant process shaping the outer hydrogen exosphere. Conditions for formation of coronae would be different in solar planets. These differences result from the individual planet's physical characteristics, for example, the intrinsic magnetic field, gravity, presence of a sea, and the atmospheric composition. Therefore, planetary corona observations are challenging and indispensable for understanding and modelling planetary atmospheres [*Chaffin et al.,* 2015].

Hydrogen absorption cell measurements are an efficient technique for remote

sensing of the density and temperature distributions of planetary hydrogen coronas. This technique has been primarily used to measure the geocorona [*Bertaux*, 1978]. The temperature distribution provides crucial information for quantitatively estimating the escape rate of hydrogen atoms present in a planetary atmosphere. In addition, the absorption cell technique has certain advantages over others in terms of geometrical size, weight, simplicity, and durability. Thus, the technique could be suitable for future small size satellite missions.

3.1.1. Early Observations using Absorption Cells

Observations using hydrogen/deuterium absorption cells onboard rockets or satellites have been conducted to measure the intensity of hydrogen Lyman-alpha line emission which is resonantly scattered by hydrogen atoms in planetary atmospheres or the interstellar medium. Morton and *Purcell* [1962] observed the hydrogen Lyman-alpha night glow of the terrestrial atmosphere using a hydrogen absorption cell on board a rocket for the first time.

Following this achievement, observations using absorption cells mounted on satellites have also been performed. The Lyman-alpha line shape in the terrestrial upper atmosphere was analyzed by a hydrogen absorption cell on board the OGO-5 satellite by *Bertaux and Blamont* [1971, 1981] and *Bertaux* [1978].

Bertaux et al. [1978, 1981] used hydrogen and deuterium absorption cells onboard Venera-9 and 10 to observe the day side hydrogen exosphere of Venus. From these observations, an exospheric temperature of 500 $\pm$ 100 K was estimated from both the scale height analysis and the line width measurements.

Bertaux et al. [1976] and *Babichenko et al.* [1977] reported that the temperature of interplanetary hydrogen near the Sun was 12000 K and 340 $\pm$ 30 K in the Martian upper atmosphere using the cells onboard Mars 4-7.

Lallement et al. [1984, 1985], *Bertaux and Lallement* [1984], and *Bertaux et al.* [1985] showed that the temperature of the interstellar medium (LISM) flowing in the solar system was 1800 K from the analysis of a spectral profile and a variation of

Doppler shift of the observed hydrogen Lyman-alpha emission from the LISM using hydrogen absorption cells onboard Prognoz 5 and 6.

The width of a hydrogen Lyman-alpha line can be measured by varying the width of the absorption profile. *Bertaux et al.* [1989] observed geocoronal and interplanetary hydrogen Lyman-alpha line emissions from instruments aboard Spacelab-1 and estimated their line shapes using this method.

As cited above, hydrogen absorption cell measurements are an efficient technique for remotely sensing the density and temperature distributions of planetary hydrogen coronas. The temperature distribution provides crucial information for quantitatively estimating the escape rate of hydrogen atoms present in the planetary atmosphere. In addition, the absorption cell technique has certain advantages over others in terms of geometrical size, weight, simplicity, and durability. Thus, the technique could be suitable for future small satellite missions.

An absorption cell photometer was mounted on the first Japanese Mars mission, NOZOMI [*Taguchi et al.*, 2000], but no data could be obtained because NOZOMI's orbit insertion was unsuccessful. In addition, due to limited development time, parameter optimization (i.e., filament shape, applied power, gas pressure, and others) for the absorption cells installed in the NOZOMI spacecraft was insufficient. Since the absorption performance is strongly dependent on these parameters, further optimization and study would be required for a future space mission.

In this study, I have focused mainly on the principle of thermal dissociation for the tungsten filament and constructed new hydrogen absorption cells for the evaluation of the absorption efficiency. Four types of filaments whose shapes were shorter and/or thinner than the ones previous studied were attached to the glass cells. An increase in the dissociation rate due to the new filament design was expected.

3.1.2. Purpose of this Chapter

I have mainly focused on the principle of thermal dissociation for the tungsten filament and constructed new hydrogen absorption cells for evaluation of the absorption

efficiency. Gas inlet ports allowed the H_2 gas pressure in the glass cells to be controlled for the performance evaluation. Four types of filaments whose shapes were shorter and/or thinner than the ones previously studied were attached to the glass cells. An increase in the dissociation rate due to the new filament design was expected.

To develop and optimize the design of the absorption cells for future missions, the performances of the new cells were evaluated using the French synchrotron facility, SOLEIL, in July 2016. Absorption profile dependences were obtained for filament length and diameter (1), applied power to the filaments (2), hydrogen gas pressure (3), and optical path length of the cell (4). Here we present and analyze the experimental results and discuss perspectives for future development and application of the absorption cell technique.

3.2. Absorption Cell Technique

3.2.1. Principle

The hydrogen absorption cell technique provides scientists with the density and temperature distributions of hydrogen coronas.

A hydrogen absorption cell consists of a soft cylindrical glass tube and two magnesium fluoride (MgF_2) windows fused to both sides of the cylinder. The windows are transparent to vacuum ultraviolet (VUV) radiation down to ~115 nm. The cells are filled with hydrogen molecules. When the filaments inside the cell are turned on, the hydrogen molecules thermally dissociate into two ground state hydrogen atoms. Hydrogen Lyman-alpha emissions from the atmosphere enter the cell through the MgF_2 window and are absorbed by the hydrogen atoms which transition into the excited state n = 2. When the density of hydrogen atoms is sufficient, the medium in the cell becomes optically thick for the Lyman-alpha radiation. The radiation is transmitted through the cell when the filaments are turned off. The intensity of the hydrogen Lyman-alpha emission is obtained by subtracting the VUV intensity through the cell when the filaments are turned on from the intensity when the filaments are turned off.

Figure 3.1 shows the conceptual diagram for estimating Doppler temperature. The absorption profile depends on the temperature and number density of the atoms in the cell. When the power applied to the filaments is low, the hydrogen molecules are insufficiently dissociated. Due to the low number density and temperature, the medium is optically thin at the hydrogen Lyman-alpha wavelength, and the width of the absorption spectrum is narrow. When the applied power is high, the medium becomes optically thick and the spectral width increases. Thus, the amount of transmitted light passing through the cell varies in response to the absorption profile. Comparing measured Lyman-alpha intensities with different absorption profiles calibrated during ground operations enables the estimation of the source atmosphere Doppler temperature.

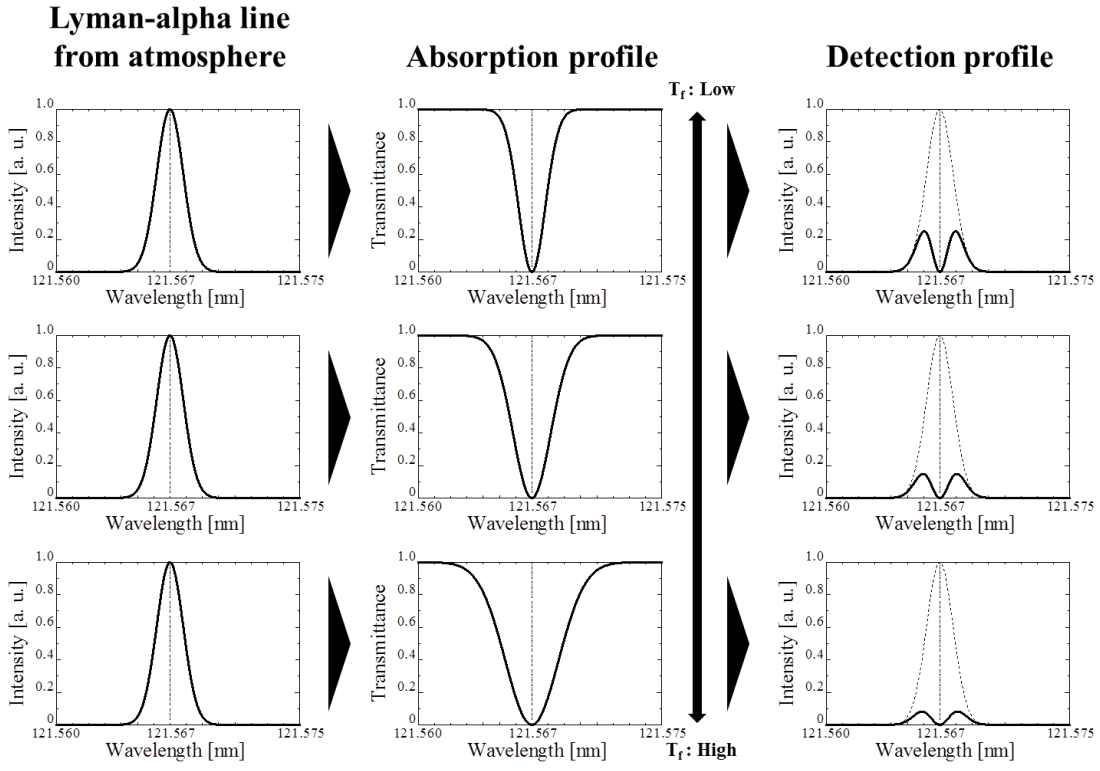

Figure 3.1. Conceptual diagram of the Doppler temperature detection. Changing the power applied to the filaments (i.e., filament temperature, T_f) changes the absorption profile. The Doppler temperature can be estimated by calculating the respective absorption profiles from the detected transmitted light.

3.2.2. Performance Evaluation of the Improved Absorption Cells

I have developed two new absorption cells based on those designed for the NOZOMI mission. *Kawahara et al.* [1997] described the prototype hydrogen/deuterium absorption cells developed for the mission in detail. The UVS-P photometer on board NOZOMI (launched in 1998) consists of the hydrogen/deuterium cells developed by *Taguchi et al.* [2000] based on the prototype cells [*Kawahara et al.*, 1997]. Here, in order to systematically study the cell performance, optical thickness, and Doppler width for various specifications and conditions, I constructed the new cells with four different types of filaments. The specifications of the newly designed cells from this study are shown in Table 3.1 together with those from previous studies.

Table 3.1. Specifications of cells

	Cell Type	Diameter of Cell [mm]	Optical Path Length [mm]	Gas Press. [Pa]	Filament Material
This Study	Variable	47	100	Variable	Tungsten (Shown in Table 2)
	Variable	47	60		
Prototype	H cell	25	100	400	Tungsten (0.1 mmØ × 30 mm)
	D cell	50	60		
UVS-P	H cell	25	60	400	Tungsten (20 μmØ × 90 mm)
	D cell	25	60		

Four types of tungsten filaments with different lengths and diameters (Table 3.2) were attached to the new cells at sides I and II of the cells (Fig. 3.2). These filaments can be individually turned on/off. In addition, gas inlet ports were attached to feed H_2 molecules into the absorption cells. The cell performance was expected to be largely dependent on the filament shape and the H_2 pressure.

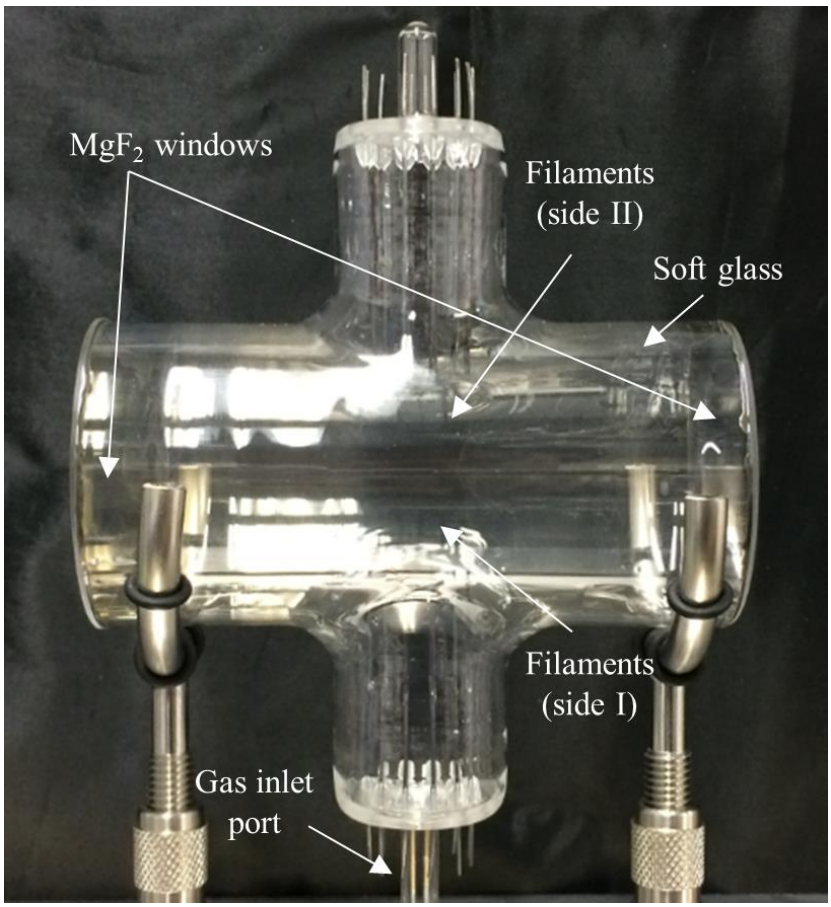

Figure 3.2. View of the new type of absorption cell (optical path length = 100 mm) designed for calibration purposes. The diameter of the effective area (MgF_2 windows) of the cell is 47 mm. Four types of filaments, as shown in Table 2, were attached to sides I and II of the cell. These eight filaments could be turned on/off independently. In order to change the gas pressure, a gas inlet port was used to feed H_2 into the cell. The H_2 gas pressure and the filament power could be changed from outside the chamber.

Table 3.2. Filament shape installed in the new cells

Filament type	Filament length [mm]	Diameter [μm]
Type-A	51.1	27.6
Type-B	28.5	27.6
Type-C	35.6	24.4
Type-D	20.8	24.4

3.3. Absorption Profile Measurement with a High-resolution Fourier Transform Spectrometer

The absorption profiles of various absorption cells were measured with a unique high-resolution Vacuum UltraViolet Fourier Transform Spectrometer (VUV-FTS) installed on the VUV undulator-based DESIRS beamline [*Nahon et al.*, 2012] at the Synchrotron SOLEIL, Saint Aubin in France. The branch performance has been described in detail previously [*de Oliveira et al.*, 2016], and only the details specific to the present experiment are discussed. The spectrometer was set to achieve a spectral resolution of 8.0×10^{-4} nm at 121.6 nm. The full undulator bandwidth (~7 nm) fed the FTS branch located upstream of the monochromator. The FTS allows broadband high-resolution absorption spectroscopy in the VUV down to 40 nm, see *de Oliveira et al.* [2016] for more details. Note that the efficiency of the instrument permitted a high-resolution, 7 nm bandwidth single scan in about 15 minutes. The short scan time is essential when several parameters need to be tested within the limited time allocated on the synchrotron beamline.

Measurements of the absorption profiles of the hydrogen cells were recorded by placing an absorption cell in a vacuum chamber. Figure 3.3 shows a schematic diagram of the measurement configuration. The cell was set on an XZ translation stage and installed in the FTS branch vacuum chamber of the DESIRS beamline. The undulator beam passed through the cell and the transmitted light was recorded by the

FTS instrument downstream. The applied power to the filaments and the H_2 gas pressure in the glass cell were regulated from outside the chamber. The outside of the gas inlet port was connected to a gas cylinder and a vacuum pump. The evacuation and injection of H_2 gas were performed before each measurement and the gas pressure could be adjusted with an accuracy of ~10 Pa. The purity of the H_2 gas was > 99.9995%.

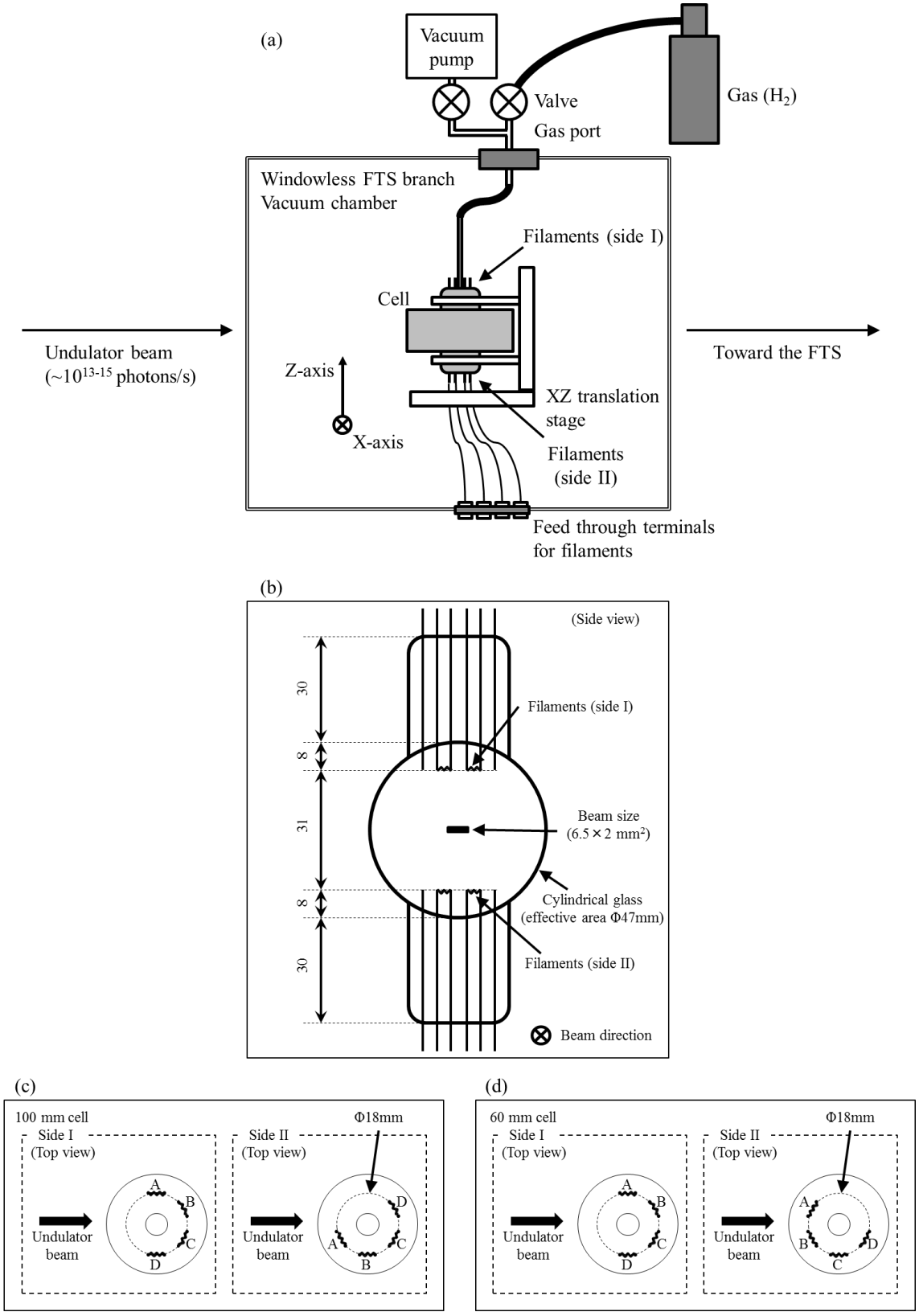

Figure 3.3. (a) Cross-sectional diagram of the measurement configuration. The VUV synchrotron beam travels through the absorption cell before entering the FTS. The cell

on the XZ translation stage is placed in the vacuum chamber (pressure $\sim 5\times10^{-5}$ Pa). The power applied to the filaments and the gas pressure in the cell can be changed from outside the chamber. (b) Side view of the new cell. The undulator beam (6.5×2 mm^2) passes through near the center of the glass. (c) Filament locations on sides I and II in the 100 mm cell. (d) Filament locations on sides I and II in the 60 mm cell. Figures not to scale.

3.4. Data Analysis

According to the Beer-Lambert law, the intensity of the light transmitted through the cell can be expressed by the following equation:

$$I(\lambda) = I_0 \exp\left\{-\tau_0 \exp\left[-\left(\frac{\lambda-\lambda_0}{\Delta\lambda}\right)^2\right]\right\} \tag{3-1}$$

Here, I_0 is the incident synchrotron radiation which is constant in the vicinity of the line, λ_0 is the Lyman-alpha absorption line center, τ_0 is the optical thickness at $\lambda = \lambda_0$, and $\Delta\lambda$ is the Doppler width of the hydrogen atoms in the cell. The H (n = 2) lifetime, the Stark, and the collisional broadenings are neglected, therefore, the optical thickness can be described as the Doppler Gaussian-shape function within a good approximation. However, the observed transmission should be modified in order to account for the instrumental response function according to:

$$I_{obs}(\lambda) = \frac{\int I(\lambda)\Gamma(\lambda-\lambda')d\lambda'}{\int \Gamma(\lambda-\lambda')d\lambda'} \tag{3-2}$$

The observed absorption spectrum is the convolution of the true line profile with the FTS apparatus function $\Gamma(\lambda)$, which is a well characterized sinc function:

$$\Gamma(\lambda) = \frac{\sin(\pi \times 1.2 \times \lambda / \Delta\lambda_{FTS})}{\pi \times 1.2 \times \lambda / \Delta\lambda_{FTS}} \tag{3-3}$$

$\Delta\lambda_{\mathrm{FTS}}$ is the FWHM of the sinc function arising from the FTS finite optical path difference and is directly related to the instrument spectral resolution. During the measurements, the instrument was set for $\Delta\lambda_{\mathrm{FTS}} = 8.0 \times 10^{-4}$ nm, which is roughly half the Doppler width of the atomic hydrogen Lyman-alpha transition at room temperature. This spectral resolution is sufficient to properly describe the line.

The optical thickness at $\lambda = \lambda_0$, τ_0, and the Doppler width, $\Delta\lambda$ will be considered as figures of merit. As the optical thickness becomes larger and the FWHM becomes wider, the amount of absorbed light increases. Consequently, the level of performance will be considerably higher. An absorption cell with high performances provides high tunability of the absorption thickness and then the Doppler temperature.

An optimization routine was developed based on a least-squares best-fit of $I_{obs}(\lambda)$ to the experimental absorption spectrum, with τ_0, $\Delta\lambda$ (temperature dependent), I_0, and λ_0 as free parameters. $\Delta\lambda_{FTS}$ was set to the theoretical value as described above. Figure 3.4 shows two examples with different applied powers. The model quite accurately reproduced the experimental data, however, the consistency was not perfect for the saturation level (zero transmission) as shown in Fig. 3.4 (b). This experimental artifact has been described previously [*de Oliveira et al.*, 2016], and is related to phase errors occurring in the FTS, and is probably due to the noisy environment of the synchrotron facility. Another report has revealed a small instrumental Gaussian broadening in the FTS that can be determined when the measured linewidth is narrow [*Heays et al.*, 2011]. The FWHM of this extra Gaussian broadening, whose origin is not fully identified, is $\sim 7.4 \times 10^{-5}$ nm and was completely neglected during the present study.

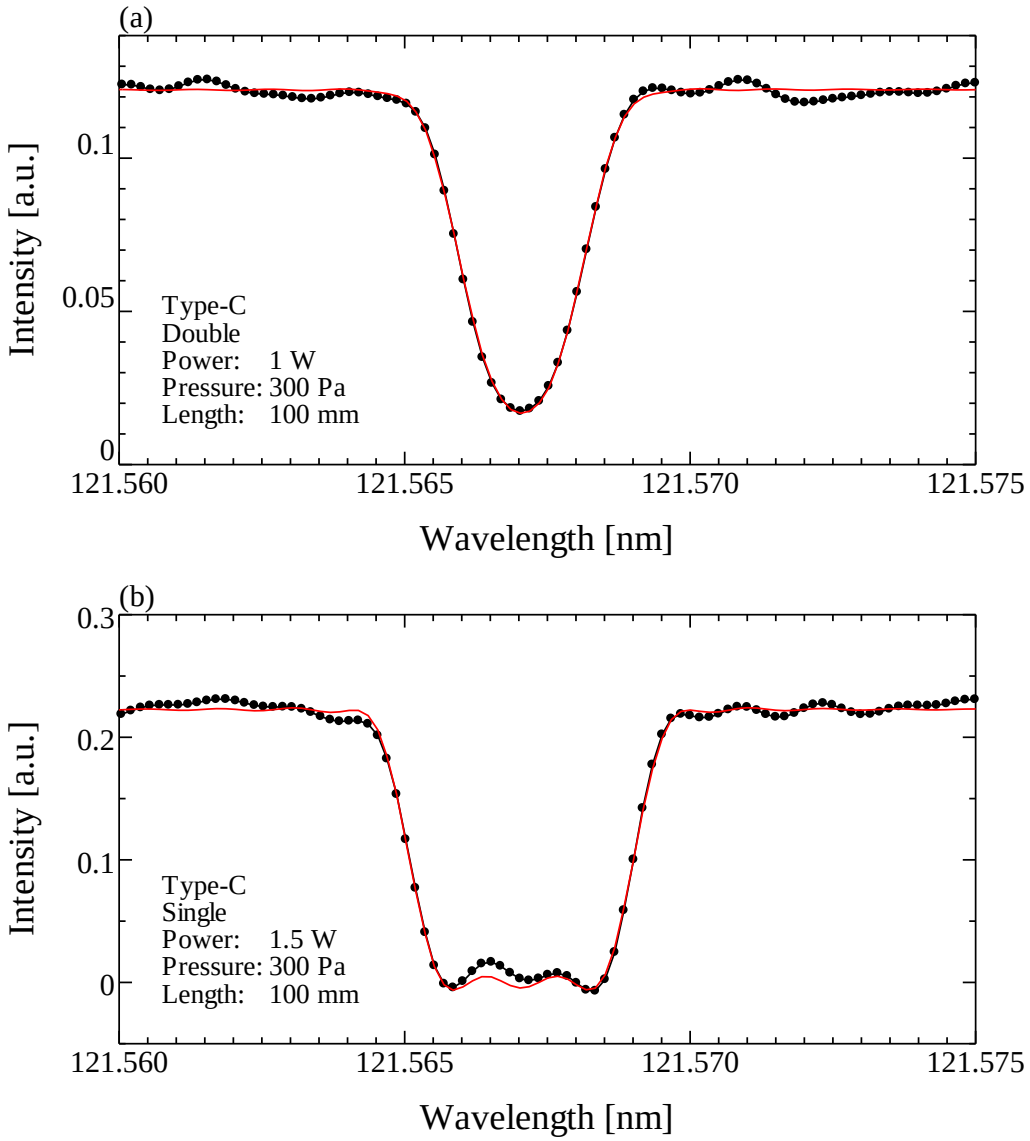

Figure 3.4. Obtained spectra near the center of the hydrogen Lyman-alpha line with two different applied powers (black circles). The model spectrum assumes a Doppler broadening (in red). The small regular oscillation is an instrumental effect due to the shape of the apparatus function; see text for details.

3.5. Results and Discussion

3.5.1. Dependence on the Filament Length and Diameter

Figures 3.5 and 3.6 show (a) the optical thicknesses and (b) the FWHMs ($2\sqrt{\ln 2} \times \Delta\lambda$) of the absorption profiles, respectively, for the 100 mm and 60 mm cells, with an H_2 pressure of 300 Pa and a filament power of 1.5 W. Four pairs of filaments were turned on/off on one side (single filament), or both sides (double filaments). The absorption profiles with all possible variable combinations could not be obtained due to limited beam time and thus, there are missing data in some of the figures. However, some insights can be inferred from the recorded data.

It was found that the optical thicknesses with filaments Type-C and -D were larger than those with Type-A and -B for both cell lengths. These results suggest that the thinner and shorter filaments provided higher performance. In contrast, no significant difference appeared in the FWHMs.

Hydrogen molecules dissociate into atoms when they collide with the filaments, and the thermal energy from the filaments causes the atoms to leave the surface. When the filaments are thinner and shorter, the filament temperature is generally high because of the higher power density. This leads to a higher dissociation rate and a larger optical thickness compared to the thicker and longer filaments.

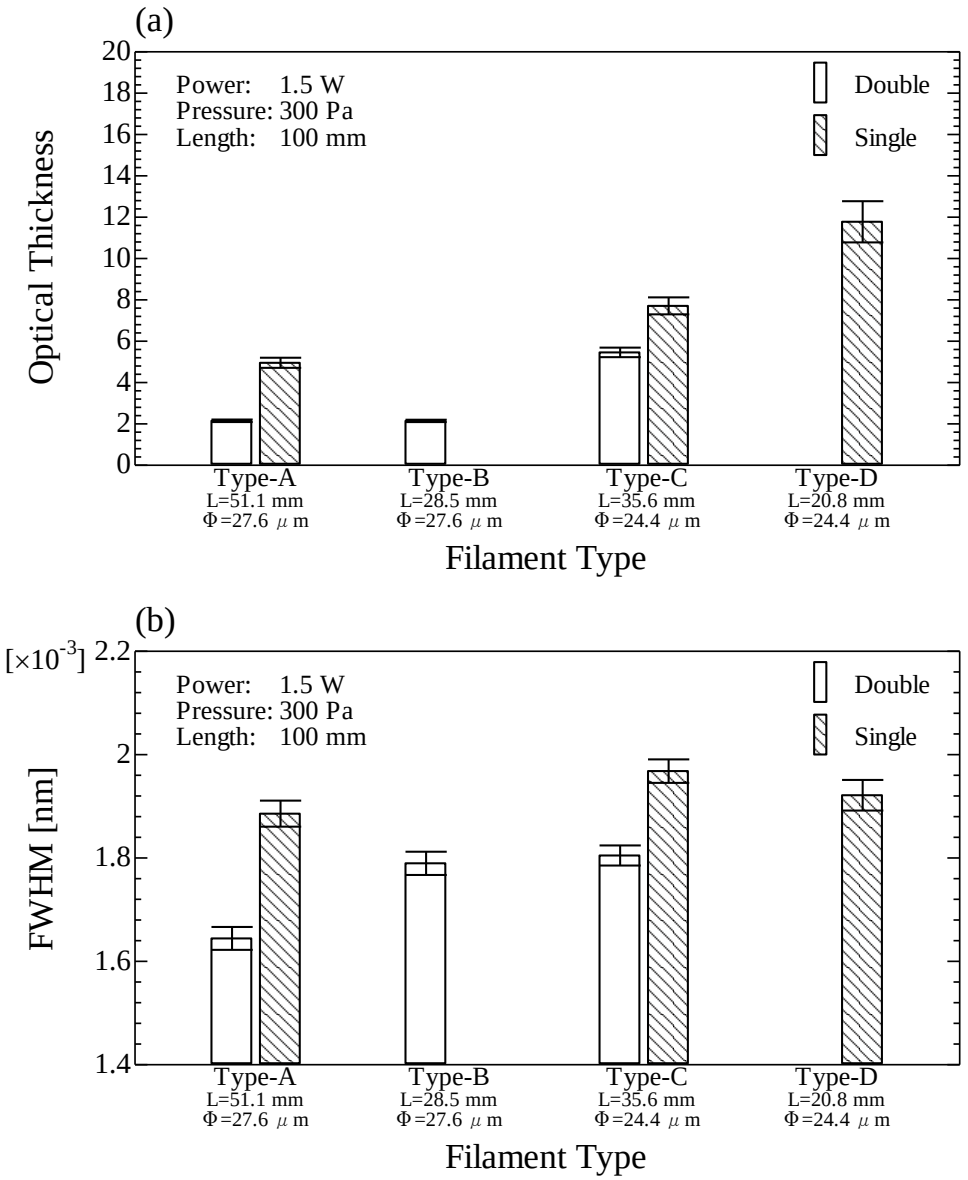

Figure 3.5. Optical thicknesses (a) and FWHMs (b) of the absorption profiles in the 100 mm cell using different filaments. The applied power was 1.5 W, and the H_2 gas pressure was 300 Pa. The white bars indicate the results when filaments on both sides were turned on. The black-hatched bars indicate the results when one filament on side I was turned on.

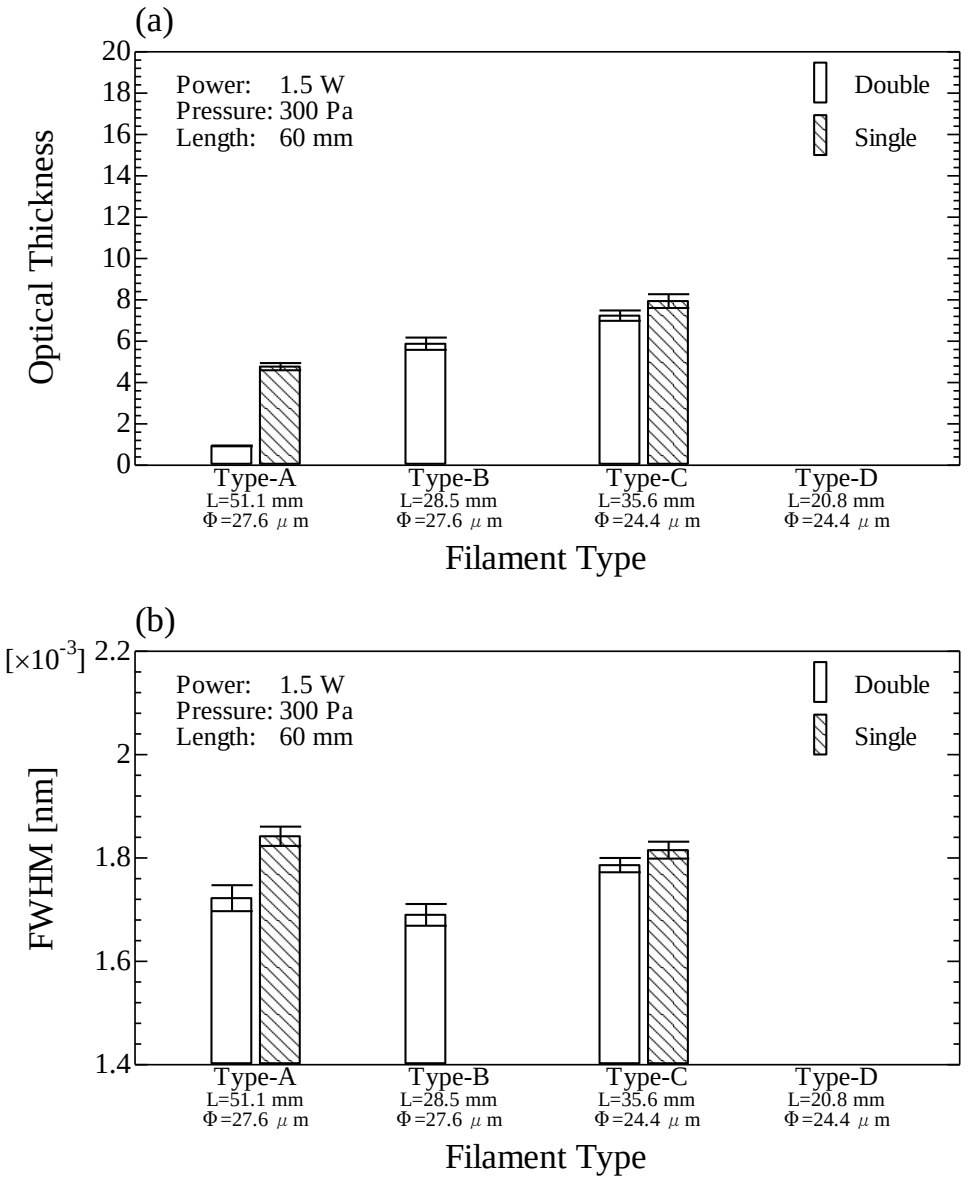

Figure 3.6. Optical thicknesses (a) and FWHMs (b) of the absorption profiles in the 60 mm cell using different filaments. The other experimental conditions are the same as in Fig. 3.5, except for the cell length.

3.5.2. Dependence on Applied Power and Optical Path Length

Figure 3.7 shows the power dependences of the performances with the new

cells and the Type-C filaments at an H_2 gas pressure of 300 Pa. The optical thicknesses increased with increasing the applied powers of the filaments in the range from 1 to 3 W. These observations might be explained in terms of the dissociation rate increasing with the filament temperature due to the applied power. However, at 3 W or more, the optical thicknesses seemed to reach a saturation level. The data for the absorption cells of the UVS-P and the prototype are also shown in Fig. 3.7 for comparison. The new cells showed a wider tunability for the optical thickness than the previous cells. The small optical thicknesses of the prototype cell by *Kawahara et al.* [1997] may be attributed to the thick filament used in their cell. A quasi-linear correlation between the applied power and the FWHM is shown in Fig. 3.7 (b). The energy of the hydrogen atoms desorbing from the tungsten filament surfaces is given by the thermal energy of the filaments. The filament temperature deduced from the tungsten resistivity increased quasi-linearly with the applied power. Therefore, the FWHM that was proportional to the square root of the gas temperature also increased quasi-linearly with the power. There is no clear explanation for the larger FWHM of the UVS-P.

It can be seen from Figs. 3.5-7 that practically no differences were observed between the 60 mm and 100 mm long cells. This suggests that hydrogen atoms produced in the vicinity of the filaments are quenched before diffusing to the MgF_2 windows and are not distributed uniformly along the beam path. This inhomogeneous distribution was also mentioned by *Kawahara et al.* [1997].

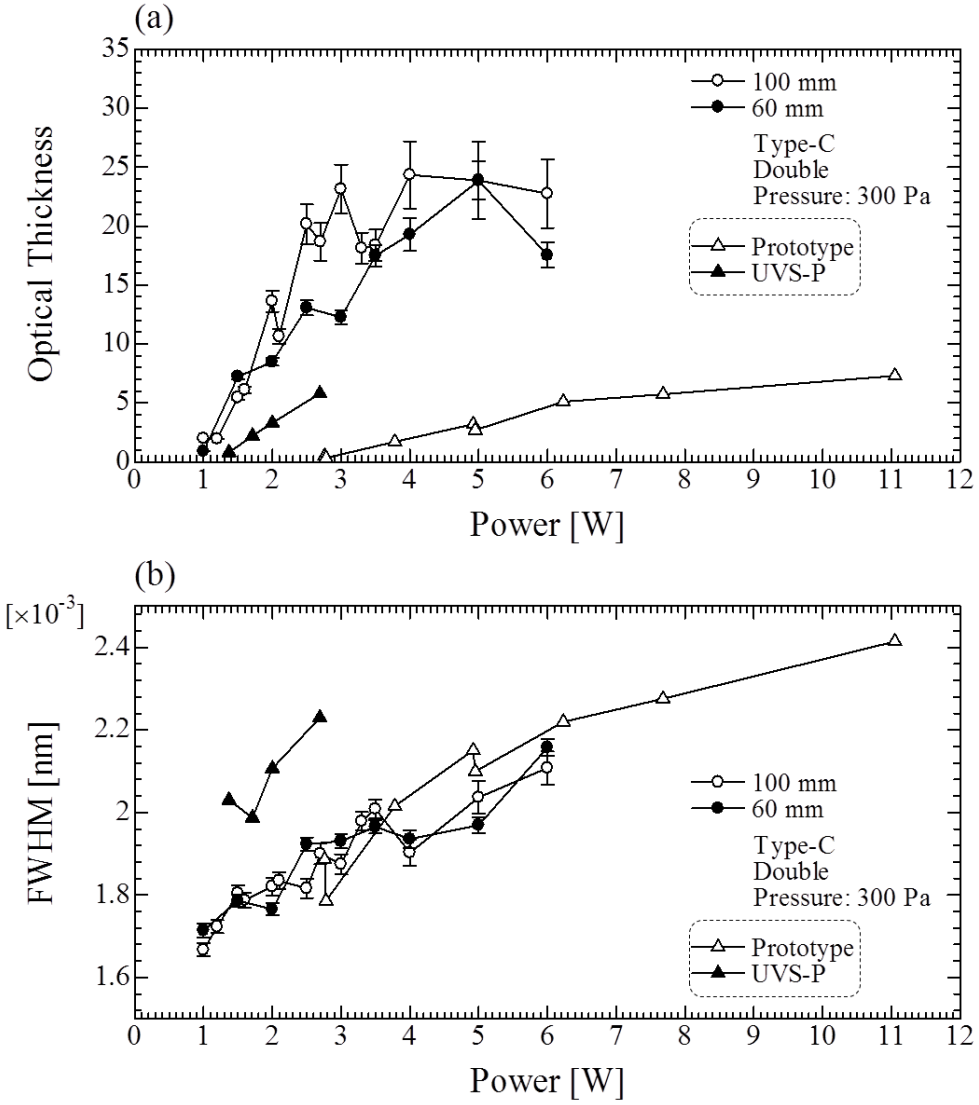

Figure 3.7. Optical thickness dependences (a) and FWHMs (b) of the absorption profiles on the applied power of the filaments. White circles indicate performances for the 100 mm cells. Black circles indicate performances for the 60 mm cells. Triangles show the performances of the UVS-P (black) and those of the prototype cells of *Kawahara et al.* [1997] (white).

3.5.3. Dependence on Gas Pressure

Figure 3.8 shows the pressure dependences of the performances with the Type-C filament at 1.5 W and the 100 mm cell. As the gas pressure increased, the

optical thickness decreased overall, but the thickness also peaked between 100 and 300 Pa. No pressure dependence was found regarding the FWHM. Since the applied power was constant, the following explanation is proposed. If the gas pressure increases, the heat conduction from the filaments to the hydrogen gas increases as well. Then, the temperature of the filaments only slightly rises and therefore, the dissociation rate of the molecules decreases. In contrast, if the pressure decreases, the number of atoms in the cell decreases and the optical thickness decreases as well.

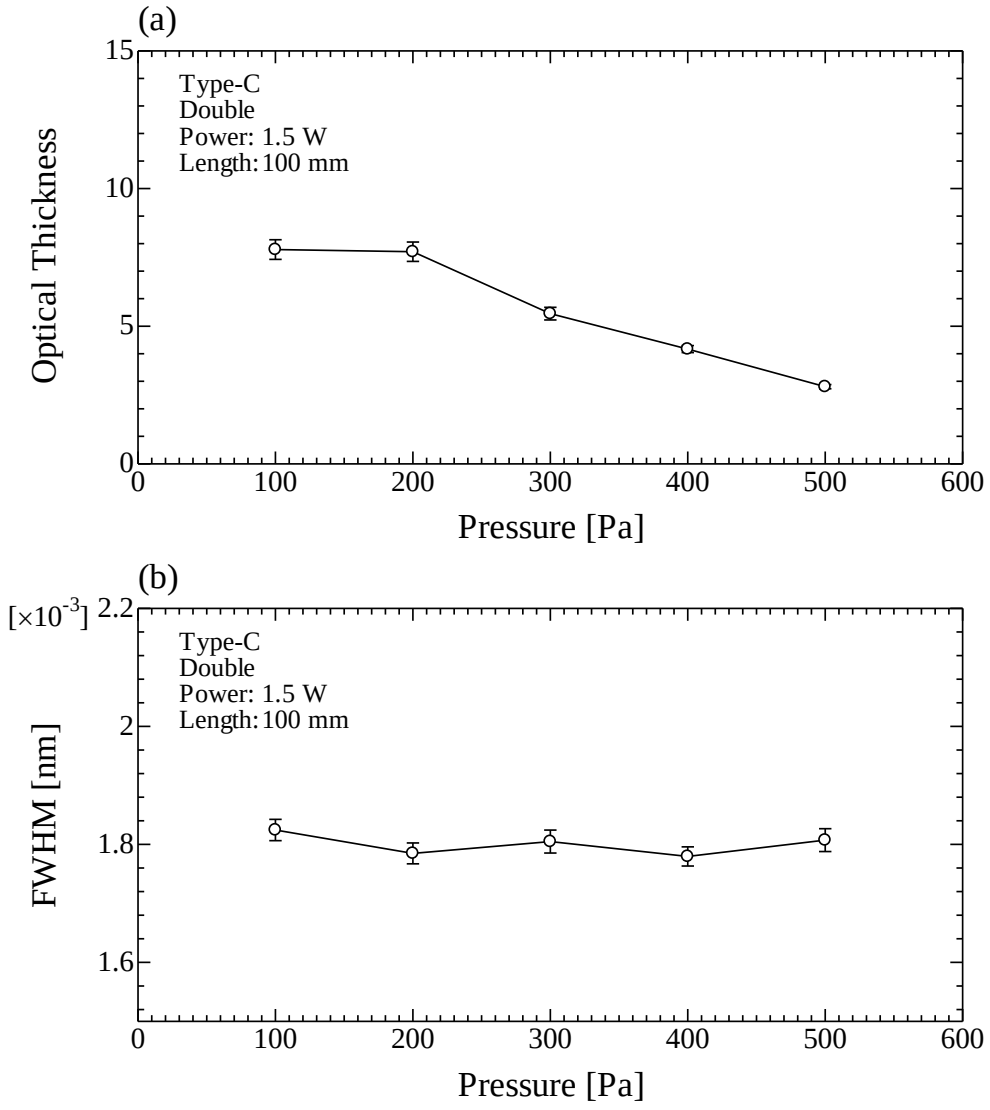

Figure 3.8. Optical thickness dependences (a) and FWHMs (b) of the absorption profiles versus the H_2 gas pressure.

3.5.4. Filament Temperature and Fraction of Dissociated Molecules Deduced from Measurement

Since the resistivity of tungsten depends on temperature, it is possible to estimate the temperature from the resistivity of a filament during heating. Therefore, the filament temperature can be deduced from the resistivity of a tungsten wire which is obtained from electric voltage and current measurements [*Lide*, 1994]. Figure 3.9 shows the relationship between the resistivity and the tungsten temperature. The red line in Figure 3.9 shows the result of a least-squares fitting to the experimental values indicated by white circles, and this function was used to derive the temperature.

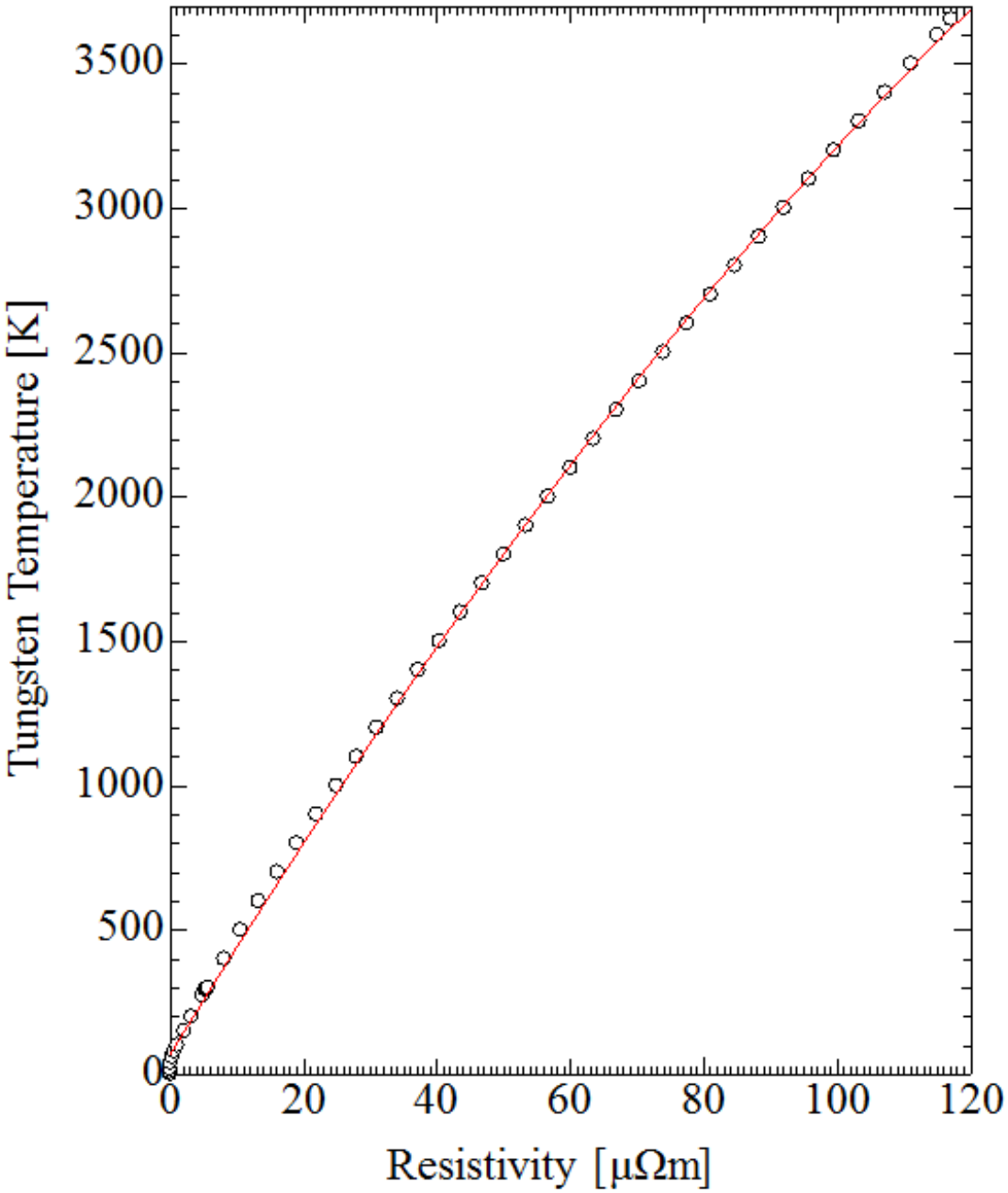

Figure 3.9. Relationship between resistivity and the tungsten temperature.

Figure 3.10 shows the relationship between the filament temperature and the atomic hydrogen gas temperature derived from the measured absorption profile. The atomic gas temperature, T_H, can be deduced from the Doppler broadening, $\Delta\lambda$, of the measured spectrum by the following:

$$\Delta\lambda = \frac{\lambda_0}{c}\sqrt{\frac{2kT_H}{m_H}} \tag{3-4}$$

In this equation, λ_0 is the center wavelength of the Lyman-alpha absorption, c is the speed of light, k is the Boltzmann constant, and m_H is the mass of the hydrogen atom. The atomic gas temperature increases linearly with filament temperature. The measured atomic hydrogen gas temperature was much lower than the temperature calculated for the filament. This observation is in good agreement with previous studies, in which the temperature difference between the filaments and H atoms was interpreted by considering that the temperatures derived from the FWHM was the average value of the atomic gas temperature along the beam path in the cell.

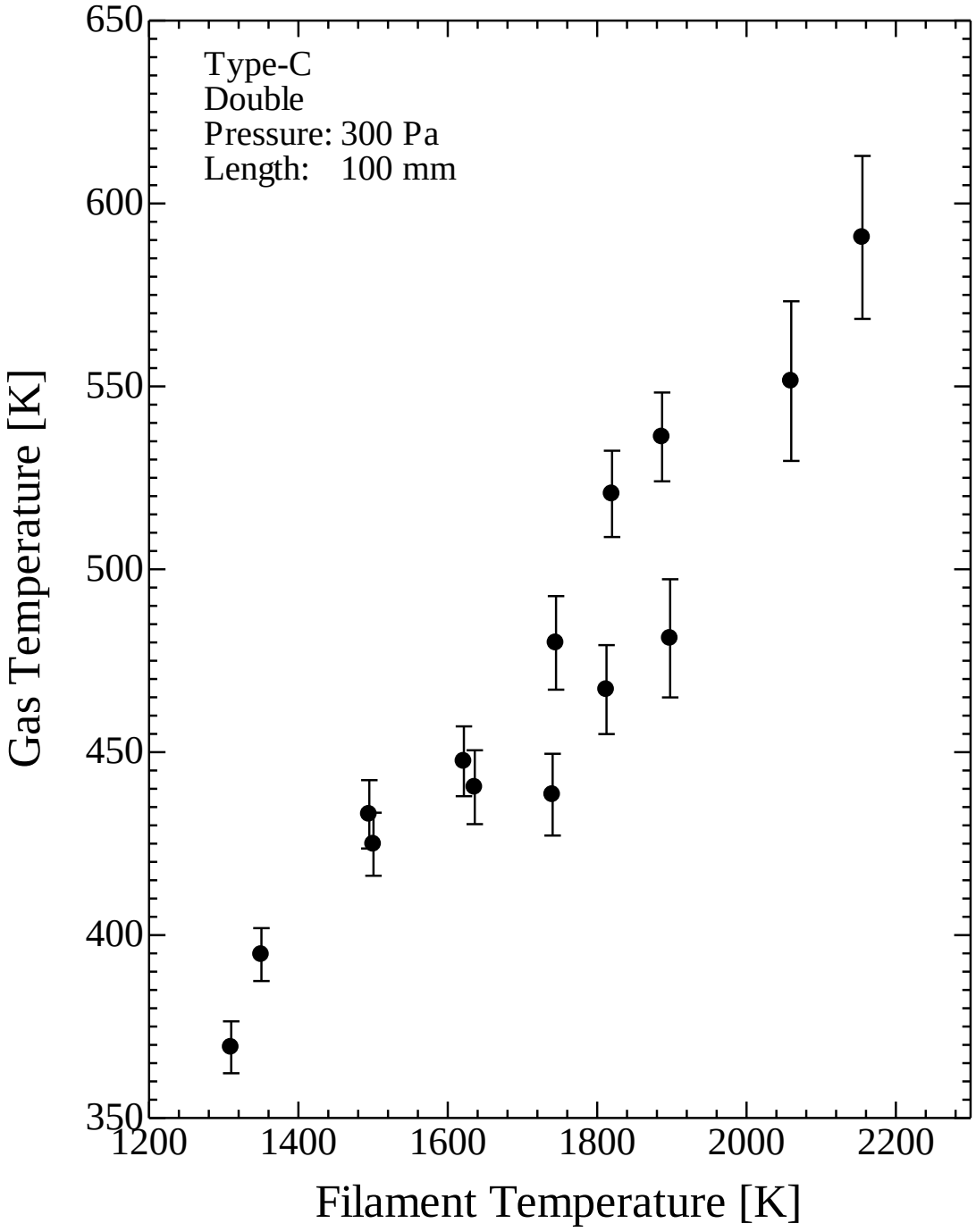

Figure 3.10. Relationship between the filament temperature and the atomic hydrogen gas temperature.

Following the Beer-Lambert law, the hydrogen atom density, n_H, can be obtained from $\tau_0 = n_H \sigma_0 L$, where L is the optical pass length in the cell and σ_0 is the

absorption cross section of hydrogen atoms at $\lambda = \lambda_0$ defined below as [*Meier and Prinz*, 1970]:

$$\sigma_0 = \frac{\sqrt{\pi} e^2 \lambda_0^2 f}{m_e c^2 \Delta\lambda} \tag{3-5}$$

In equation (3-5), f indicates the oscillator strength, 0.41641, for hydrogen atoms. m_e and e denote the mass and charge of the electron, respectively. In the thermal dissociation equilibrium, hydrogen atoms and hydrogen molecules obey the reaction, $H_2 \rightleftarrows 2H$, and a fraction of the dissociated molecules, α, can be calculated as below:

$$\alpha = \frac{n_H}{2n_0} \tag{3-6}$$

where n_0 is the density of hydrogen molecules which were filled into the cell in every measurements. Note that the n_H is considered to be the averaged value along the SR beam path length L in the absorption cell. Figure 3.11 shows the relationship between the filament temperature and the fraction of dissociated molecules. A higher fraction of atomic hydrogen was achieved in the new cells compared to the prototype cell. In addition, the fraction increased gradually and was almost constant for filament temperatures above ~1800 K, corresponding to an applied power of ~3 W. A similar trend was observed in the previous study by *Smith and Fite* [1962] who found that the dissociation efficiency of H_2 into H atoms on tungsten surfaces increases with an increasing tungsten temperature and approaches a limiting value above 2500 K. The optical thickness depends on filament temperature and increases with temperature. This is because reaction rates of dissociation and adsorption depend on the filament temperature, and the density of hydrogen atoms in the equilibrium state determined by the ratio of the rate constants that change depending on temperature. In Fig. 3.7 (a), the similar trend can be seen for optical thickness. After reaching the plateau, the number density of H atoms in the cell does not increase and is independent of the electrical

power. Further investigations in combination with simulations of the dissociation and recombination rates will be useful to understand more precisely the processes involved.

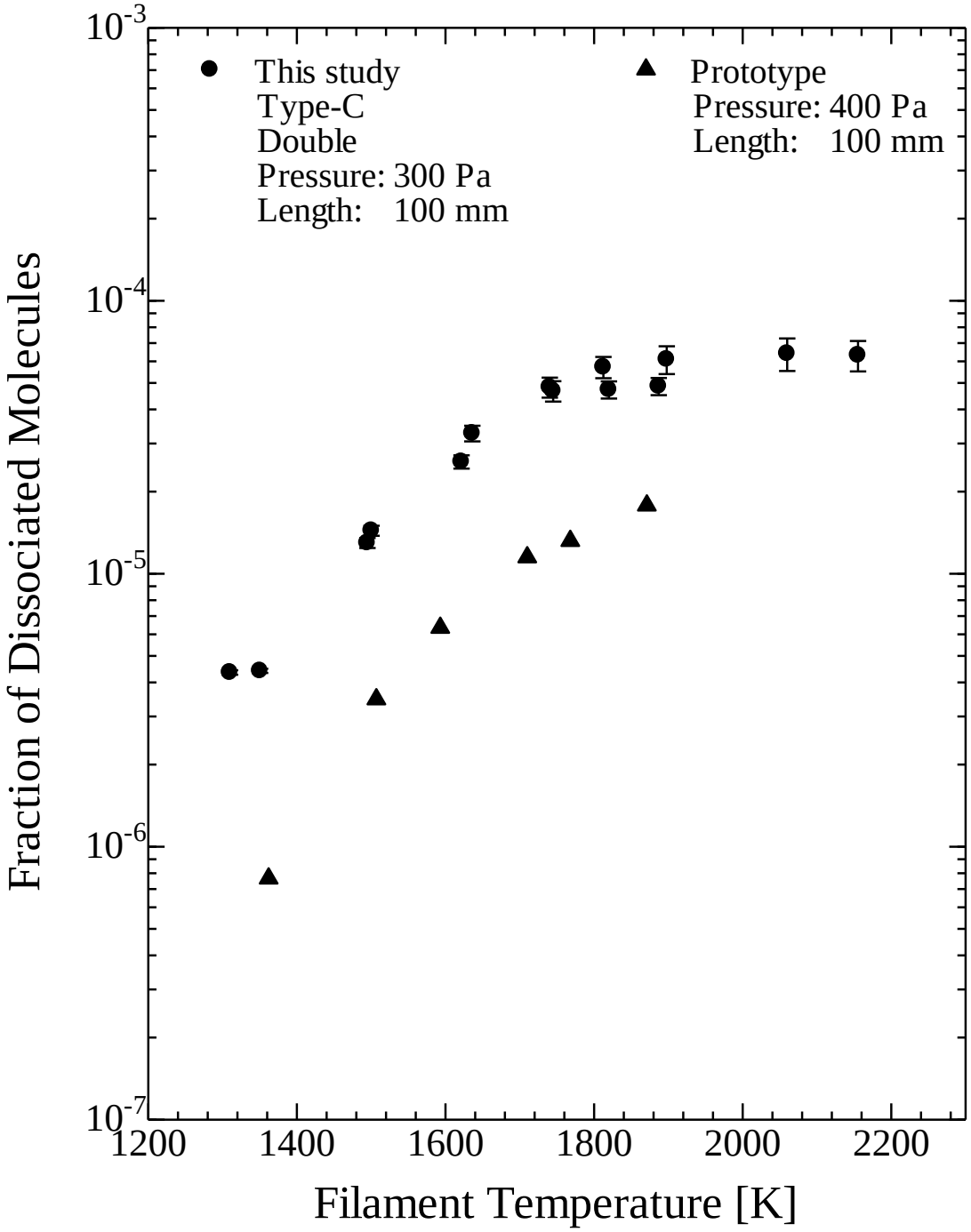

Figure 3.11. Relationship between the fraction of dissociated molecules and the filament temperature.

3.6. Feasibility Analysis for Martian Corona Observations using the Absorption Cell

It is worthwhile to simulate temperature measurements of the Martian corona by using the new absorption cell developed in this study. Based on the results of this experiment, simulated observations were created with the imager shown in Figure 3.12. I assumed the following conditions. For the observational geometry, the imager can perform spatial scanning by orbital motion by fixing one axis of the spacecraft in inertial space and can image the Martian limb as shown in Figure 3.13. During nominal observation field-of-view (FOV), the imager was set to $25.6 \times 25.6\, deg.^2$ ($256 \times 256\, bin^2, 0.1\, deg./bin$) and the acquired images were reduced to one-dimensional datum consisting of 256 points with 2 bytes. The sensitivity of the imager with a FOV of $25.6 \times 0.1\, deg^2$ was 12 cps/kR with consideration of the efficiencies of each optical component (Table 3.4). The brightness of the Martian hydrogen corona was 2 kR [*Feldman et al.*, 2011] and was 4450 cts with a 180-sec exposure. This value is sufficient to estimate the density and temperature of the hydrogen corona.

The dark current noise was 10.4 cps/cm^2 as described in Chapter 2. Assuming the above conditions, the result of the simulated temperature estimation is shown in Figure 3.14. During the error evaluation of the temperature estimation, the optical thickness and FWHM errors derived by fitting to experimental values were adopted as systematic errors. Statistical errors were also evaluated with the assumption that the counts followed the Poisson distribution. The sum of these errors was used as an estimate of the count variance errors. Difference in the transmittances increased with power consumption. Since the dynamic range of MCP is about 10^3, power consumption should be set to 2.5 W or less in order to detect signals above a dark current noise level.

One of the observation datasets is shown in Table 3.5. Five images can be acquired by varying the filament temperature. The measurement of the Martian hydrogen corona temperature is possible with a high accuracy of about 30 K as shown in Figure 3.15. The estimated temperature error was evaluated by fitting the expected

brightness from the performance of the absorption cell to pseudo observational data. Counts errors were assumed as a normal distribution with the variance estimated as described above. The estimated temperature variance of the observational target was used as the temperature estimation error by performing 5000 numerical experiments.

From past observations, it has been clarified that the Martian hydrogen corona has two high and low temperature components [*Chaufray et al.*, 2008]. In previous studies, there were ambiguities regarding the density and temperature of the hydrogen atoms when reproducing the observed intensity distributions in models [*Chaffin et al.*, 2013]. The dissipated hydrogen atoms amounts were insufficiently evaluated due to a scarcity of information related to the density and temperature [*Clarke et al.*, 2014]. The above problems can be overcome by observing the density and temperature distributions simultaneously with high accuracy using an absorption cell which would allow the dependences of the hydrogen atom dissipation rates on solar activity and season to be clarified.

To interpret the observations of the imager, the observed intensities were compared with the Chamberlain model for coronal brightness [*Chaufray et al.*, 2008; *Clarke et al.*, 2014; *Chaffin et al.*, 2015]. The best fit to the observed values was searched to find the exospheric density and temperature which minimized the chi-squared statistics as explained by *Chaffin et al.* [2015]. *Chaufray et al.* [2008] applied Chamberlain's approach to the observed intensity of hydrogen Lyman-alpha emission obtained by the SPICAM onboard Mars Express and achieved a reasonable fit for the set of observations by assuming an exobase temperature of 200-250 K and a density of $1\text{-}4 \times 10^5$ cm^{-3} in good agreement with photochemical models. *Clarke et al.* [2014] fit the model to observational results from the Hubble Space Telescope and reported a sudden variation in the intensity of the Martian hydrogen corona that decreased by 40% over 4 weeks. It was suggested that the seasonal change in the amount of water vapor in the lower atmosphere may have caused the variation. *Chaffin et al.* [2015] captured the first three-dimensional distribution of the Martian hydrogen corona using MAVEN/IUVS. Although the distribution had been hypothesized to be symmetrically spherical, they revealed that the distribution departed from spherical

symmetry at higher altitude. It is necessary to observe the Martian hydrogen corona in more detail.

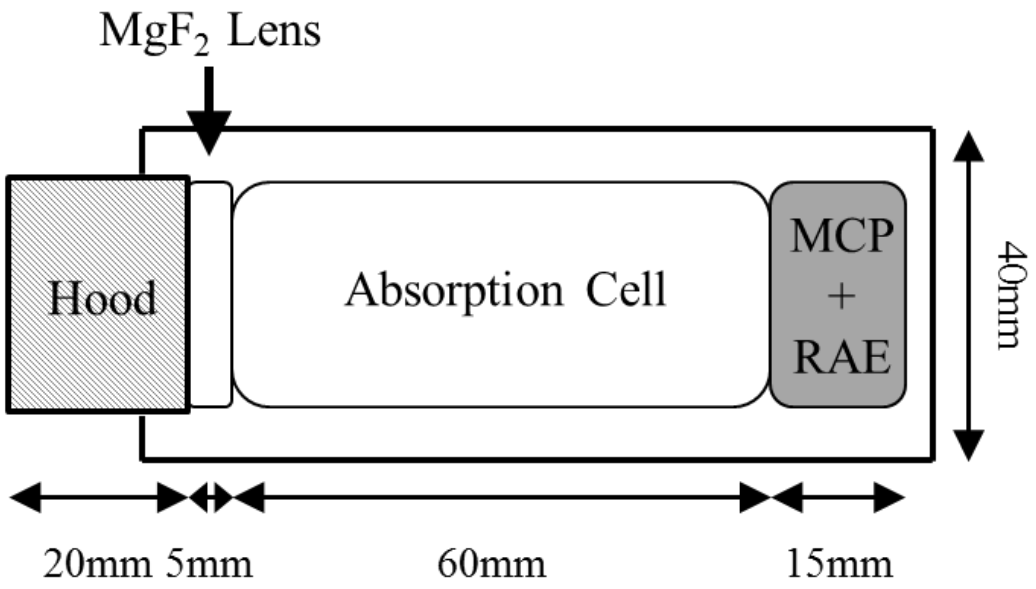

Figure 3.12. Schematic diagram of the new absorption cell imager. The imager consists of an absorption cell, an MgF_2 lens, a detector (MCP + RAE), and a hood. It can be constructed with a weight of < 1 kg and an envelope of < 1 U.

Table 3.3. Specifications of the absorption cell imager

Target Wavelength	121.6 nm (H Lyman-alpha)
Angular Resolution	0.1 deg.
Time Resolution	180 s
Field of View	25.6×25.6°
Data Format	$256 \times 256\,\mathrm{bin}^2$
Mass	< 1 kg
Size	< 1 U
Effective Area of MCP	Φ25 mm
Open Aperture	1.65 cm^2
Cell Diameter	25 mm
Filament Type	Type-C
Gas Pressure in Cell	200 Pa

Table 3.4. Efficiencies of each component

Transmittance of MgF_2 Lens	0.5
Transmittance of MgF_2 Window	0.1
Quantum Efficiency of MCP	0.01

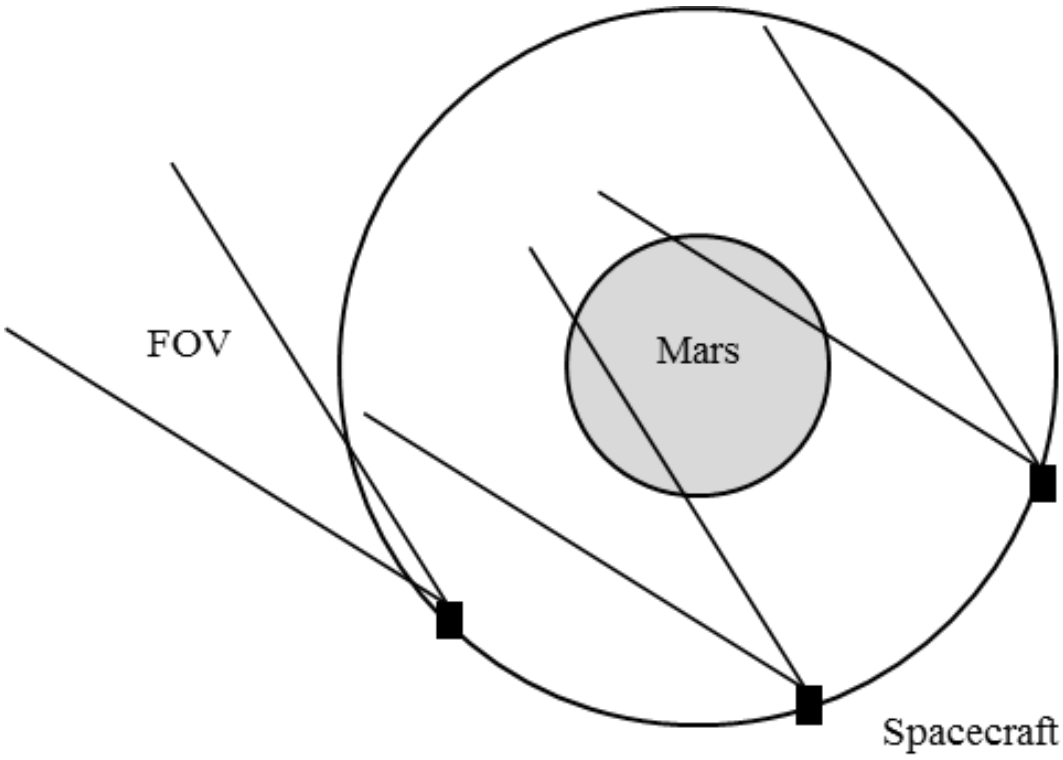

Figure 3.13. Geometry of the Martian corona observation. The imager can perform spatial scanning by orbital motion by fixing one axis of the spacecraft in inertial space to image the Martian limb.

Table 3.5. Observation dataset

Power [W]	Exp. Time [sec]
0	180
1	180
1.5	180
1.6	180
2.1	180

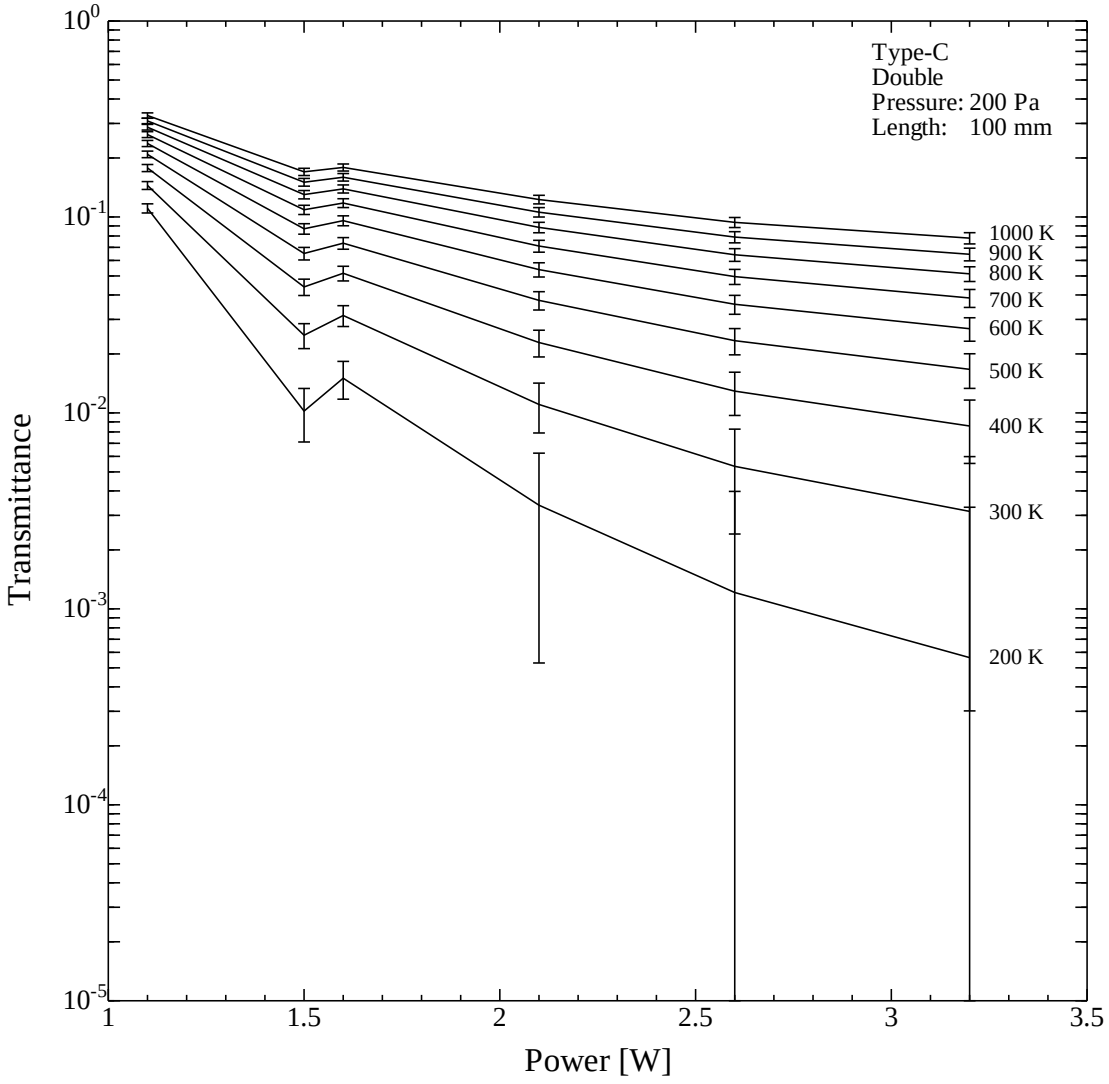

Figure 3.14. Simulation of the temperature measurements of planetary corona's using the new Type-C absorption cell. The cause for the dip at ~1.5 W that appears in all the measurements of Type-C has not been clearly identified. Although these dips are probably artifact, further investigations are necessary.

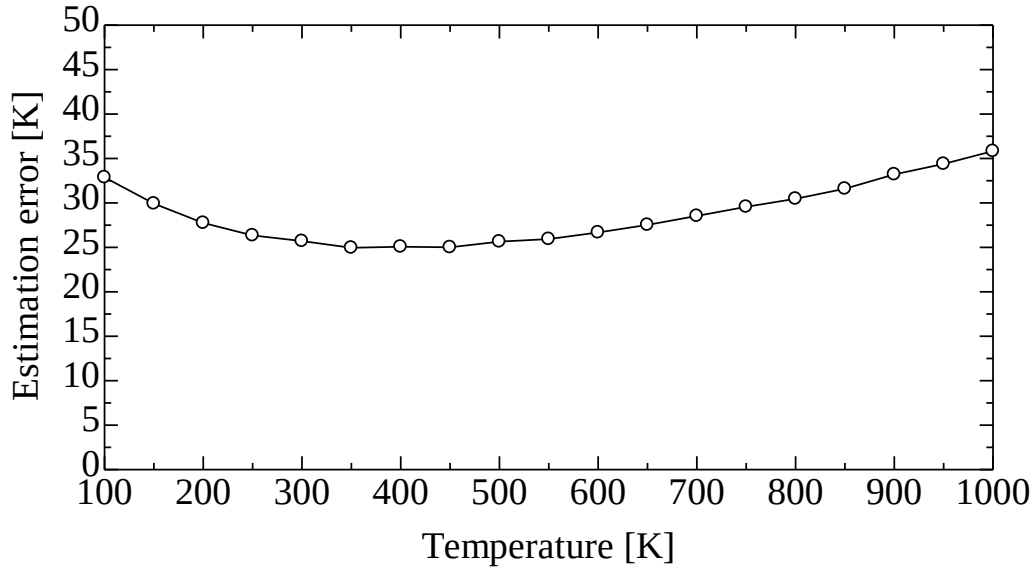

Figure 3.15. Temperature estimate errors of the Martian hydrogen corona. The temperature can be probed with an accuracy of about 30 K.

3.7. Conclusions

I have developed newly designed absorption cells to evaluate the dissociation efficiency of various tungsten filaments. The performance of the cells (optical thicknesses and FWHMs) was evaluated with various precursor H_2 gas pressures, applied filament powers, and optical path lengths using the VUV-FTS installed on the DESIRS beamline at SOLEIL. In Table 3.6, the optimized parameters from the present experiments are shown.

Table 3.6. Optimized parameter values for the new absorption cells

Diameter [μm]	Power [W]	Pressure [Pa]
24.4	1-3	100-300

The present investigation has shown that the improved absorption cells have better performance than the previous cells. I have confirmed that the filaments should be

thin and that the appropriate gas pressure and applied power should be remained in the range of 100-300 Pa and 1-3 W, respectively. Using these parameters, I found that about a 4 times higher optical thickness can be achieved compared to that with the UVS-P. I have also demonstrated that the Doppler temperature of Martian coronas can be determined with an accuracy of about 30 K.

When the filament is turned on, the dissociative adsorption rate of hydrogen molecules and the desorption rate of hydrogen atoms on the filament surface in the cell immediately reaches an equilibrium state. Since the desorption rate is determined by the temperature of the filament surface and the number of adsorption sites, a large surface area and high-power density lead to a higher efficiency of the absorption cell. In consideration of the above, I fabricated shorter and/or thinner filaments than the previous studies and evaluated their performances, but the optimum value has not yet been determined. Further performance evaluations of the thinner and shorter filaments are needed in the near future. In addition to the filament shape, the optical length of the cell can also be reduced in consideration of the results of the present experiments. These results suggest that further miniaturization of the absorption cell can be performed. Through this experiment, I established a procedure for future parameter optimization.

In addition to the performance upgrade (improvement), the new absorption cell can be constructed with a weight of less than 2 kg including the analog electronics and in an outer envelope smaller than 2 U (1 U=$100 \times 100 \times 100$ mm^3). Such a compact design can be integrated in an ultra-small satellite or explorer; therefore, I believe that the absorption cell technique is suitable for future ultra-small space missions. For example, this technique could be used for geocoronal observations by a lunar orbiter or the Japanese Experiment Module (JEM) in the International Space Station. Ultra-small satellite missions equipped with a space telescope and dedicated to the observation of planets (for instance the Martian corona), icy satellites, and comets [*Shinnaka et al.*, 2017] will also benefit from the compactness of the device.

However, additional performance evaluations are still needed. The optimization is now underway for the shape of the tungsten filament and the filament-beam path geometry. An endurance test of the filaments and confirmations of the stability of the

performance should also be conducted. Calibration methods in space are also an issue that should be considered for future missions. The development and evaluation of a deuterium absorption cell are also planned. Indeed, a determination of the D/H ratio isotopic ratio would help for estimating the total amount of water lost since planet birth, combining data from comets, asteroids, and planets [*Hartogh et al.*, 2011; *Alexander et al.*, 2012; *Altwegg et al.*, 2014].

References

Alexander, C. O. D., Bowden, R., Fogel, M. L., Howard, K. T., Herd, C. D. K., and Nittler, L. R. (2012). The provenances of asteroids, and their contributions to the volatile inventories of the terrestrial planets. *Science*, *337*(6095), 721-723.

Altwegg, K., Balsiger, H., Bar-Nun, A., Berthelier, J. J., Bieler, A., Bochsler, P., Briois, C., Calmonte, U., Combi, M., De Keyser, J., Eberhardt, P., Fiethe, B., Fuselier, S., Casc, S., Gombosi, T. I., Hansen, K. C., Hässig, M., Jäckel, A., Kopp, E., Korth, A., LeRoy, L., Mall, U., Marty, B., Mousis, O., Neefs, E., Owen, T., Rème, H., Rubin, M., Sémon, T., Tzou, C.-Y., Waite, H., and Wurz, P. (2014). 67P/Churyumov-Gerasimenko, a Jupiter family comet with a high D/H ratio. *Science*, 1261952.

Babichenko, S. I., Deregusov, E. V., Kurt, V. G., Romanova, N. N., Skliankin, V. A., Smirnov, A. S., Bertaux, J. J., and Blamont, J. (1977). Measurements in interplanetary space and in the Martian upper atmosphere with a hydrogen absorption-cell spectrophotometer for L-alpha radiation on-board Mars 4-7 spaceprobes. *Space Science Instrumentation*, *3*, 271-286.

Bailey, J., and Gruntman, M. (2011). Experimental study of exospheric hydrogen atom distributions by Lyman‐alpha detectors on the TWINS mission. *Journal of Geophysical Research: Space Physics*, *116*(A9).

Bailey, J., and Gruntman, M. (2013). Observations of exosphere variations during geomagnetic storms. *Geophysical Research Letters*, *40*(10), 1907-1911.

Bertaux, J. L. (1978). Interpretation of OGO-5 line shape measurements of Lyman-α emission from terrestrial exospheric hydrogen. *Planetary and Space Science*, *26*(5), 431-447.

Bertaux, J. L., and Blamont, J. E. (1971). Evidence for a source of an extraterrestrial hydrogen Lyman-alpha emission. *Astronomy and Astrophysics*, *11*, 200.

Bertaux, J. L., and Blamont, J. E. (1973). Interpretation of OGO 5 Lyman alpha measurements in the upper geocorona. *Journal of Geophysical Research*, *78*(1), 80-91.

Bertaux, J. L., Blamont, J. E., Tabarie, N., Kurt, W. G., Bourgin, M. C., Smirnov, A. S., and Dementeva, N. N. (1976). Interstellar medium in the vicinity of the sun-A temperature measurement obtained with Mars-7 interplanetary probe. *Astronomy and Astrophysics*, *46*, 19-29.

Bertaux, I. L., Blamont, J., Marcelin, M., Kurt, V. G., Romanova, N. N., and Smirnov, A. S. (1978). Lyman-Alpha observations of Venera-9 and 10 I. The non-thermal hydrogen population in the exosphere of Venus. *Planetary and Space Science*, *26*(9), 817-831.

Bertaux, J. L., Blamont, J. E., Lepine, V. M., Kurt, V. G., Romanova, N. N., and Smirnov, A. S. (1981). Venera 11 and Venera 12 observations of EUV emissions from the upper atmosphere of Venus. *Planetary and Space Science*, *29*(2), 149-166.

Bertaux, J. L., and Lallement, R. (1984). Analysis of interplanetary Lyman-alpha line profile with a hydrogen absorption cell-Theory of the Doppler angular spectral scanning method. *Astronomy and Astrophysics*, *140*, 230-242.

Bertaux, J. L., Lallement, R., Kurt, V. G., and Mironova, E. N. (1985). Characteristics of the local interstellar hydrogen determined from PROGNOZ 5 and 6 interplanetary Lyman-alpha line profile measurements with a hydrogen absorption cell. *Astronomy and Astrophysics*, *150*, 1-20.

Bertaux, J. L., Le Texier, H., Goutail, F., Lallement, R., and Kockarts, G. (1989, December). Lyman alpha observations of geocoronal and interplanetary hydrogen from Spacelab-1-Exospheric temperature and density and hot emission. In *Annales Geophysicae* (Vol. 7, pp. 549-563).

Chaffin, M., Chaufray, J., Stewart, A. I., Schneider, N. M., Montmessin, F., and Bertaux, J. (2013, December). Models and Observations of Time-Varying Hydrogen Escape at Mars. In *AGU Fall Meeting Abstracts*.

Chaufray, J. Y., Bertaux, J. L., Leblanc, F., and Quémerais, E. (2008). Observation of the hydrogen corona with SPICAM on Mars Express. *Icarus*, *195*(2), 598-613.

Clarke, J. T., Bertaux, J. L., Chaufray, J. Y., Gladstone, G. R., Quémerais, E., Wilson, J. K., and Bhattacharyya, D. (2014). A rapid decrease of the hydrogen corona of

Mars. *Geophysical Research Letters*, *41*(22), 8013-8020.

Clarke, J. T., Mayyasi, M., Bhattacharyya, D., Schneider, N. M., Mcclintock, W. E., Deighan, J. I., Stewart, A. I. F., Chaufray, J.-Y., Chaffin, M. S., Jain, S. K., Stiepen, A., Crismani, M., Holsclaw, G. M., Montmessin, F., and Jakosky, B. M. (2017). Variability of D and H in the Martian upper atmosphere observed with the MAVEN IUVS echelle channel. *Journal of Geophysical Research: Space Physics*, *122*(2), 2336-2344.

Esposito, L. W., Barth, C. A., Colwell, J. E., Lawrence, G. M., McClintock, W. E., Stewart, A. I. F., Keller, H. U., Korth, A., Lauche, H., Festou, M. C., Lane, A. L., Hansen, C. J., Maki, J. N., West, R. A., Jahn, H., Reulke, R., Warlich, K., Shemansky, D. E., and Yung, Y. L. (2004). The Cassini ultraviolet imaging spectrograph investigation. *Space science reviews*, *115*(1-4), 299-361.

Feldman, P. D., Steffl, A. J., Parker, J. W., A'Hearn, M. F., Bertaux, J. L., Stern, S. A., Weaver, H. A., Slater, D. C., Versteeg, M., Throop, H. B., Cunningham, N. J., and Feaga, L. M. (2011). Rosetta-Alice observations of exospheric hydrogen and oxygen on Mars. *Icarus*, *214*(2), 394-399.

Funase, R., Inamori, T., Ikari, S., Ozaki, N., and Koizumi, H. (2015). Initial operation results of a 50kg-class deep space exploration micro-spacecraft PROCYON.

Hartogh, P., Lis, D. C., Bockelée-Morvan, D., de Val-Borro, M., Biver, N., Küppers, M., Emprechtinger, M., Bergin, E. A., Crovisier, J., Rengel, M., Moreno, R., Szutowicz, S., and Blake, G. A. (2011). Ocean-like water in the Jupiter-family comet 103P/Hartley 2. *Nature*, *478*(7368), 218.

Heays, A. N., Dickenson, G. D., Salumbides, E. J., De Oliveira, N., Joyeux, D., Nahon, L., Lewis, B. R., and Ubachs, W. (2011). High-resolution Fourier-transform extreme ultraviolet photoabsorption spectroscopy of $^{14}N^{15}N$. *The Journal of chemical physics*, *135*(24), 244301.

Kameda, S., Ikezawa, S., Sato, M., Kuwabara, M., Osada, N., Murakami, G., Yoshioka, K., Yoshikawa, I., Taguchi, M., Funase, R., Sugita, S., Miyoshi, Y., and Fujimoto, M. (2017). Ecliptic North‐South Symmetry of Hydrogen Geocorona. *Geophysical Research Letters*, *44*(23), 11,706-11,712.

Kawahara, T. D., Okano, S., Abe, T., Fukunishi, H., and Ito, K. (1997). Glass-type hydrogen and deuterium absorption cells developed for D/H ratio measurements in the Martian atmosphere. *Applied optics*, *36*(10), 2229-2237.

Kuwabara, M., Yoshioka, K., Murakami, G., Tsuchiya, F., Kimura, T., Yamazaki, A., and Yoshikawa, I. (2017). The geocoronal responses to the geomagnetic disturbances. *Journal of Geophysical Research: Space Physics*, *122*(1), 1269-1276.

Lallement, R., Bertaux, J. L., Kurt, V. G., and Mironova, E. N. (1984). Observed perturbations of the velocity distribution of interstellar hydrogen atoms in the solar system with Prognoz Lyman-alpha measurements. *Astronomy and Astrophysics*, *140*, 243-250.

Lallement, R., Bertaux, J. L., and Dalaudier, F. (1985). Interplanetary Lyman-alpha spectral profiles and intensities for both repulsive and attractive solar force fields Predicted absorption pattern by a hydrogen cell. *Astronomy and Astrophysics*, *150*, 21-32.

Lide, D. R. (1994). CRC Handbook of Chemistry and Physics, 75th ed., pp. 10-296, 12-41, 12-160.

McClintock, W. E., Schneider, N. M., Holsclaw, G. M., Clarke, J. T., Hoskins, A. C., Stewart, I., Montmessin, F., Yelle, R. V., and Deighan, J. (2015). The imaging ultraviolet spectrograph (IUVS) for the MAVEN mission. *Space Science Reviews*, *195*(1-4), 75-124.

McComas, D. J., Allegrini, F., Baldonado, J., Blake, B., Brandt, P. C., Burch, J., Clemmons, J., Crain, W., Delapp, D., DeMajistre, R., Everett, D., Fahe, H., Friesen, L., Funsten, H., and Goldstein, J. (2009). The two wide-angle imaging neutral-atom spectrometers (TWINS) NASA mission-of-opportunity. *Space Science Reviews*, *142*(1-4), 157-231.

Meier, R. R., and Prinz, D. K. (1970). Absorption of the solar Lyman alpha line by geocoronal atomic hydrogen. *Journal of Geophysical Research*, *75*(34), 6969-6979.

Morton, D. C., and Purcell, J. D. (1962). Observations of the extreme ultraviolet

radiation in the night sky using an atomic hydrogen filter. *Planetary and Space Science*, *9*(8), 455-458.

Nahon, L., de Oliveira, N., Garcia, G. A., Gil, J. F., Pilette, B., Marcouillé, O., Lagarde, B., and Polack, F. (2012). DESIRS: a state-of-the-art VUV beamline featuring high resolution and variable polarization for spectroscopy and dichroism at SOLEIL. *Journal of synchrotron radiation*, *19*(4), 508-520.

Nass, H. U., Zoennchen, J. H., Lay, G., and Fahr, H. J. (2006). The TWINS-LAD mission: Observations of terrestrial Lyman-[alpha] fluxes. *Astrophysics and Space Sciences Transactions (ASTRA)*, *2*(1), 27.

Oliveira, N. D., Joyeux, D., Roudjane, M., Gil, J. F., Pilette, B., Archer, L., Ito, K., and Nahon, L. (2016). The high-resolution absorption spectroscopy branch on the VUV beamline DESIRS at SOLEIL. *Journal of synchrotron radiation*, *23*(4), 887-900.

Shinnaka, Y., Fougere, N., Kawakita, H., Kameda, S., Combi, M. R., Ikezawa, S., Seki, A., Kuwabara, M., Sato, M., Taguchi, M., and Yoshikawa, I. (2017). IMAGING OBSERVATIONS OF THE HYDROGEN COMA OF COMET 67P/CHURYUMOV–GERASIMENKO IN 2015 SEPTEMBER BY THE PROCYON/LAICA. *The Astronomical Journal*, *153*(2), 76.

Smith Jr, J. N., and Fite, W. L. (1962). Reflection and Dissociation of H2 on Tungsten. *The Journal of Chemical Physics*, *37*(4), 898-904.

Taguchi, M., Fukunishi, H., Watanabe, S., Okano, S., Takahashi, Y., and Kawahara, T. D. (2000). Ultraviolet imaging spectrometer (UVS) experiment on board the NOZOMI spacecraft: Instrumentation and initial results. *Earth, planets and space*, *52*(1), 49-60.

Yoshikawa, I., Yoshioka, K., Murakami, G., Yamazaki, A., Tsuchiya, F., Kagitani, M., Sakanoi, T., Terada, N., Kimura, T., Kuwabara, M., Fujiwara, K., Hamaguchi, T., and Tadokoro, H. (2014). Extreme ultraviolet radiation measurement for planetary atmospheres/magnetospheres from the Earth-orbiting spacecraft (Extreme Ultraviolet Spectroscope for Exospheric Dynamics: EXCEED). *Space Science Reviews*, *184*(1-4), 237-258.

Yoshioka, K., Murakami, G., Yamazaki, A., Tsuchiya, F., Kagitani, M., Sakanoi, T., Kimura, T., Uemizu, K., Uji, K., and Yoshikawa, I. (2013). The extreme ultraviolet spectroscope for planetary science, EXCEED. *Planetary and Space Science*, *85*, 250-260.

Chapter 4. Concluding Remarks

In this thesis, I have developed the two UV instruments dedicated for ultra-small spacecraft missions. These approaches are expected to lead opportunity of future explorations to increase.

Development of the ultra-small EUV imager (Chapter 2)

The technique of multilayer coating which enhances the reflectivity of a mirror utilizing interference of reflected light has been conventionally used in the planetary science.

To obtain a higher reflectivity at the wavelength of 30.4 nm than the traditional Mo/Si multilayer coating, the Mg/SiC coating has been developed. The Mg/SiC multilayer coated mirror has achieved about twice as high reflectivity as the Mo/Si mirror. Additionally, high stability of the reflectivity of the Mg/SiC multilayer coated mirror has been confirmed through the environment dependency confirmation test. After the estimation of the overall detection efficiency, it has been concluded that PHOENIX can observe the plasmasphere with temporal and spatial resolutions of < 1 hour and 0.15 Re, respectively. These values are sufficient to discuss the behavior of plasma in the plasmasphere. In addition, the improvement in efficiency enabled constructing PHOENIX with size of $66 \times 99 \times 99\, mm^2$, and its size is considerably smaller (< 10%) than KAGUYA/TEX.

Development of the absorption cell (Chapter 3)

To optimize the design of the absorption cell with smaller size and lighter weight for future ultra-small missions, newly improved hydrogen absorption cells have been manufactured and their performances have been evaluated by using the French synchrotron facility, SOLEIL. The optimized parameters are as follows; (1) the filament shape (length and diameter), (2) the applied power to the filament, and (3) the gas pressure enclosed in the glass cell. From the results of experiments, it was revealed that the thin filament, the enclosed gas pressure of 100-300 Pa, and the applied power of 1-3

W are required to obtain high efficiency. The new cells can be applied for planetary corona observations because they are small and light and operated with low power consumption. The new cell can measure the temperature of the Martian upper atmosphere with an accuracy of ~30 K and clarify dependences of hydrogen dissipation on the solar activity and season. Through this experiment, I established the procedure for future parameter optimization of absorption cell technique.

Appendix

A. Calculation of Reflectivity and Transmittance

One of the main factors which decide the reflectivity and transmittance of the materials is the complex refractive index. The ideal reflectivity of materials is computed as follows.

Consider that the light enter the plane surface of the material, whose complex refractive index can be expressed as $N_i = n_i - ik_i$, from a vacuum medium.

Consider that the multilayer coating consists of N layers. The medium between the boundary surfaces k-1 and k is called the k-th layer, the interval is h_k, and the refractive index thereof is n_k. Assuming that the incident angle of the plane wave to the multilayer coating is θ_0 and the incident angle at the boundary surface k of the k-th layer is θ_k, the following equation holds.

$$n_0 \sin\theta_0 = n_1 \sin\theta_1 = \cdots = n_k \sin\theta_k = \cdots = n_N \sin\theta_N \tag{A-1}$$

The tangential component of the electric field at the interface is given by

$$E_k = E_k^{(i)} + E_k^{(r)} \tag{A-2}$$

where $E_k^{(i)}$ and $E_k^{(r)}$ are the tangential component of the incident wave and the reflected wave, respectively. The tangential component of the magnetic field is given by the following equation.

$$H_k = \sqrt{\frac{\varepsilon_0}{\mu_0}} n_k \cos\theta_k (E_k^{(i)} - E_k^{(r)}) \tag{A-3}$$

The phase of the tangential components of the incident wave and the reflected wave changed as below.

$$\delta_k = \frac{2\pi}{\lambda_0} n_k h_k \cos\theta_k \tag{A-4}$$

At a position immediately below the boundary surface k-1, the phase is advanced with respect to the boundary surface k, and the phase of the boundary surface k is delayed. Therefore, the following equation holds.

$$E_k^{'} = E_k^{(i)} \exp(i\delta_k) + E_k^{(r)} \exp(-i\delta_k) \tag{A-5}$$

The same applies to the magnetic field. The tangential components of the electric and magnetic fields are continuous at each interface.

$$E_{k-1} = E_k^{'} = E_k^{(i)} \exp(i\delta_k) + E_k^{(r)} \exp(-i\delta_k) \tag{A-6}$$

$$H_{k-1} = H_k^{'} = \sqrt{\frac{\varepsilon_0}{\mu_0}} n_k \cos\theta_k \left[E_k^{(i)} \exp(i\delta_k) - E_k^{(r)} \exp(-i\delta_k)\right] \tag{A-7}$$

Following the above equations, the electric field and the magnetic field are described below

$$E_{k-1} = E_K \cos\delta_k + iH_k \frac{\sin\delta_k}{\sqrt{\varepsilon_0/\mu_0}\eta_k} \tag{A-8}$$

$$H_{k-1} = iE_k \sin\delta_k \sqrt{\frac{\varepsilon_0}{\mu_0}} \eta_k + H_k \cos\delta_k \tag{A-9}$$

$$\eta_k = n_k \cos\theta_k \tag{A-10}$$

where η_k is called as an effective refractive index in the case of s-polarized lights. The optical admittance Y_k is represented below.

$$Y_k = \sqrt{\frac{\varepsilon_0}{\mu_0}}\eta_k \tag{A-11}$$

The equation of the electric and the magnetic fields can be expressed as follows using the characteristic matrix M_k.

$$\begin{pmatrix} E_{k-1} \\ H_{k-1} \end{pmatrix} = M_k \begin{pmatrix} E_k \\ H_k \end{pmatrix} \tag{A-12}$$

$$[M_k] = \begin{pmatrix} \cos\delta_k & \dfrac{i\sin\delta_k}{Y_k} \\ iY_k \sin\delta_k & \cos\delta_k \end{pmatrix} \tag{A-13}$$

The same analysis can be performed for p-polarized lights and the effective refractive index is expressed by the following equation.

$$\eta_k = \frac{n_k}{\cos\theta_k} \tag{A-14}$$

Generally, in the multilayer coating composed of the N layer, the following formula is given.

$$\begin{pmatrix} E_0 \\ H_0 \end{pmatrix} = [M_1][M_2]\cdots[M_N] \begin{pmatrix} E_N \\ H_N \end{pmatrix} \tag{A-15}$$

The reflectivity and the transmittance can be calculated using the characteristic matrix as follows.

$$R = |r|^2 = \left|\frac{E^{(r)}}{E_0^{(i)}}\right|^2 = \left|\frac{Y_0(m_{11} + Y_{N+1}m_{12}) - (m_{21} + Y_{N+1}m_{22})}{Y_0(m_{11} + Y_{N+1}m_{12}) + (m_{21} + Y_{N+1}m_{22})}\right|^2 \tag{A-16}$$

$$T = \frac{n_{N+1}\cos\theta_{N+1}}{n_0\cos\theta_0}|t|^2 = \frac{Y_{N+1}}{Y_0}\left|\frac{E_{N+1}^{(i)}}{E_0^{(i)}}\right|^2 = \frac{Y_{N+1}}{Y_0}\left|\frac{2Y_0}{Y_0\left(m_{11}+Y_{N+1}m_{12}\right)+\left(m_{21}+Y_{N+1}m_{22}\right)}\right|^2 \quad \text{(A-17)}$$

$$[M_k] = \begin{pmatrix} m_{11} & m_{12} \\ m_{21} & m_{22} \end{pmatrix} \quad \text{(A-18)}$$